IMPERIAL COLLEGE LONDON

UNIVERSITY OF LONDON

A COMPARISON OF THE VIBRO-MODULATION AND THERMOSONIC NDT TECHNIQUES

by

Marco Morbidini

A Thesis submitted to the University of London for the degree of

Doctor of Philosophy

Supervised by Prof. Peter Cawley

Nondestructive Testing Laboratory

Department of Mechanical Engineering

Imperial College London

London SW7 2AZ

April 2007

Abstract

Thermosonics and vibro-acoustic modulation (VAM) are two recent nondestructive testing (NDT) techniques which show potential to improve the detection of interface-type defects (fatigue cracks in metals and delaminations in composites) compared to traditional NDT methods. These two novel "active" techniques have in common the excitation of structural vibrations of the test-sample to generate significant displacement of the defect interfaces. In thermosonics this is achieved by high power ultrasound applied to the specimens by high power sonotrodes (20 or 40 kHz). In VAM the defect is vibrated by the excitation (by impact or by an electro-magnetic shaker) of the lowest frequency modes of the structure. The diagnosis of damage is done by using different "pick-up" methods. Thermosonics exploits the local generation of heat, due to friction and/or stress concentration, which can be imaged by modern infrared (IR) thermal imaging cameras. VAM uses the modulation of an additional interrogating ultrasonic field, which is the result of a nonlinearity introduced by the defect in the previously linear and undamaged structure.

In this Thesis, an extensive experimental study of both NDT techniques is presented. The general aim of the study has been to assess and then compare the sensitivity of both methods as a function of defect size as well as their rapidity and reliability of application. Laboratory specimens with fatigue cracks of variable size were prepared and quantitative measurements were taken using both methods. VAM tests were carried out at different amplitudes of the low frequency modulating wave and for a wide range of ultrasonic frequencies (70 - 230 kHz) to find those at which the sensitivity to damage was maximum. A damage index is proposed to evaluate the crack severity. Thermosonic experiments were carried out varying the amplitude of

the input ultrasound to study the correlation between vibration level and temperature rise. This was achieved through the characterization of the extra damping introduced in the specimens by the crack. Based on this information, an algorithm is proposed for the prediction of the thermosonic signal from vibration records.

The results of the experiments show that VAM has a relatively limited sensitivity to small cracks, because it is affected by coherent noise generated at the supports of the specimen. On the other hand, thermosonics can potentially detect smaller cracks if a sufficient vibration amplitude is excited in the specimens. Hence, the reliability in detecting small cracks using thermosonics was studied further and led to the definition of practical calibration and testing procedures that allow us to detect reliably any cracks.

Acknowledgements

I would like to express my gratitude to my supervisor Prof. Peter Cawley for his invaluable guidance during this work. I would also like to thank all the colleagues of the NDT Laboratory. They have provided sound technical support, inspirational discussions and great encouragement throughout the project.

In particular, I want to acknowledge the co-operation with Dr. Philippe Duffour and Dr. Tim Barden during respectively the first (vibro-acoustic modulation) and second (thermosonics) stage of this project. Much of our work has been the result of our synergies.

A significant part of the work was carried out in the departmental Materials Testing Laboratory, where I received the competent and enthusiastic help of Mr. Hugh McGillivray and Mr. Amit Choda.

Furthermore, I have to acknowledge the Engineering and Physical Sciences Research Council (EPSRC), which has primarily funded this work, and the sponsorship of the following industrial partners: AIRBUS, Rolls-Royce, BNFL and dstl.

Last (but not less important), I would like to heartily thank all those people who have sincerely cared for me during these years, namely my father Alessandro, my mother Gioiella and my love Tiziana. I met Tizi immediately after I started my PhD and our relationship has grown in parallel with this work.

Primavera Baciata dal Sole
col Profumo di Rose e di Viole

Viva Sant' Ubaldo e Viva Sant' Antonio!

List of Symbols

a	crack length during fatiguing
$_a$	subscript, average value
$_{avg}$	subscript, average value
A	amplitude of vibration
A_{cs}	area of cross section
b	negative fatigue strength exponent
B_0	dc value of the modulating wave
B_1	peak value of the ac part of the modulating wave
$c_0, c_1, etc.$	Fourier coefficients
C_N	strain energy per unit strain squared of mode N
C'	fatigue strength coefficient
C''	fatigue propagation coefficient
Cal	experimental calibration factor
d	depth
$\mathbf{E}$	complex modulus of elasticity
$_{exp}$	subscript, means experimental
f	frequency
$_{fe}$	subscript, refers to finite element
F	amplitude of fundamental frequency
h	height
$H_o(f)$	frequency transfer function for open crack
$H_c(f)$	frequency transfer function for closed crack
i	(also subscript) running number of vibration cycles or $\sqrt{-1}$
k	time constant of exponential decay used in the heating index
K	stress intensity factor

continue on next page

continue from previous page

K_c	fracture toughness
ΔK	cyclic stress intensity factor
$_I$	subscript, refers to mode 1 of fracture mechanics
I	second moment of area
$Im()$	imaginary part of quantity
L_s	length of specimen
L_f	distance of supports during fatiguing (flexural length)
m	fatigue propagation exponent
$_{max}$	subscript, refers to maximum value
M	bending moment
^{n}	superscript, denotes the n-th mode
$_n$	subscript, denotes the n-th segment
N	total number of cycles in fatiguing
$_N$	subscript, denotes the N-th mode
P_c	static compressive load
P	power dissipated at the crack
Q	damping Q-factor
R	sidebands-to-carrier amplitude ratio
$\overline{R}$	average ratio
$Re()$	real part of quantity
S_c	target crack size to be detected
S_{-1}	amplitude of the first left sideband
S_{+1}	amplitude of the first right sideband
sd	standard deviation
ΔS	variation of a fatigue parameter (stress or strain)
$_{thr}$	subscript, denotes a threshold value
t	time
T	time period or temperature

continue on next page

continue from previous page

ΔT	temperature variation
u	mode shape
V	total strain energy
ΔV	energy dissipated
w	width
W	frequency weight
y	distance from neutral axis
$y_N(x)$	mono-dimensional mode shape of mode N along x
Y	fatigue shape factor

Greek Letters:

α	phase delay
δ	logarithmic decrement of vibration
η	vibration loss factor
$\eta_{uncracked}$	vibration loss factor of an uncracked specimen
$\eta_{crack,3}$	vibration loss factor of a cracked specimen in the 3rd flexural mode
ϵ	strain
κ	thermal diffusivity
$\mu\epsilon$	micro-strain, i.e. $\times 10^{-6}$ the given value
ω	angular frequency
Ψ	specific damping coefficient
σ	stress
$\Delta\sigma$	cyclic variation of stress
τ	time

Contents

List of Tables

List of Figures

Chapter 1

Introduction

1.1 Motivation

The aerospace and nuclear power industries are demanding quicker, more reliable and more sensitive nondestructive testing (NDT) inspection methods for the detection of small fatigue cracks and impact damage in structures. In the maintenance sector, such requirements arise mainly from the need of reducing the maintenance costs, increasing the efficiency of inspection and reducing the dependence on human judgement (for example dye penetrant testing requires well trained operators). In the production sector, the demand of new and better tools for quality control is also increasing.

Established NDT techniques are not completely satisfactory for the detection of fatigue cracks in metals and delaminations in composites. Conventional ultrasonic techniques are widely used in industry and are generally based on the assumption of the linear interaction of an acoustic wave with the defect. In principle, a wave that impacts a defect can undergo reflection or diffraction and the reflected or diffracted wave can be analyzed to obtain information on the presence and size of the defect [1]. However, major problems arise with this approach when there is a lack of a-priori knowledge of the features of the defect that is to be detected. The diagnosis of the presence of a crack by linear ultrasound is usually the result of the

interpretation of an ultrasonic measurement. This interpretation may be difficult or impossible if in the measured data the defect signature is masked by other information contained in the signal, such as reflections from boundaries, diffraction from edges, dispersion phenomena, excitation of multiple modes etc. [1]. Furthermore, the success of conventional ultrasonic techniques for detecting small fatigue cracks may be compromised by ultrasonic grain noise and by the degree of closure of the cracks. Thermal NDT techniques are also currently used in industry as a means of detecting cracks and delaminations [2]. The principle behind such techniques is that the defect acts as a thermal barrier to the heating front stimulated by a high power optical flash. The resulting discontinuity in the thermal field on the specimen surface can be measured by an infrared (IR) camera [3]. However, major problems arise when the defect is too deep to be reached by a significant amount of heat or when the defect interfaces are in contact hence allowing heat transmission [4].

Vibro-acoustic modulation and thermosonics both have the potential of solving these difficulties and therefore the potential of becoming routine NDT fast-screening inspection methods.

1.1.1 Vibro-acoustic modulation

Vibro-acoustic modulation (or vibro-modulation as appears in the title of this Thesis) was first introduced as a NDT method in the early 1990s. It was born from the observation of the amplitude modulation of an ultrasonic vibration field by means of a second low frequency vibration, typically in the sonic range, imposed on a structure containing fatigue defects at a microscopic level [5]. This amplitude modulation also occurs in structures with interface-type defects, such as cracks and delaminations. The principle of this method is represented in Figure 1.1. Vibro-acoustic modulation (VAM) is based on the interaction/mixing of two vibrations that are present simultaneously in a defective structure. Throughout this work it will be assumed that a linear system can be defined as one which responds in accordance to the principle of superposition. When two vibrations at two distinct frequencies are excited in a *linear* system, the resulting interaction is simply given by the sum of

the two separate components. In the frequency domain this would result in the presence of distinct spectral lines at those two distinct frequencies. A plain structure, without any defect, will be considered linear since it is able to transmit separately the two frequency components. A mechanical structure can become nonlinear in the presence of a crack if, for example, the crack opens and closes (*"breathes"*) during the low frequency vibration cycle. When the crack is open or closed the structure will exhibit slightly different frequency response functions (FRF) and this will result in ultrasound amplitude modulation at the frequency of the low frequency vibration. In the frequency domain, the modulation due to the mixing of the two excited frequencies is characterized by the appearance of sidebands to the main ultrasonic probing frequency; this effect will be referred to as *nonlinear* throughout this work. It will be noted that this division between linear and nonlinear systems is based on the assumption that the presence of a crack in a structure must correspond to the introduction of some sort of nonlinearities and, therefore, is rather simplistic. However this simple classification is good enough for the practical purposes of this study which were highlighted in the former subsection.

1.1.2 Thermosonics

Thermosonics is a hybrid thermal-acoustic technique that exploits local heating at the crack/delamination. The heat is generated through the dissipation of mechanical energy at the defect interfaces. The mechanical oscillatory energy is input to the structure by means of a fixed-frequency acoustic resonator typically in the range from 20 to 40 kHz. A schematic representation of the method is given in Figure 1.2. The mechanical energy can be dissipated locally either by clapping or rubbing of the interfaces (heating over the crack area) or by material damping which is especially significant in the zones of stress concentration (for example at the crack tip). The presence of a defect results in a temperature increase on the specimen surface. A temperature measurement is therefore needed in order to inspect the structure. This is performed with a high sensitivity IR imaging camera, which makes thermosonics a "full field" inspection technique. The commercial availability

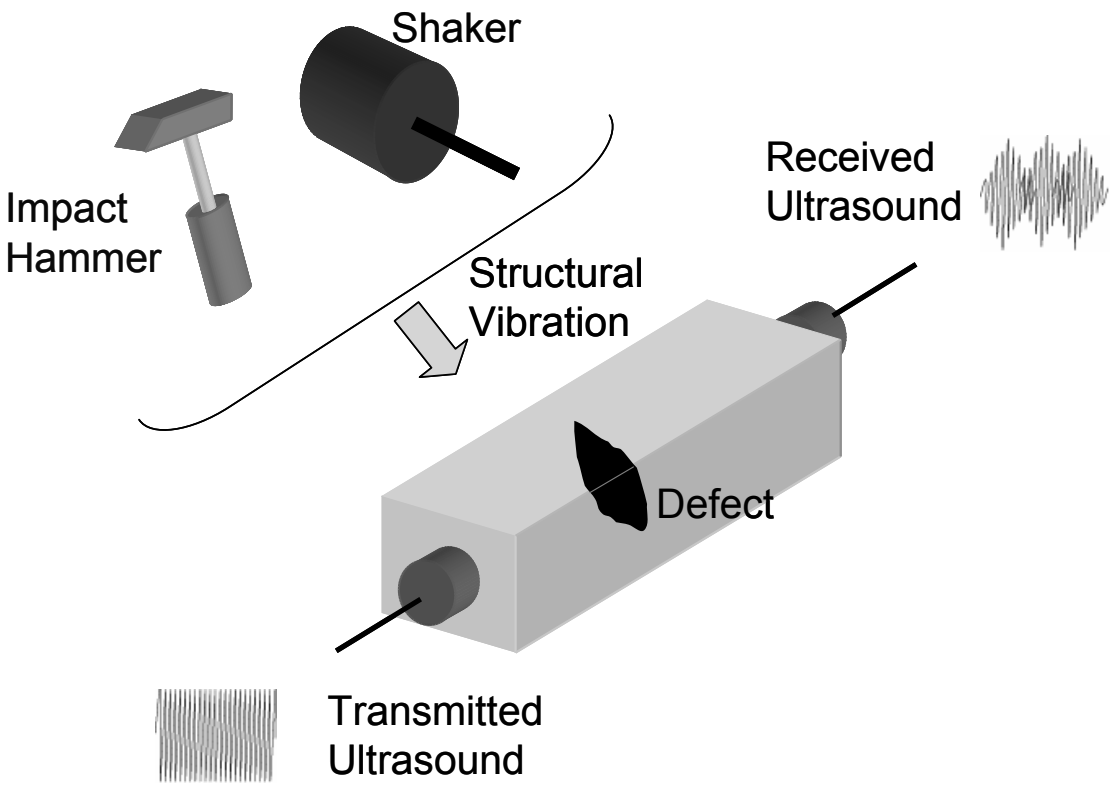

Figure 1.1: *Schematic representation of the VAM method of NDT*

of sensitive cameras has been a key point in the worldwide interest that thermosonics has attracted since Prof. Thomas at Wayne State University, Detroit, USA, [6] introduced this technique in 1999. The idea of the exploitation of the heat produced at the crack when it is subjected to vibrations was already known. In the early eighties Mignogna at al. [7] carried out an extensive study on vibrothermography, a technique that is directly related to thermosonics, but could not be exploited at the time for practical NDT, due to low sensitivity of the IR imaging apparatus then available. Thermosonics differs from vibrothermography because it uses a very short pulse of ultrasound, typically fractions of a second long, whilst vibrothermography uses continuous sonic excitation at a frequency of 20 kHz or less.

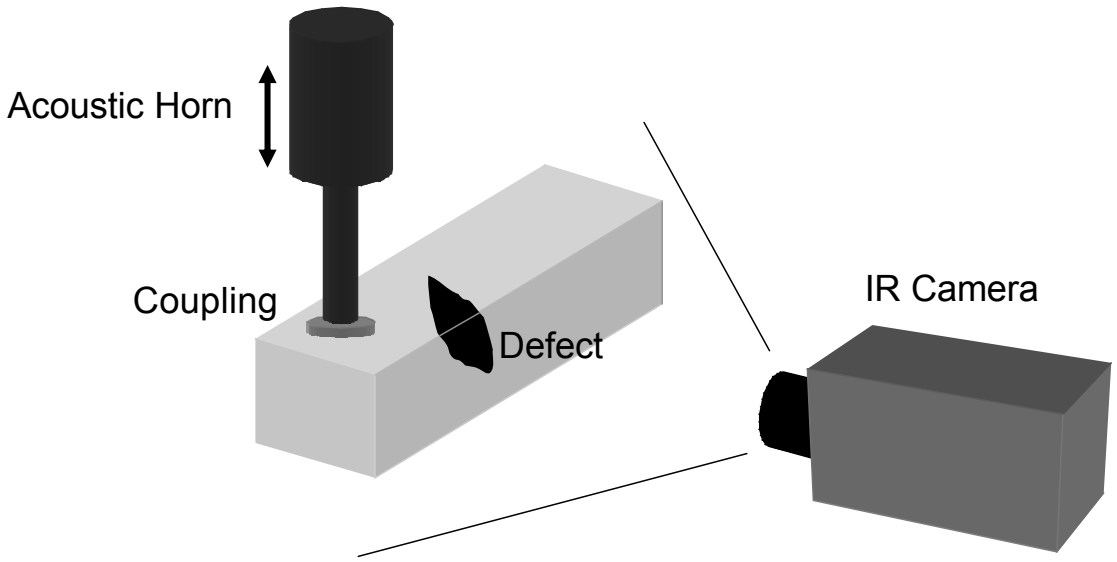

Figure 1.2: *Schematic representing the thermosonic method of NDT*

1.2 Project background

The thermosonics project was structured as a cooperation between the NDT groups at Imperial College London and at the University of Bath. This was done in consideration of the intrinsic interdisciplinary nature of the method which uses vibrational excitation and thermal monitoring [8]. The main responsibility of Imperial College has been to study the characteristics of the vibration field excited in thermosonics, and in particular the evaluation of the interaction of such vibrations with defects. The ideal outcome of this work was the capability of predicting the amount of heat dissipated by a defect during vibration. An additional task assigned to the Imperial College side was that of investigating the potential generation of multiple and sub-multiple harmonic nonlinearities in the samples with defects, when these were vibrated using the same exciter as in thermosonics. This additional part of the work was thought of as an immediate by-product of the thermosonic tests. The NDT research group in Bath has been responsible for the modelling of the defects as heat sources and for the analysis of the thermal fields generated by ultrasonic stimulation.

Early tests demonstrated the impossibility of detecting small cracks by the har-

monics method using the same acoustic horn necessary to vibrate the test-piece in thermosonics. This was principally due to the concurrent generation of large super/sub harmonic nonlinearities (hence the same as those expected to be generated by the cracks) at the contact between the exciter and the test structure, which meant that the presence of a crack could never be tested reliably. However, further tests at Imperial College showed that VAM (which can also be considered a nonlinear method of NDT) had the potential of detecting the fatigue cracks that the harmonics method was failing to detect. Thus, the study of VAM was pursued further and the harmonics method was abandoned.

In this Thesis, only the work carried out under the direct responsibility of the author is described and discussed in detail. This includes:

- the preparation of cracked samples;
- the characterization of cracks;
- the experimental part of the VAM investigation;
- the thermosonic experiments in metals with focus on the vibration analysis;
- the development of a methodology for the prediction of the thermosonic signal from vibration records in cracked metallic samples;
- the formulation of procedures to obtain reliable detection of small cracks in metals.

Dr. Philippe Duffour (also based at Imperial College) worked in the project from October 2003 to December 2004. Dr. Duffour's main area of work was the development of models of modulation mechanisms in VAM, and he also conducted a comparative study of VAM and damping measurement as NDT techniques. He contributed with some ideas to the early stages of the development of a prediction methodology for the thermosonic signal.

Dr. Tim Barden worked in the project at the University of Bath from September 2003 to September 2005. The thermosonic experiments carried out in these two

years were organized in Bath, because of the availability of an IR camera on the site. Later, the IR camera was brought to Imperial College to allow the completion of the work. The tests at Bath were conducted jointly by Dr. Barden and the author of this Thesis. Dr. Barden's main responsibilities during his period at Bath were the development of the thermal models needed in the thermosonic predictions and the application of thermosonics to the detection of impact damage in composites.

The work of Dr. Duffour and Dr. Barden is acknowledged throughout this Thesis, and reports of their findings are included where it is believed they contribute to clarity and completeness of the core topics of this Thesis which have been listed above.

1.3 Thesis overview

VAM and thermosonics are NDT techniques that have recently attracted increasing interest in the NDT community because of their potential to achieve fast detection of *"breathing"* defects in complex structures. In a few cases, both methods are already in use in industrial environments and have replaced conventional inspection procedures [9, 10]. However, more research work is needed before their physics is fully understood and therefore their potential can be fully assessed. This work aims to be a step forward in this direction.

In this Thesis, both methods have been applied to simple specimens with cracks of well known characteristics. Thus, the capability of preparing sets of laboratory specimens with controlled cracks of varying depth has been of primary importance. Chapter 2 gives an account of this initial phase of the project, together with the attempts that have been tried throughout the work to describe in as much detail as possible the morphology of these cracks.

At microscopic level, the morphology of crack-like defects is complex. An accurate study of the dynamics of the interaction of the defect interfaces when the specimen is subjected to complex vibrations would be extremely difficult. The measurement

of the extra-damping introduced in each specimen by the presence of a crack has been a valuable global method of describing the effects of the presence of a crack in a vibrating system. Damping measurements constitute an NDT method on their own, and have therefore been compared to VAM and thermosonics. Furthermore, since the vibration damping quantifies the dissipation of mechanical energy in a vibrating system, it has been used for the prediction of the thermosonic signal. The damping measurements on all the available cracked specimens are described in Chapter 3.

Chapter 4 contains a literature review and the experimental work in the area of VAM. The experiments are carried out using two different implementations of the method. One uses an electromagnetic shaker to excite the low frequency modes, the other uses an impact hammer. The cracks can be detected reliably only after the excitation system and the supports have been optimized. Once the optimized testing rig has been achieved, a systematic study of the method is performed, with the aim of understanding the effects of varying the ultrasonic frequency as well as the amplitude of the low frequency vibration. The following assessment of the general sensitivity of the method leads to the derivation of a damage index. The experimental results are then compared to the analytical and numerical results obtained by Dr. Duffour to validate the proposed vibro-modulation models. The Chapter is concluded by feasibility studies of inspection on real industrial components.

Chapter 5 initially presents a literature review on thermosonics. This will justify the choice of the pulsed version of the method and will highlight the benefits of the proposed approach for the prediction of the temperature rise. The idea is to use damping data measured independently to obtain the temperature rise generated by a certain vibration amplitude. The prediction algorithm arises from considerations on the outcome of the previous damping measurements. The prediction routine is then applied to measurements on a set of steel cracked beams. The validation of the prediction methodology is discussed in detail before the sensitivity of the method to crack size is analyzed.

Chapter 6 addresses the problem of the reliable detection of cracks in metals using thermosonics. The vibration threshold needed to reveal small cracks of known size

is discussed. A detectability criterion which defines the minimum vibrational strain required to detect cracks of given size, using an IR camera of known sensitivity, is enunciated. This criterion is of crucial importance for the future development of practical inspection systems and procedures.

The Thesis concludes with Chapter 7 which includes a summary of the work undertaken, a summary of the relevant scientific findings, a comparison of the VAM and thermosonic methods of NDT and an overview of the areas that would benefit from further work in the author's view.

Chapter 2

Production of cracked specimens

Sets of cracked specimens to be used for VAM and thermosonics research were produced in the the departmental materials testing facilities at Imperial College in order to monitor as closely as possible the fatiguing conditions and consequently the shape, size and morphology of the cracks obtained. It was presumed that these characteristics of the cracks would affect the VAM and thermosonics results. Hence, the strategy of own production was preferred to sourcing from external manufacturers.

An ideal set of laboratory specimens for research on VAM and thermosonics would have the following characteristics:

- specimens of simple geometric shape, easy to handle and to machine;
- one crack in each specimen with controlled location and shape;
- several cracked specimens with cracks of different shape and size.

The following sections describe in detail the procedures followed to obtain cracks of variable size and shape in steel and perspex (trade name for poly-methyl methacrylate) beams. The characteristics of these cracks were then measured using different methods in order to describe their morphology as accurately as possible. The dimensions of the specimens and the results of the measurements taken to study the morphology of the cracks are listed in the summary section (2.4) at the end of this

Chapter. Complete control over the crack characteristics was not achieved at the moment of their production. However, it was possible to produce cracks of different size.

2.1 Production of cracks in steel beams

Fatigue is the nucleation and growth of cracks under cyclic stress. Fatigue is eventually characterized by the appearance (at macroscopic level) of a crack at a free surface of the component, and is most common in metals. The process is initiated by the presence of imperfections at molecular level, due to missing atoms at some locations in the metallic crystalline lattice. These imperfections are known to move and accumulate at the border of the grains, under the effect of cyclic load; hence the formation of nuclei and "slip" zones at the grain boundaries. Above a certain load called *"Fatigue Limit"* the nuclei can break through the grain and form cracks at microscopic level, which can then propagate. If the *"Fatigue Limit"* is never reached the structure is said to have *"Infinite Life"* which is generally characterized by load cycles exceeding $10^6 - 10^7$ without the formation of a fatigue crack [11]. Fatigue can occur in different materials such as ceramics, polymers or composites, but other mechanisms are involved [12].

The *"Fatigue Life"* of a structure subject to fatigue is the number of cycles before the final failure. Systematic studies to understand fatigue phenomena are relatively recent (from the 60s onwards), and all the models derived to predict the *"Fatigue Life"* are mainly based on the fitting of experimental data [11].

When the occurrence of a crack has to be predicted, it is common to refer to a family of curves called *"S-N"* curves, where S is a load parameter (could either be stress or plastic strain depending on whether the fatigue is stress or plastic-strain driven, these are also respectively referred to as high-cycle fatigue and low-cycle fatigue) and N is the number of cycles at which the failure occurs. The general form of the

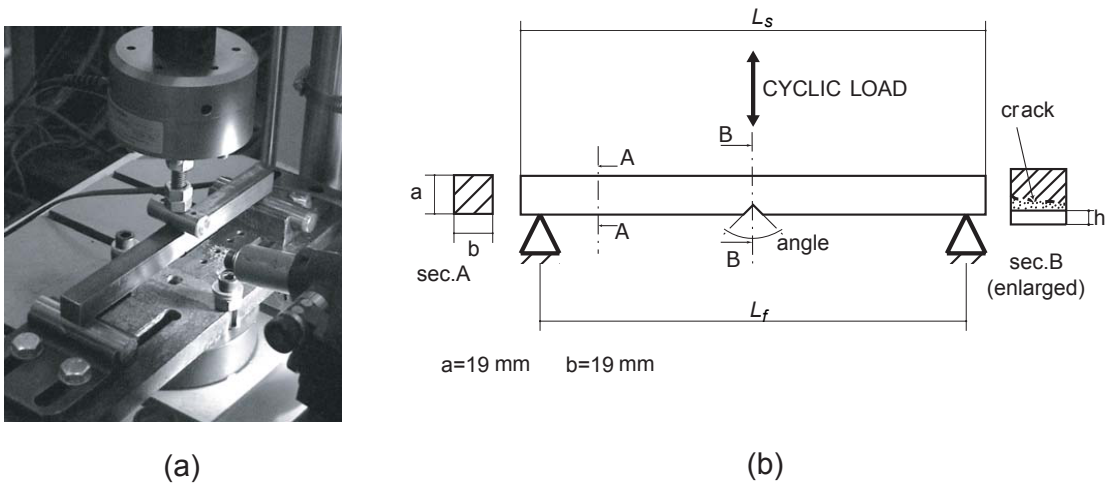

Figure 2.1: *(a) Three-point bending rig for the production of cracks in steel beams by fatigue and, (b), schematic representation of it.*

relation between S and N is:

$$\frac{\Delta S}{2} = C' (2N)^b \tag{2.1}$$

where ΔS is the peak-to-peak amplitude of the loading cycle, C' is the fatigue strength coefficient and b is the negative fatigue strength exponent. These two parameters vary due to the sensitivity of the *"S-N"* curves to surface finish, coatings, notches, residual stresses and changes of mean load. In particular, notches have the effect of a local amplification of the stress and strain and act as stress and strain concentrators, and therefore are often used as a source for crack formation [13].

When the growth rate of an existing crack has to be studied, it is usual to refer to models like the Paris regime. In the Paris regime it is assumed that the crack growth rate da/dN is governed by the cyclic stress intensity factor ΔK:

$$\frac{da}{dN} = C'' \Delta K^m \tag{2.2}$$

where a is the crack length, C'' is the fatigue propagation coefficient and m is the fatigue propagation exponent. ΔK is a function of the variable stress $\Delta\sigma$, the crack length a and of the geometry of the component. The variable loading $\Delta\sigma_{thr}$ under which the fracture does not propagate corresponds by means of equation 2.2 to a

threshold variation of the intensity factor ΔK_{thr} needed to start the propagation [12]. These notions are of use if the propagation of existing cracks is needed.

Figure 2.1 shows the setup used for cracking sets of mild steel beams. The specification of the metal used is, according to the British Standard BS970 and the European Standard EN3B, "bright mild steel for machined parts or shafting" (C 0.20%, Mn 0.50%, Ph 0.05% max., S 0.05% max., Si 0.23%). The beams (square 3/4 inch nominal cross section) were initially V-notched, with notches of variable angles and depths h (see section 2.4), and then loaded on a three-point bending rig using an INSTRON 8872 material testing machine rated at 25 kN nominal load capacity. The distance L_f [see Figure 2.1 (b)] is the effective flexure length during fatiguing. Notches of different geometry were used in order to establish if it was possible to facilitate the generation of straight, through width cracks. This was highly desirable because it would have allowed the sizing of the cracks simply from the measurement of their depth at the edges. However, perfectly straight cracks were not usually achieved using the rig of Figure 2.1. The fatiguing of the specimens was either stopped upon the observation of the formation of a crack at one edge of the notch, or continued at a slightly higher load to grow the cracks further into the material. The monitoring of the specimens to see if the crack was present was done through a microscope. The shape of the cracks and their actual size could only be revealed later after breaking the specimens at the end of the VAM and the thermosonic tests. This will be described in section 2.3.2. In section 2.4, Tables 2.1, 2.2 and 2.3 list the characteristics of the steel specimens and of the cracks produced in them.

2.2 Production of cracks in perspex beams

The procedure followed to produce cracks in perspex beams is different from the one for metals. Static loading was used instead of cyclic loading, and the beams were not only pre-notched but also pre-cracked. The notch was cut in perspex using a hacksaw. The hacksaw was supported on vertical height-adjustable guides

allowing a straight cut. The resulting notch was rectangular, as shown in Figure 2.2, with a groove of width $w \cong 1$ mm. A razor blade was used to pre-crack the perspex specimens. The blade was supported in a block of aluminium and the whole apparatus was cooled in a fridge at a temperature of 4 - 5 $°C$. The notched beam was, at the same time, heated up in boiling water at a temperature of about 100 $°C$. When the cool blade contacted the hot base of the groove, local cooling took place on the specimen, causing the formation of a relatively brittle zone at the base of the notch. Perspex is a thermoset, and therefore its elastic properties are hugely affected by the temperature. Above 90 $°C$ and for high levels of stress the plastic characteristic is dominant whereas at temperatures close to 0 $°C$ the elastic-brittle characteristic is dominant. This facilitates the pre-cracking. The aluminium holder was immediately hit by a hammer, and the result was the production of a straight pre-crack, along the whole width of the specimen as sketched by the shadowed area in Figure 2.2 sec.B. Once a pre-crack was created, it could be propagated to the desired length. For a given pre-crack length a and shape factor Y, the stress intensity factor K can be calculated. In the case of a static load, we will consider a single value K rather than a cyclic range ΔK. If the crack loading is in a normal opening mode (mode I of fracture mechanics) for the equivalent bi-dimensional system sketched in Figure 2.2 the stress intensity factor in mode I, K_I, is given by:

$$K_I = Y\sigma\sqrt{a}; \tag{2.3}$$

where σ is the stress resulting from three-point bending on an uncracked cross section. The condition for propagating the pre-crack is given by:

$$K_I = K_c; \tag{2.4}$$

where K_c is the fracture toughness. The role of the fracture toughness in fracture mechanics is equivalent to that of material strength in yielding. K_c is a property of the material, whilst K_I depends on the loading and on the geometry of the specimen and the fracture [12].

The propagation of the pre-crack was obtained through the application of a controlled displacement at mid-span, as in Figure 2.2. The displacement was increased

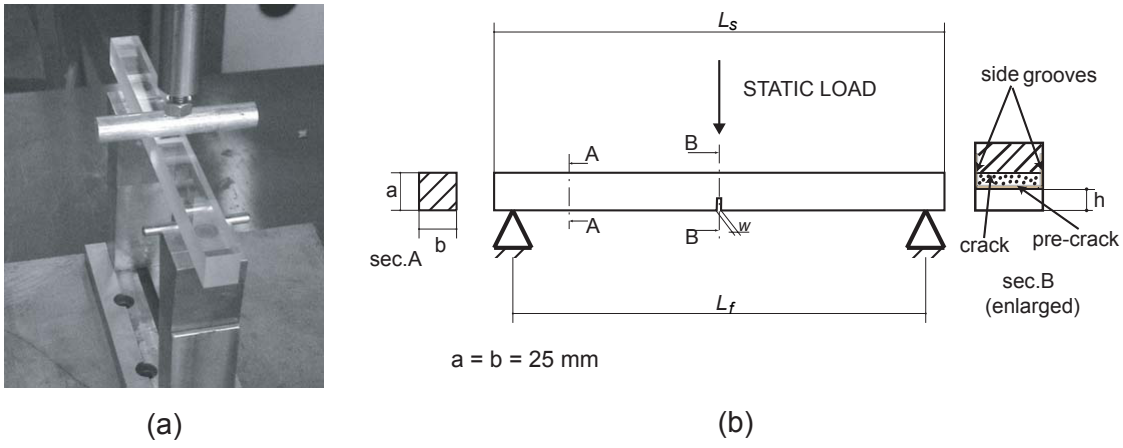

Figure 2.2: *(a) Three-point bending rig for the production of cracks in perspex beams by static loading and, (b), schematic representation of it.*

at an extremely low rate, according to the resolution allowed by the material testing machine. This machine was again the INSTRON 8872, previously used for the fatiguing of metal beams, with a displacement resolution of 0.01 mm. The load was correspondingly slowly increased until the condition expressed in equation 2.4 was satisfied. At this point the fracture propagated. The propagation of the fracture was within the plane of the pre-crack, and it was very likely to remain straight. This was helped by the presence of two very small grooves at the edges of the rectangular notch along the depth of the beam and in the same cross section as the pre-crack.

The propagation of the fracture was accompanied by a load drop for the fixed displacement that initiated the propagation. The load could be monitored at the same time as the displacement was slowly increased and the drop was a clear symptom that the fracture was propagating. Proceeding slowly was a key point in obtaining cracks of different depths in perspex, because the avalanche mechanism that would have finally broken the specimen could be avoided. The load drop is determined by the fact that when the fracture propagates the resisting cross section reduces, therefore increasing the flexibility of the beam. A more flexible beam will give larger displacements at smaller loads. Table 2.4 lists the characteristics of the perspex specimens and of the cracks produced in them.

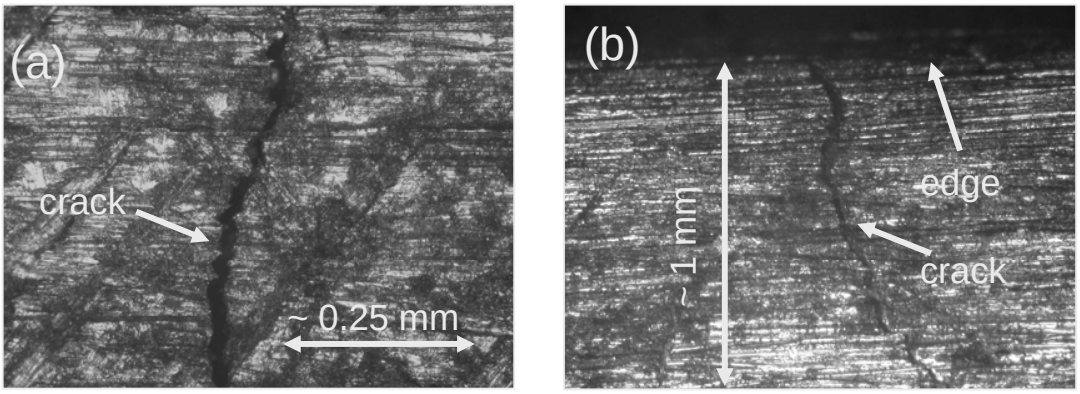

Figure 2.3: *(a) Microscope photograph of a segment of crack mouth through the width of specimen T-1 (the notch was removed). (b) Microscope photograph of a segment of crack side along the depth of beam T-1.*

2.3 Characterization of cracks

Both VAM and thermosonics exploit the motion of the crack interfaces to generate effects that can then be measured, as discussed in the Introduction. Therefore, it is important to know as precisely as possible the features of these cracks, so that they can be correlated to the measurements of respectively ultrasound modulation and surface temperature rise.

2.3.1 Measurement of crack opening

The degree of crack opening in the initial unstrained state was first assessed visually by means of images taken in a microscope as in Figure 2.3 (a) and (b). Such images provided an initial approximate measure of the crack mouth opening displacement (CMOD). However, a better understanding of the "breathing" of the cracks was achieved using a compliance method [14]. The principle exploited by this technique is that, in the region close to a small crack, the stress/strain characteristic varies as the crack changes its openness under the effect of loading. Therefore the compliance C is a function of the strain ϵ when measured on the crack or close to it. This is

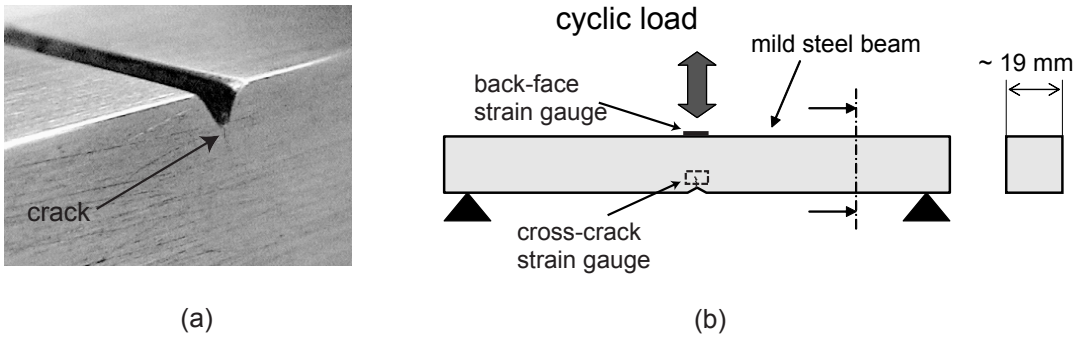

Figure 2.4: *(a) Photo showing the edge of a crack (where the cross-crack strain gauges were positioned) and, (b), three-point bending rig for the measurement of initial partial crack opening. The cross-crack strain gauge is placed on top of the crack for sensing the crack opening/closing.*

due to the local load path variation around the crack as the geometry (openness) of the crack changes [15]. Such path deviation would not occur once either of the the two limit states of the crack are reached, when the crack is fully open (becoming substantially equivalent to a notch) or fully closed (equivalent to absence of fracture).

The compliance test could be done using the three-point bending rig as in Figure 2.4. The crack opening behaviour was measured by testing with the crack at the bottom face of the beam (this configuration is the one shown in Figure 2.4), whilst closure was measured by reversing the beam so that the crack was at the top face and subject to compression when the beam was loaded. The strain across the crack, sensitive to the crack opening and closing, was measured by a foil strain gauge (Kyowa model KFG 120) and a reference foil strain gauge (same model) was positioned at the back of the beam, on the same cross section of the crack (back-face strain gauge). This arrangement is shown in Figure 2.4 (b). The load, the cross-crack strain and the back-face strain were all recorded during the tests. An example of the load and back-face strain signals is shown in Figure 2.5 during cycling at 5 Hz in the direction to close the crack of specimen CO (see list of specimens in Section 2.4). The cross-crack and back-face strain can be plotted against the load to obtain the graph of Figure 2.6. The full closure of the crack corresponds to an increased stiffness compared

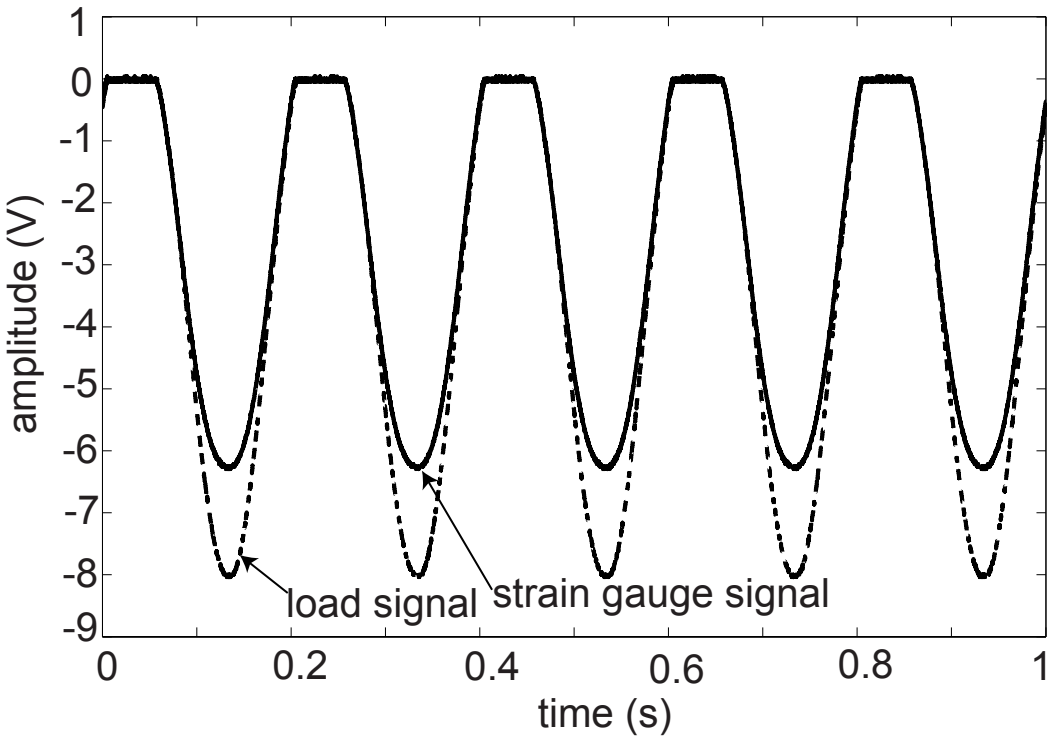

Figure 2.5: *Example of load and cross-crack strain vs time during cyclic loading at 5 Hz in the direction to close the crack of specimen CO. The oscillating hydraulic piston is contacting the beam only during part of its cycle hence providing an unloaded/unstrained reference condition within each period.*

to partial closure; the exact closure point was estimated, for this crack, at -1.1 kN corresponding to 220 $\mu\epsilon$ measured at the back-face strain gauge (dash-point line in Figure 2.6).

In Figure 2.7 the compliance (strain per unit load, calculated as the first derivative of the curves shown in Figure 2.6) measured by both strain gages on the cracked specimen T-2 is plotted as a function of the back-face strain for both directions of loading. The crack shows the "breathing" behaviour typical of a partially open crack in its initial unstressed status. It is noteworthy that, during the loading to close the crack (positive back-face strain), the compliance measured across the crack reaches the value of the constant compliance measured by the back-face strain gauge. This means that, for this crack, full crack closure was reached at around 275 $\mu\epsilon$ measured at the back face. However, it was not possible to state the exact strain at which the

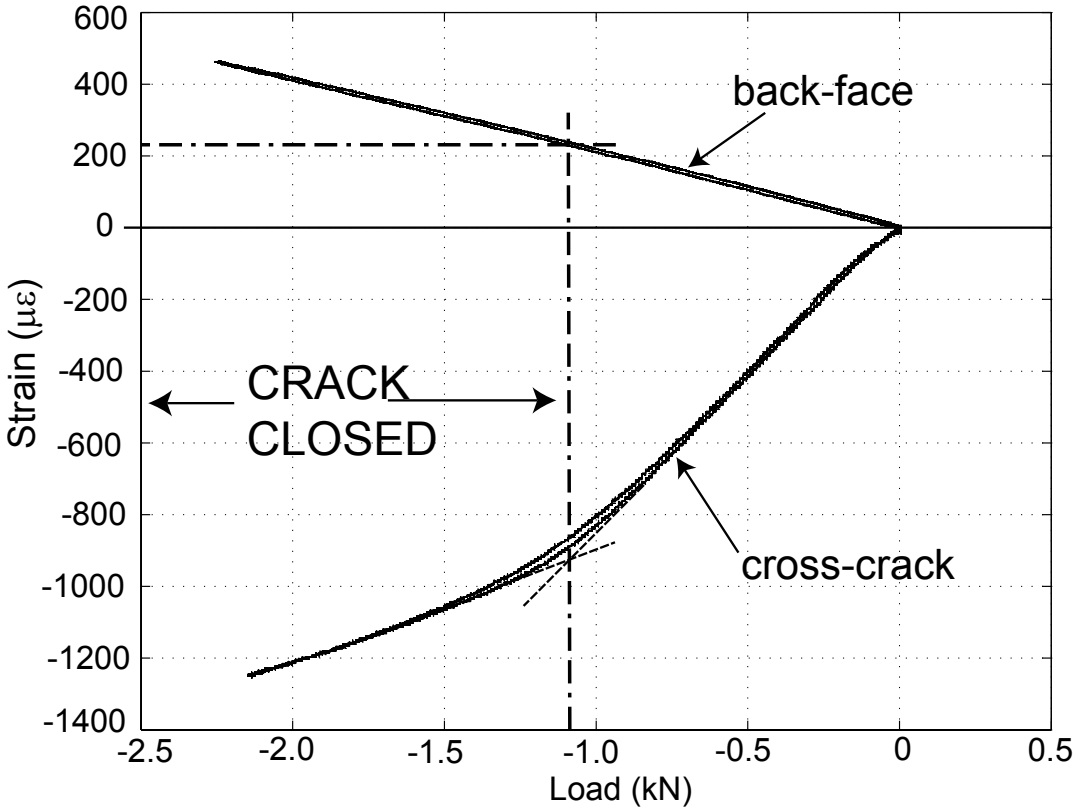

Figure 2.6: *Back-face and cross-crack strain vs load showing the sensitivity of the cross-crack strain to the closure of the crack in specimen CO.*

crack was fully open (negative back-face strain), since the compliance of the specimen did not reach a constant value before the maximum compressive load. The jump in the data close to zero strain was observed while a low load was applied to the specimen to close the crack. It is believed that this jump was the result of rocking of the specimen on its supports due to imperfect parallelism between the specimen and the supports. It is important to stress that the compliance tests were made at a fraction of the maximum load used to produce the cracks (100 $\mu\epsilon$ at the back-face corresponded approximately to 0.1 kN load on 10-mm-thick beams) and therefore it was assumed that the compliance tests neither changed the crack morphology nor propagated the crack significantly. For this reason, full crack opening was not always reached.

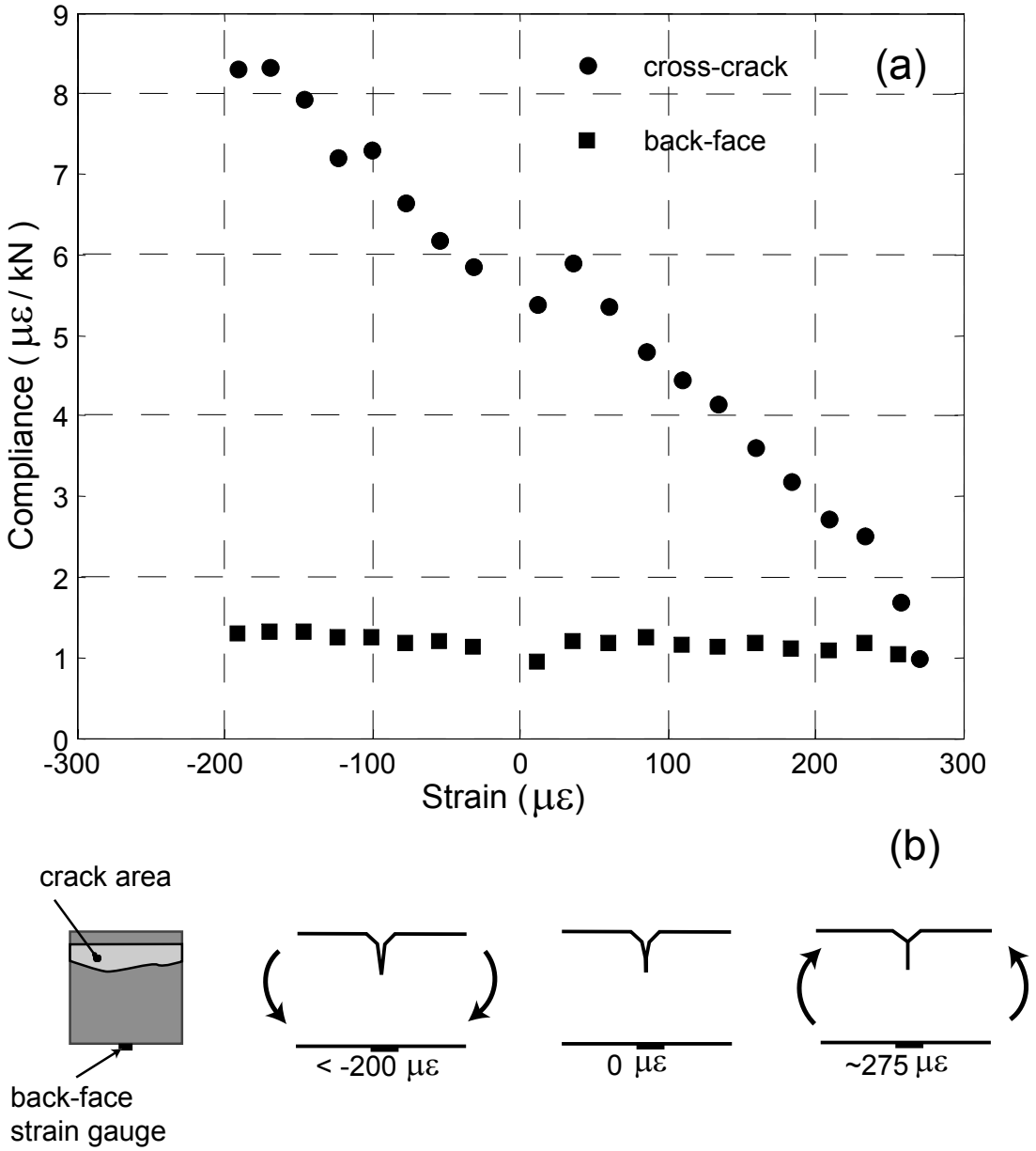

Figure 2.7: *(a) Compliance to loading of specimen T-2 (before removing the notch) as measured by the cross-crack and back-face strain gauges. The back-face strain gauge is insensitive to crack opening as shown by constant compliance. (b) Schematic illustration showing the back-face strain corresponding to full crack opening and full crack closure.*

2.3.2 Measurement of crack size

As mentioned earlier, an initial visual inspection revealed that the depth of the cracks at their edges over two opposite sides of the beams [as seen in Figure 2.4 (a)]

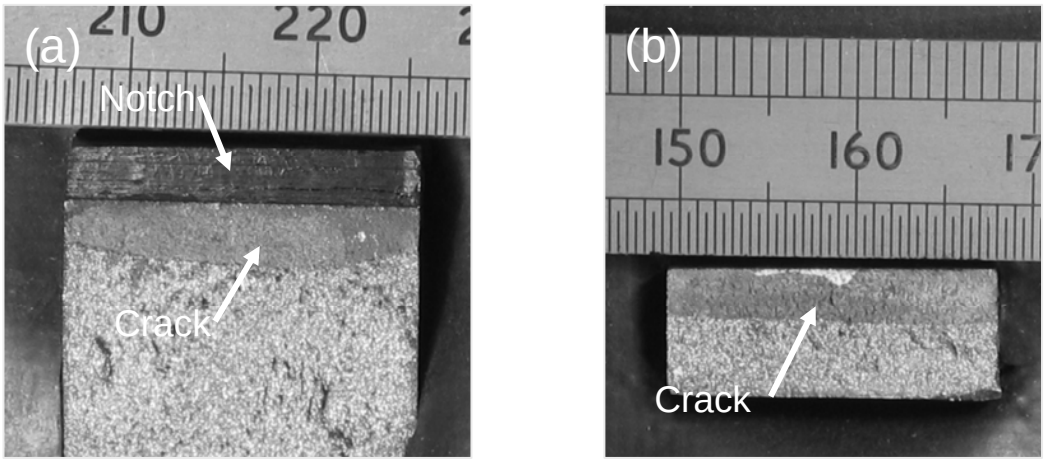

Figure 2.8: *(a) Cracked cross section of specimen S-1 (used in VAM) after breaking the specimen in two halves. (b) Cracked cross section of specimen T-1 (used in thermosonics) after breaking the specimen in two halves.*

was generally slightly different, implying that perfectly uniform propagation of the crack front from the root of the notch was not achieved. In some cases, the crack front deviated slightly out of the notched cross section of the beam as shown in Figure 2.8. In order to obtain a more accurate characterization of the profile of each crack, the samples were broken in half after the VAM/thermosonics experiments were completed. The crack depth at the edges and at the point of maximum depth (the crack profiles all exhibited a slight concavity) were measured by taking pictures of the crack profiles using a magnification factor of about 10 [Figure 2.8 (a) and (b)]. From these measurements the percentage of cracked cross section for each beam was estimated.

2.3.3 Measurement of crack roughness

Once the specimens were broken, the roughness of the crack surface and the average spacing between the asperities were measured using a Talysurf surface profiling machine, usually scanning along a 15 mm line across the width of the cracks. An example of such a measurement is provided in Figure 2.9. The roughness and the

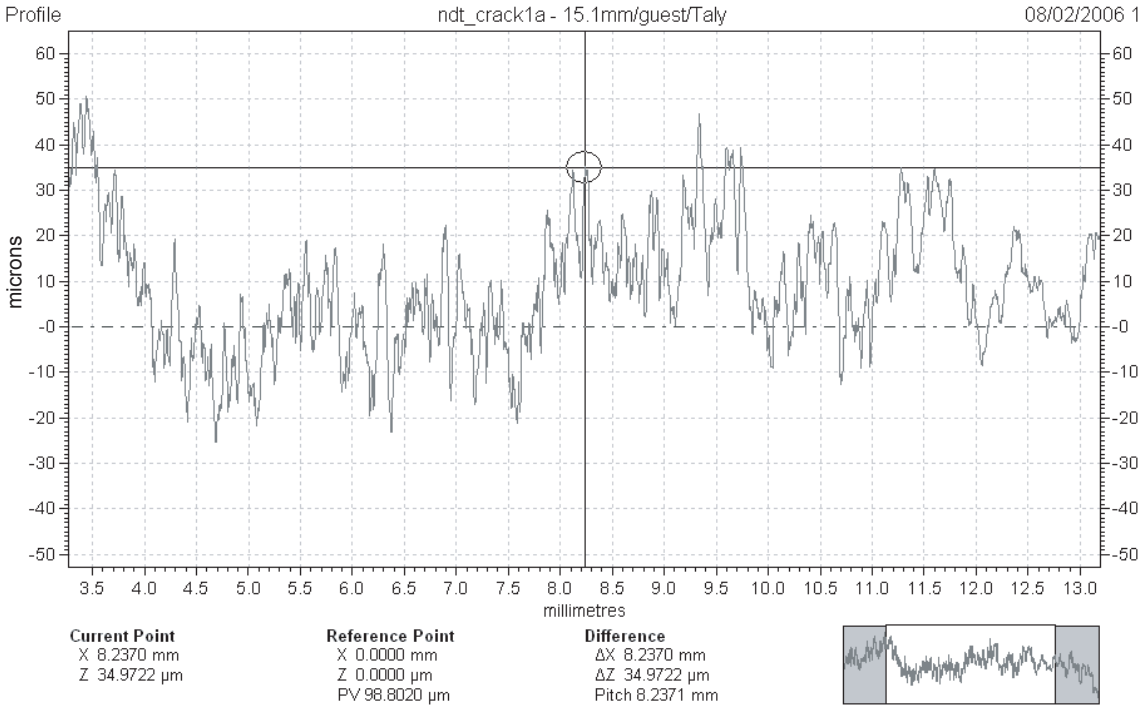

Figure 2.9: *Altimetric profile of the crack of specimen T-1 measured over a line by the Talysurf profiling machine.*

mean peak spacing were calculated after having filtered out the low spatial frequencies from the raw data acquired by the profiling machine. A cut-off frequency of 0.8 mm was used. This had to be done in order to achieve a correct description of the sharpness and spatial density of the crack asperities, having removed the spatial low frequency components given by the irregular shape of the crack mouth that can be seen in Figure 2.3 (a).

2.4 Characteristics of specimens and cracks

Three sets of mild steel cracked beams and one set of cracked perspex beams were produced in total. The steel beams were cut from square-cross-section lengths of cold-drawn mild steel. The perspex beams were cut from plates of dimensions $300 \times 300 \times 25$ mm.

2.4.1 Specimens used for VAM

The characteristics of the set of steel beams used in the VAM experiments are listed in Table 2.1. Steel beams of three lengths were used, 300 250 and 200 mm. These were labelled respectively "L", "M" or "S" and sequentially numbered. Three lengths were used in order to have the flexural modes of the beams at different frequencies. The notches had the same depth but different angles to understand if this could affect the formation of straight cracks. For beam M-1 the number of loading cycles before the fatiguing was stopped was as little as around 13 thousands, whilst for beam S-1 they were an order of magnitude higher nearly reaching 150 thousands. The number of cycles N for all beams was approximately in the range of $10^4 - 10^5$, meaning that the crack formation was not clearly low-cycle type (i.e. plastic strain driven) or high-cycle type (i.e. stress driven). Therefore, by the time of the appearance of the crack, a rather small plastic zone around the root of the notch was formed. This plastic zone was likely to be wider for specimen M-1 compared to specimen S-1. An extra specimen CO was cracked after the need of studying the effect of the initial partial crack opening on the ultrasound modulation in VAM became evident. This will be described later in Chapter 4. Only for this specimen the values of back-face strain corresponding to full crack closure and opening were measured. However, since the loading for specimen CO was done with settings similar to those used for all other specimens, it could be deduced that a similar crack "breathing" was occurring for all specimens.

2.4.2 Specimens used for thermosonics

The characteristics of the set of steel beams used in the thermosonic experiments for the study of the surface temperature rise prediction algorithm are listed in Table 2.2. Beams 300 mm long were cut and sequentially numbered (T-1, T-2 etc.). Notches 5 mm deep were used to initiate the cracks. The fatiguing was stopped many thousands cycles after the crack had initially formed in order to propagate the defects well into the depth of the material, for around 1 to 3 mm. The fatiguing

Table 2.1: *Characteristics of the cracked steel beams used in the VAM experiments.*

Beam	L-1	M-1	S-1	L-2	M-2	S-2	CO
Length (mm)	300	250	200	300	250	200	250
Thickness (mm)	19	19	19	19	19	19	19
Notch depth (mm)	2	2	2	2	2	2	2
Notch angle (deg.)	60	60	60	90	90	90	90
Flexural length (mm)	240	190	140	240	190	140	190
Load (kN)	6	6.5	7	7	8.3	8.5	7
N cycles (x10^3)	137	38.2	148	33.4	34.7	29.2	52.1
Crack depth at edge 1 (mm)	2.9	2.2	2.5	3.1	1.7	1.6	1.6
Crack depth at edge 2 (mm)	1.4	1.3	2.3	2.3	1.6	1.6	1.1
Max. depth (mm)	3.4	2.4	3.6	3.4	2.3	2.1	1.8
% cracked area	9.8	11.1	16.6	16.1	10.6	10.4	8.5
Crack breathing	Yes	Yes	Yes	Yes	Yes	Yes	Yes
Closure back-face strain ($\mu\epsilon$)	-	-	-	-	-	-	220
Aperture back-face strain ($\mu\epsilon$)	-	-	-	-	-	-	-30
Roughness (μm)	7.9	8.9	6.5	16	7.6	9.6	8.4
Mean Peak Spacing (μm)	183	230	199	353	171	218	202

loads were generally the same for all specimens. However the fatiguing was stopped after a larger number of cycles when a larger crack needed to be produced. After the cracks were produced, the beams were machined to remove the notches and a layer of material of the same thickness on the opposite side. The final thickness of the beams was 10 mm. Rather large cracks were generated, with sizes between 13% and 40% of the final cross-section area. The crack "breathing" measurements were performed to ensure that the machining did not alter drastically the partial opening state of the cracks hence resulting in tightly closed or fully open cracks. This would have been equivalent to having a continuum or an open slot (both would not heat up using thermosonics). A further reason to remove the notches was that of preventing

Table 2.2: *Characteristics of the cracked steel beams used in thermosonics for the study of the algorithm to predict the temperature rise.*

Beam	T-1	T-2	T-3	T-4	T-5	T-6	T-7
Length (mm)	300	300	300	300	300	300	300
Thickness (mm)	10	10	10	10	10	10	10
Notch depth (mm)	5	5	5	5	5	5	5
Notch angle (deg.)	90	90	90	90	90	90	90
Flexural length (mm)	240	240	240	240	240	240	240
Load (kN)	5.1	3.7	3.9	4.3	3.9	4.0	4.1
N cycles ($\times 10^3$)	44	86	57	39	70	69	56
Crack depth at edge 1 (mm)	3.8	2.7	1.5	0.9	2.8	2.7	1.6
Crack depth at edge 2 (mm)	2.7	2.4	1.6	0.7	2.8	2.8	2.0
Max. depth (mm)	4.2	3.1	2.0	1.4	3.4	3.5	2.5
% cracked area	40	29	18	13	28	31	22
Crack breathing	Yes	Yes	Yes	Yes	Yes	Yes	Yes
Closure back-face strain ($\mu\epsilon$)	450	275	400	160	300	350	100
Aperture back-face strain ($\mu\epsilon$)	-60	$\leq$-200	-150	-75	$\leq$-180	$\leq$-250	$\leq$-250
Roughness (μm)	6.0	7.0	6.6	6.8	7.0	7.1	6.4
Mean peak spacing (μm)	172	156	160	172	156	172	159

accumulation of black paint at the root of the notch when preparing the beams for IR measurements (this will be described in detail in Chapter 5). The non-uniformity of the paint on the notches can cause artifacts on the IR images. The combination of relatively thin beams with large "breathing" cracks allowed the relative motion of the contacting interfaces to produce an amount of heat large enough to measure a clear temperature rise during vibration.

The characteristics of the set of steel beams used for the study of the vibration required to reliably detect small cracks in metals using thermosonics are listed in

Table 2.3: *Characteristics of the cracked steel beams used in thermosonics to find the minimum detectable crack size.*

Beam	TT-1	TT-2	TT-3	TT-4	TT-5	TT-6	TT-7
Length (mm)	300	300	300	300	300	300	300
Thickness (mm)	17	17	17	17	17	17	17
Notch depth (mm)	1	1	1	1	1	1	1
Notch angle (deg.)	60	60	60	60	60	60	60
Flexural length (mm)	240	240	240	240	240	240	240
Load (kN)	8.0	8.2	8.0	8.2	8.3	8.3	8.3
N cycles ($\times 10^3$)	38	40	56	61	50	40	51
Crack depth at edge 1 (mm)	0.5	0.7	1.1	0.7	0.3	0.6	0.6
Crack depth at edge 2 (mm)	0.5	0.4	1.0	0.5	0.6	0.5	0.4
Max. depth (mm)	0.9	0.8	1.5	0.7	0.7	1.0	1.0
% cracked area	4.5	3.5	7.8	2.9	3.6	4.8	4.9
Roughness (μm)	6.3	6.0	6.9	6.2	6.9	6.9	6.6
Mean peak spacing (μm)	152	162	182	188	199	180	165

Table 2.3. Beams 300 mm long were cut and sequentially numbered (TT-1, TT-2 etc.). Shallower (1 mm) and sharper (60 degrees) notches were used. The fatiguing was stopped soon after the presence of a crack became clear in the microscope. This ensured that smaller cracks were produced than those of the previous batch. After the cracks were produced, the notches and the same thickness on the other side of the beams were removed for the same reasons explained in the previous paragraph. In this way, cracked beams with cracks embedded into initially thicker specimens were obtained. These comparatively stiffer beams with cracks of smaller dimensions (approximately 3% to 10% of the total cross-section area) were ideal to carry out a study aimed at establishing criteria for the reliable crack detection of small defects (see Chapter 6).

Table 2.4: *Characteristics of the cracked perspex beams.*

Beam	P-1	P-2	P-3	P-4
Length (mm)	300	300	140	140
Thickness (mm)	25	25	25	25
Notch depth (mm)	6	7	5	6
Notch width (mm)	1	1	1	1
Flexural length (mm)	280	280	130	130
Crack depth at edge 1 (mm)	2	3	5	18
Crack depth at edge 2 (mm)	0	1	5	18
Roughness (μm)	0.65	0.81	0.45	0.57

2.4.3 Perspex specimens

The characteristics of the set of perspex beams used both in the VAM and thermosonics experiments are listed in Table 2.4. The beams were sequentially named P-1, P-2 etc.. These specimens were not used extensively in this work. In VAM, perspex offered the possibility to carry out some experiments using cracked specimens with a material Q-factor much lower than metals, and to compare this with the predictions (see Chapter 4). In thermosonics, perspex cracked beams were used initially when the excitation was not optimized and high values of vibration amplitude could not be achieved. Since the thermosonic signal could not be measured in metals at low vibration levels (see Chapter 5), the perspex beams were used to demonstrate the thermosonic method of NDT. The low thermal conductivity coefficient of perspex allowed the heat to build up at the crack hence generating a measurable temperature rise even at low vibration amplitudes.

In this Chapter the production of sets of laboratory specimens with calibrated cracks has been reviewed. The aim at this stage of the research was to produce specimens with different cracks of known characteristics. However, the propagation of straight cracks in the desired direction resulted difficult to control. For this reason, the

specimens were broken in half after the completion of the experiments to reveal the exact shape and size of the defects.

Chapter 3

Damping measurements

3.1 Introduction

As seen in Chapter 2, the morphology of fatigue cracks can be characterized by measuring several parameters including the opening of the crack mouth, the shape of the crack front, the crack size and the crack roughness. However, fatigue cracks can also be characterized by measuring the effect of their presence on the vibration of a body. The presence of a crack in a structure is known to change fundamental vibration parameters like the resonance frequency [16], and the vibration damping [17]. These effects are currently employed as working principles in various NDT applications for the detection of cracks [18, 19]. In this study, the vibration damping due to the presence of a fatigue crack in the beams will be measured. This extra-damping is introduced in the specimens by the cracks in addition to the baseline material and joints/supports damping. The experimentally obtained estimate of this additional damping will be exploited throughout this work for several purposes. First, it will provide an initial estimate of the relative crack severity among cracked beams belonging to the same batch. If similar loading conditions are maintained during the fatiguing process of a group of specimens, a similar degree of initial crack opening and a similar crack profile can be expected. In this case, the size of the cracks will be directly correlated to the crack damping. Second, it can be used as a means of

predicting the thermosonic temperature rise caused by the local energy dissipation at the crack during vibration. This is theoretically possible since the crack damping is related to the ability of the cracks to dissipate mechanical energy into heat. Third, the measurement of damping can be simply used to detect the cracks. A by-product of these measurements will be the possibility to compare the sensitivity of the damping measurement method to those of VAM and thermosonics. It will be interesting to prove whether either of the two new techniques shows increased sensitivity over the traditional damping measurement method.

In metallic damped structures subject to vibration, it is known that the stress/strain relation is non-linear and exhibits a loop behaviour known as *hysteresis* [20]. The area included in the σ/ϵ loop represents the energy dissipated per cycle per unit volume ΔV [20]:

$$\Delta V = \oint \sigma d\varepsilon. \tag{3.1}$$

The specific damping coefficient Ψ is defined as ΔV normalized to the maximum strain energy, V, stored in the unit volume during the cycle:

$$\Psi = \frac{\Delta V}{V}. \tag{3.2}$$

The study of the hysteresis mechanisms in materials and structures is the subject of ongoing research by physicists and engineers [21–25]. In engineering applications, simplified models of hysteresis are widely used. *Hysteretic* damping (also known as structural or linear damping) is a simple model of damping which approximates the hysteresis loop with an ellipse by assuming a constant phase delay between stress and strain. The loss factor η is introduced in the steady-state forced vibration analysis of hysteretically damped structures and is a measure of the phase delay α between stress and strain [26]. Making use of the complex elasticity modulus $\mathbf{E}$ it is:

$$\eta = \frac{Im(\mathbf{E})}{Re(\mathbf{E})} = \tan\alpha. \tag{3.3}$$

The area of the ellipse (ΔV) of the hysteresis loop in the stress-strain coordinate system can therefore be given, in the case of structural damping, as a function of the loss factor:

$$\Delta V = \pi\epsilon_0^2 Re(\mathbf{E})\eta, \tag{3.4}$$

where ϵ_0 is the maximum strain in the cycle. Since the maximum energy stored per unit volume is

$$V = \frac{Re(\mathbf{E})\epsilon_0^2}{2}, \tag{3.5}$$

the specific damping coefficient Ψ for hysteretic damping can be expressed in terms of η:

$$\Psi = \frac{\Delta V}{V} = 2\pi\eta \tag{3.6}$$

and is independent of the frequency of the exciting force.

In the study of vibrational damping it is common to refer to other parameters such as the logarithmic decrement of vibration, δ, and the Q-factor, Q. The first measures the decay rate of a vibration mode in the time domain [27], the second is a measure of the sharpness of the resonance peaks of a frequency response function in the frequency domain [28]. For the freely decaying mode N, after a number of cycles i, the logarithmic decrement of vibration is defined as [27]:

$$\delta_N = \frac{1}{i} \ln \frac{A_0}{A_i} \tag{3.7}$$

where A_0 and A_i are respectively the amplitudes of the vibration at the onset and after i cycles. The relation between the logarithmic decrement of vibration and the loss factor is [27]:

$$\eta_N = \frac{\delta_N}{\pi}. \tag{3.8}$$

For the forced excitation case, if a system is excited around the resonance frequency of the mode N, f_N, the Q-factor is given approximately by [28]:

$$Q_N = \frac{f_N}{f_1 - f_2} \tag{3.9}$$

where f_1 and f_2 are the two half-power points. Provided that the damping is not too large, the Q-factor is simply related to the loss factor [27]:

$$\eta_N = \frac{1}{Q_N}. \tag{3.10}$$

.

The extra damping introduced in each beam by the presence of a fatigue crack is generally dependent on the crack size and its morphology (including the size and shape of the plastic zone around the crack tip) and on the pattern and magnitude of the stress distribution on and around the crack when the specimen is vibrated (i.e. the vibration mode shape and amplitude). The idea in this work is to measure the crack damping as the difference between the loss factor measured for one cracked beam in the mode N and the loss factor for an uncracked beam in the same mode N:

$$\eta_{crack,\,N} = \eta_{cracked\ beam,\,N} - \eta_{uncracked\ beam,\,N}. \tag{3.11}$$

The vibration loss factor η is the chosen reference parameter to be measured.

3.2 Specimens used for VAM

Damping tests on the VAM specimens were carried out for a comparison between damping and VAM as NDT methods for the detection of cracks. A simple method of measuring vibration damping is by exciting the structure with an impact, and then analysing the following vibration decay. The position of the impact force, its direction and the duration of the impulse will determine the modes and the maximum frequency excited [28]. For the VAM specimens, the damping was measured by impacting the specimens with a small steel ball of diameter 5 mm at the middle of the beams in the perpendicular direction (see Figure 3.1). The ball was suspended so that it could swing freely as a pendulum. The out-of-plane velocity component of the structure response was measured using a laser vibrometer model Polytec OFV 505 pointed towards the crack. The beams were supported by taut strings at the nodal lines of the 1st bending mode. Hence, the crack damping measurements for the VAM specimens were optimized for this mode since its damping was virtually unaffected by the damping introduced by the supports. The decay following the impact was recorded using a digital storage oscilloscope. The vibration of the 1st bending mode was then extracted from the recorded time trace using a digital low-pass filter. Plotted on a logarithmic scale, the amplitude decay of this mode is

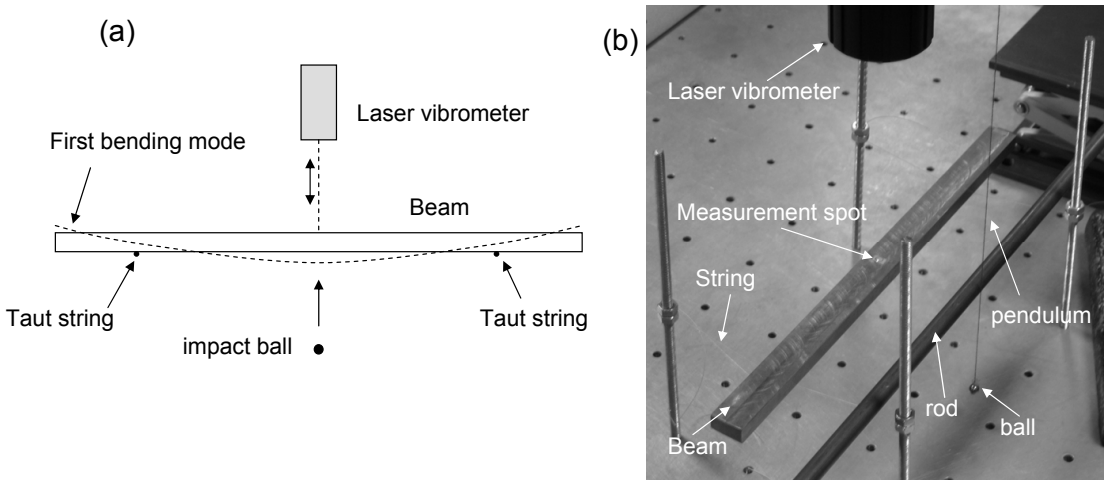

Figure 3.1: *(a) Schematic representation of the multi-mode impact damping measurement optimized for the 1st flexural mode. (b) Picture showing the implementation of the measurement.*

linear and from the slope of this line, the damping constant of the mode can be calculated [26].

The results of 10 repeated damping measurements on the specimens used in the VAM investigation (beams of Table 2.1) are shown in Figure 3.2. The average loss factor of the 1st bending mode, η_1, is plotted vs the size of the crack given as percentage of the total cross-section area. The uncertainty on the mean value is expressed by plus or minus one standard deviation. The measurement of the area of the crack was taken after breaking the specimens. Specimen S-1 exhibits a relatively higher uncertainty (order of 15%) than the other specimens; this could depend on the morphology of this particular crack. These results show that the loss factor tends to increase with increasing crack severity, even though the trend is clearly nonlinear. This has been already observed in the literature [17]. From a practical point of view this implies that it would be increasingly more difficult to detect cracks smaller than 10% of the original cross section using the damping test. The crack of specimen M-2 (10.6% crack) is already barely detectable, with the average of the repeated measurements very close to the baseline damping measured for the undamaged specimens (dashed line in Figure 3.2). This could possibly be explained by a larger initial crack opening

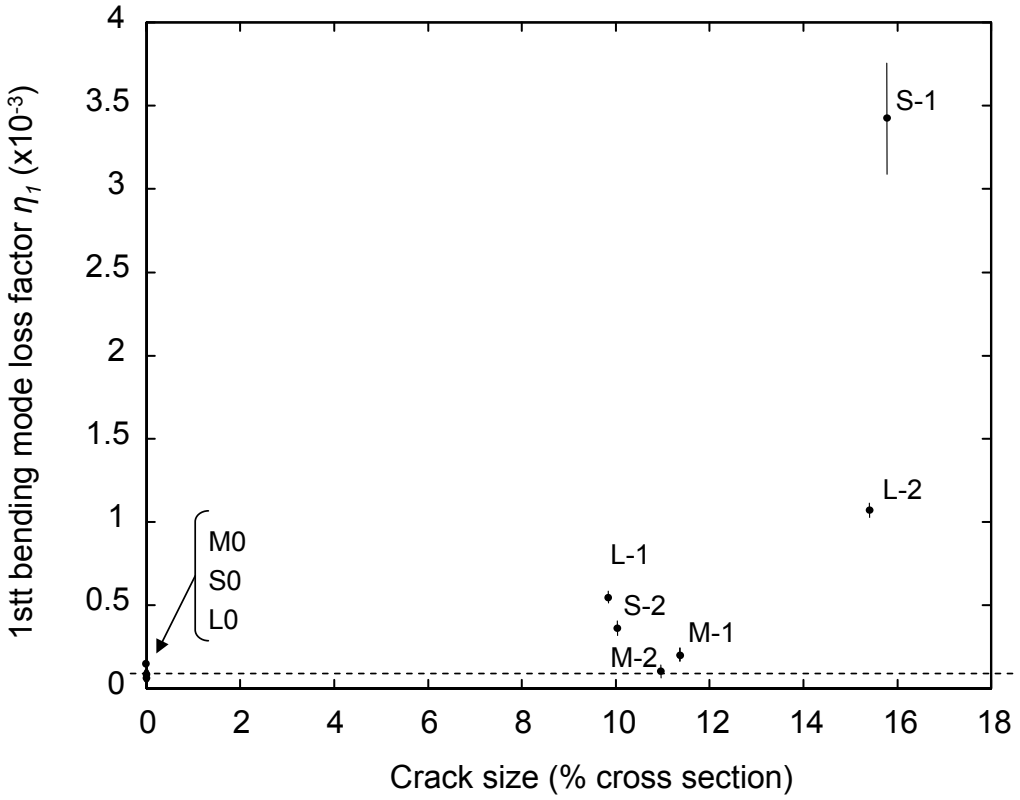

Figure 3.2: *Comparison between the 1st bending mode loss factor and the actual crack size expressed as the percentage of the total cross-section area for the specimens of Table 2.1. The vertical line through each point represents plus/minus the standard deviation for 10 repeated measurements. The dashed line represents the baseline damping level for the undamaged beams labelled M0, S0 and L0 (average of measurements for 3 uncracked beams).*

compared to the other cracks of similar size.

The same measurements were taken on two perspex samples, one uncracked and one cracked (specimen P-2 of Table 2.4). The results are given in Table 3.1. Both the loss factors of the 1st and the 3rd flexural modes (the supports were optimized for either mode) were calculated from the impact decays. The cracked specimen shows substantially the same damping as the uncracked specimen. This is due to the baseline material damping which is higher for perspex than steel, hence not allowing the cracked specimens to be differentiated. In addition, the crack surface in the perspex specimens is characterized by a much smoother profile compared to

Table 3.1: *Results from damping tests carried out on two perspex beams, one cracked (specimen P-2 of Table 2.4) and one undamaged. The loss factors of the 1st and 3rd bending modes were measured. The standard deviation obtained over 10 repeated measurements is given in brackets.*

	Undamaged	Cracked
$\eta_1(\times 10^{-3})$	51.2 ($sd = 1.0 \times 10^{-3}$)	48.7 ($sd = 0.6 \times 10^{-3}$)
$\eta_3(\times 10^{-3})$	36.5 ($sd = 0.8 \times 10^{-3}$)	36.3 ($sd = 0.9 \times 10^{-3}$)

a crack in steel (this can be explained by static loading instead of cyclic loading, see section 2.2). If we assume that a major portion of the additional crack damping is generated by friction at the asperities [29], it can be expected that cracks with a few smooth asperities would dissipate less energy during vibration.

3.3 Specimens used in thermosonics

The reason for conducting damping tests on the thermosonics specimens is twofold: first, to provide an estimate of the severity of the defects prior to breaking the specimens and, second, to be used as an input for the calculation of the heat dissipated at the crack during vibration. We will see that the latter task requires additional damping tests compared to those performed on the VAM specimens. In principle, the specimens would have to be vibrated at the same amplitude levels and in the same modes which are likely to be excited in the thermosonic tests (strain in excess of 10-20 $\mu\epsilon$ at frequencies up to 200 kHz, see Chapter 5 for further details). This could have been achieved by using the thermosonics acoustic horn as the exciter for the damping tests as well. However, the coupling between the horn and the beams would have introduced a high level of damping in the system, thus compromising the ability to measure the damping due to the crack. In addition to this, there would have been the problem of the non-reproducibility of the vibrations excited by the horn, making the damping measurements even more problematic. It was therefore

concluded that the horn excitation was not viable, and alternative damping tests were arranged to achieve a measurement of crack damping at large strain and high frequencies.

3.3.1 Initial multi-mode impact tests

As mentioned earlier, the impact test has the potential of exciting multiple modes simultaneously, hence allowing the damping to be retrieved for several modes at the same time from the analysis of a single vibration decay. Therefore, the initial damping measurements for the thermosonics specimens (specimens T-1 to T-7 in Table 2.2) were carried out using the same setup used for the VAM specimens [Figure 3.1 (a) and (b)]. The impacts were produced using a small steel ball of diameter 5 mm directed towards the middle of the beams and in the perpendicular direction. In Figure 3.1 (b), it can be seen that the steel ball is attached to a thread which bends around an horizontal rod, as the pendulum is swung, to provide the impact on one of the beams of Table 2.2. In this way, odd flexural modes of the beams were excited up to around 70 kHz, since the ball could produce a relatively short impulse. The out-of-plane velocity component of the structure response was measured using the laser vibrometer . The decays following each impact were recorded using a digital storage oscilloscope and then processed as a time-frequency plot using the short-time Fourier transform. This allows the modes of the structure to be separated in frequency, while their decay can be measured in time [30]. As discussed in the previous section, it is then possible to retrieve the mode loss factor, as the decay slope of each mode plotted on a logarithmic scale is a measure of the loss factor of that mode.

The results of these measurements are reported in Figure 3.3. The odd flexural modes up to the 19th (at around 70 kHz) could be excited. The damping of the uncracked beam was clearly lower than that of all the cracked beams at all frequencies. The severity of the cracks correlated well with the average level of damping measured for each specimen; for example beams T-1 (40% crack) and T-4 (13% crack) respectively exhibited the highest and lowest loss factors among the cracked

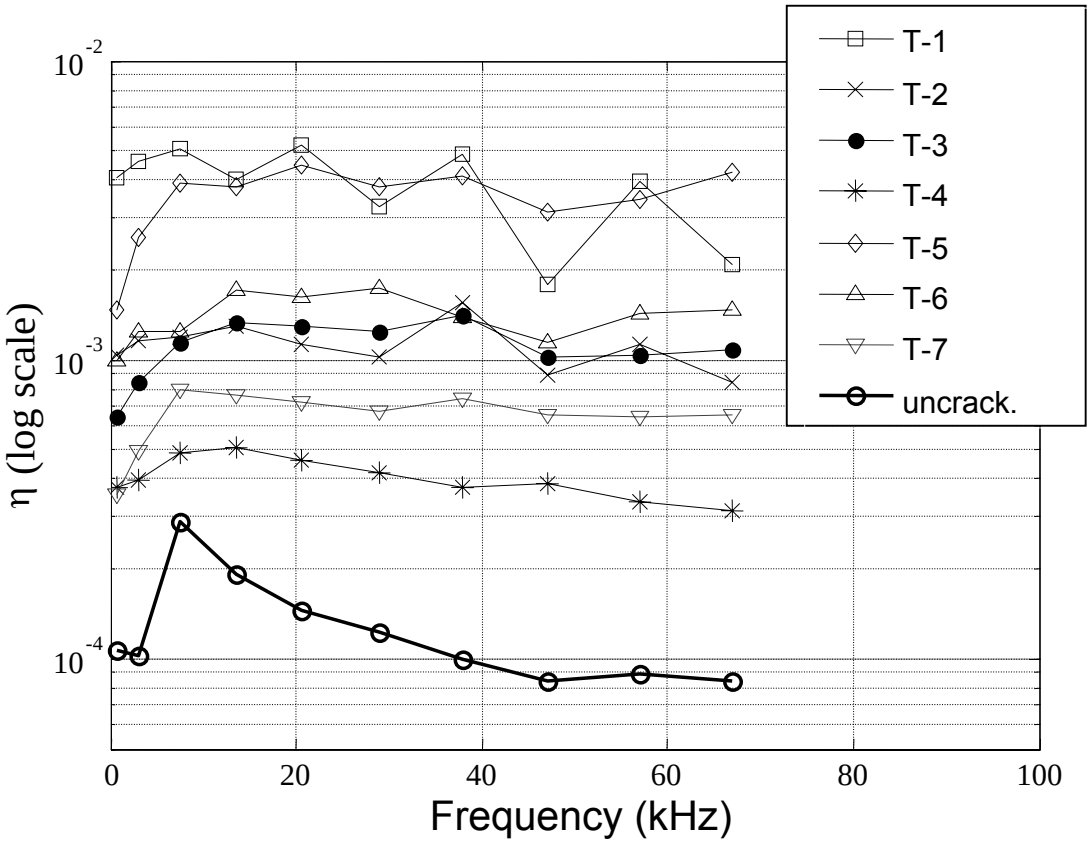

Figure 3.3: *Measured loss factors and natural frequencies of the first 10 odd flexural modes for the set of beams used in the prediction of the thermosonic signal (specimens T-1 to T-7 in Table 2.2).*

beams. However, using this setup, it was never possible to excite vibrational strain amplitudes as high as those obtained in the thermosonic tests for the flexural modes of order higher than 7 (which has a resonance frequency at around 13 kHz). For such high order modes, the amplitudes were up to a factor of 100 lower than the typical amplitudes excited in the thermosonic tests. Furthermore, most of the vibrational energy excited in thermosonics is typically within the interval 40 - 120 kHz, whereas in these damping tests the higher amplitudes are all excited at low sonic frequencies. Bovsunovsky [29] and Goken [31] have recently found that cracked structures can exhibit strong amplitude dependent vibration damping and the vibration damping can tend to decrease with increasing vibration amplitude, in contrast to classical structural damping which usually increases with increasing vibration amplitude.

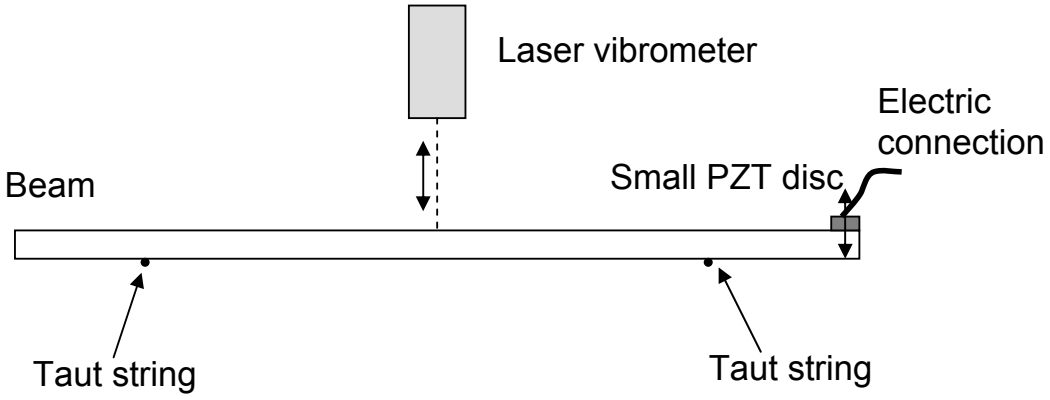

Figure 3.4: *Schematic representation of the setup for the measurement of the crack damping using forced vibrations.*

These findings further motivate the necessity of testing the crack damping using other methods. In the next phase, forced vibration damping tests were conducted.

3.3.2 Forced vibration tests

The testing rig shown in Figure 3.4 was devised in the attempt to achieve more vibration strain in the range of frequencies previously excited and, possibly, at higher frequencies. In the forced vibration tests, the oscillating force was applied at the end of the beams by a small PZT disc driven at the chosen frequency by means of a power amplifier (Macro-Design Wave-Maker) connected to a signal generator (Agilent 33220A). The use of small PZT discs ensured that the additional damping introduced by bonding them to the beams was negligible. The vibration could be tuned to the resonances of the odd flexural modes of the beams in the range 20 - 90 kHz (the power amplifier could not operate below 20 kHz, whereas the flexural resonances above 90 kHz could not be separated from other more complex modes [32]). Unfortunately, however, the target thermosonic vibration amplitude (10 - 20 $\mu\epsilon$) could not be reached; a vibrational strain in the range 1 - 2 $\mu\epsilon$ was generally achieved for all specimens. This was due to the small force that the PZT discs could transmit to the test-piece. The computation of the vibration loss factors was carried out using the half-power point method (equation 3.9) sweeping the

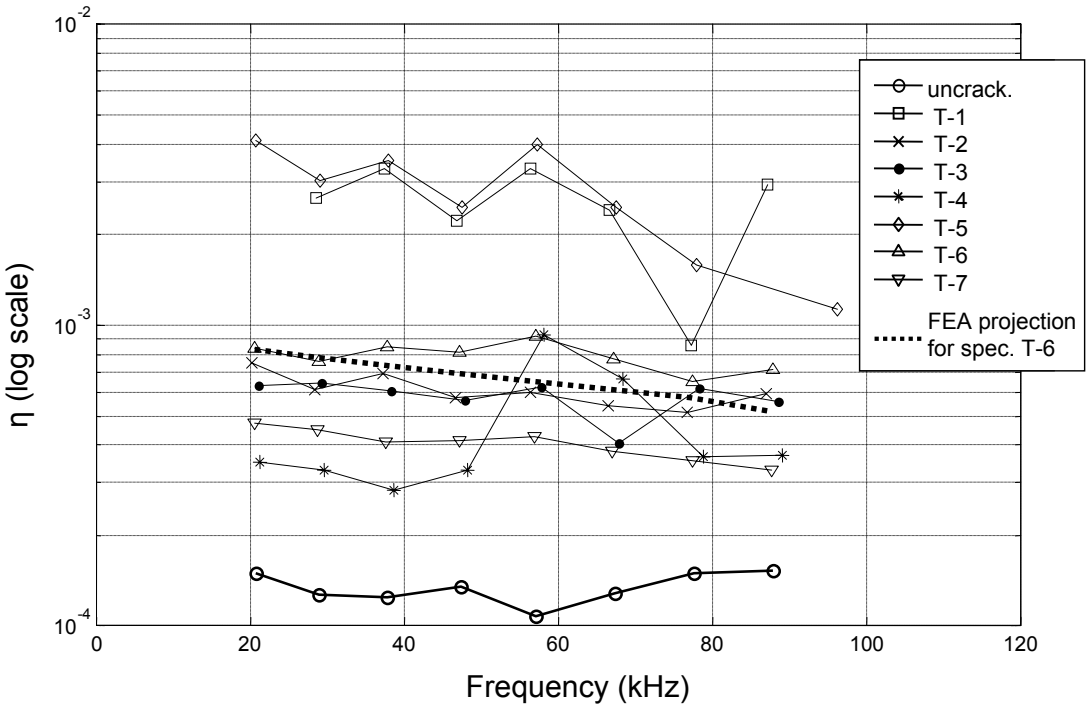

Figure 3.5: *Loss factors as a function of frequency/mode-shape measured using the setup of Figure 3.4. The typical strain amplitude was between 1 and 2 $\mu\epsilon$ at all frequencies. The dotted line is the calculated variation of the loss factor vs frequency for specimen T-6, on the assumption that ΔV is constant with frequency.*

excitation frequency around the resonance frequencies of the odd flexural modes to find the half-power points. These results are shown in Figure 3.5. Since the desired strain could not be achieved, these measurements could not be used directly to predict the heat dissipated at the crack during vibration in thermosonics. However, the analysis of the results obtained in the forced excitation tests produced other important considerations.

Bovsunovsky [29] and Goken [31] reported that the energy per unit strain, ΔV, dissipated per cycle by a crack during flexural vibrations in beam-like structures can reasonably be assumed to be independent of frequency even though it can exhibit strong variation with amplitude. This is reasonable, considering that, for a given thickness, the curvature of a beam during bending vibration (which drives the opening and closing of a crack) is directly proportional to the strain but does not depend

Table 3.2: *Results from the finite-element modal analysis of the beams used in the prediction of the thermosonic signal (specimens T-1 to T-7 of Table 2.2). The mode shapes were mass-normalized. The strain at the crack position (known as back-face strain from Chapter 2) is the strain in the mass-normalized modes. The strain energy of the mass-normalized modes is calculated from the value of the natural frequency [$V_N = \frac{1}{2}(2\pi f_N)^2$].*

Flexural mode N	Natural frequency f_N (Hz)	Back-face strain ($\times 10^6 \mu\epsilon$)
1	590	2.94
3	3136	13.7
5	7523	32.4
7	13466	56.7
9	20655	84.9
11	28808	115
13	37685	147
15	47097	179
17	55985	212
19	66964	244
21	77200	275
23	87424	300

on the mode order. In other words, the opening/closing status of the crack is fixed as long as the same strain is reached irrespective of the flexural modes excited. This scenario implies a reduction of η_N with frequency, as the strain energy stored in each mode per unit strain squared, V_N, increases with increasing order N (see equation 3.6). The analytical formula for the strain energy in pure bending of beams could be used to calculate V_N [33]:

$$V_N = K'_N \int_0^{L_s} [\frac{d^2 y_N(x)}{dx^2}]^2 dx, \tag{3.12}$$

where K'_N is a constant which depends on the natural frequency of the mode, on the geometry of the crosssection and on the material properties, and $y_N(x)$ is the mode shape of the beam (of length L_s) along the coordinate x. However, this would only

give accurate results up to the 3rd or 5th flexural mode [33] for thick beams, such as those used in this study. Given the aspect ratio of the beams, the contribution from shear stresses to the overall strain energy is significant starting from approximately the 5th flexural mode [34]. Thus, a finite element analysis (FEA) is required to calculate the appropriate values of V_N. The principal results of the modal FEA carried out for an uncracked beam of the same geometry as the beams used in the prediction of the thermosonic signal (specimens T-1 to T-7 of Table 2.2) are shown in Table 3.2. The cracked and uncracked specimens will have slightly different natural frequencies and, due to the loss of stiffness generally produced by cracks, the strain energy of the cracked beam will be slightly lower than that of the uncracked beam. However, for small cracks, these effects are small so that ignoring such changes can be considered a good enough approximation [35]. The mode shapes obtained from the modal FEA were mass-normalized, hence the strain energy in each mode could be calculated as $\frac{1}{2}\omega_N^2$, with $\omega_N = 2\pi f_N$, where ω_N^2 and f_N are respectively the eigenvalue and the natural frequency of the mode N [28]. The finite element strain energy per unit strain squared is simply obtained by dividing these values of strain energy by the finite element strain at the crack position in the mass-normalized modes. In Figure 3.5, the loss factors generally follow a decreasing trend with frequency, more pronounced for specimens T-1 and T-5 which had two of the deepest cracks. The dashed line (which refers to specimen T-6) was calculated by evaluating the energy dissipated per cycle per unit strain amplitude in the mode N using the definition of loss factor,

$$\Delta V_N = 2\pi\eta_{cracked\ beam,N} V_N, \tag{3.13}$$

and considering the measured loss factor at the lowest frequency ($\eta_{cracked\ beam,9}$ with mode 9 at around 20 kHz) and the strain energy per unit strain amplitude (V_9) which was obtained from the eigenvalue FEA of an uncracked beam described earlier. The loss factors in the higher modes for specimen T-6 were then obtained from equation 3.13 using this initial (constant) value of energy dissipated per cycle and unit strain amplitude (ΔV_9) and the values of strain energy per unit strain amplitude obtained from FEA in each mode of order higher than 9. The trend of the dotted line in Figure 3.5 broadly follows the measured data, confirming that the assumptions of

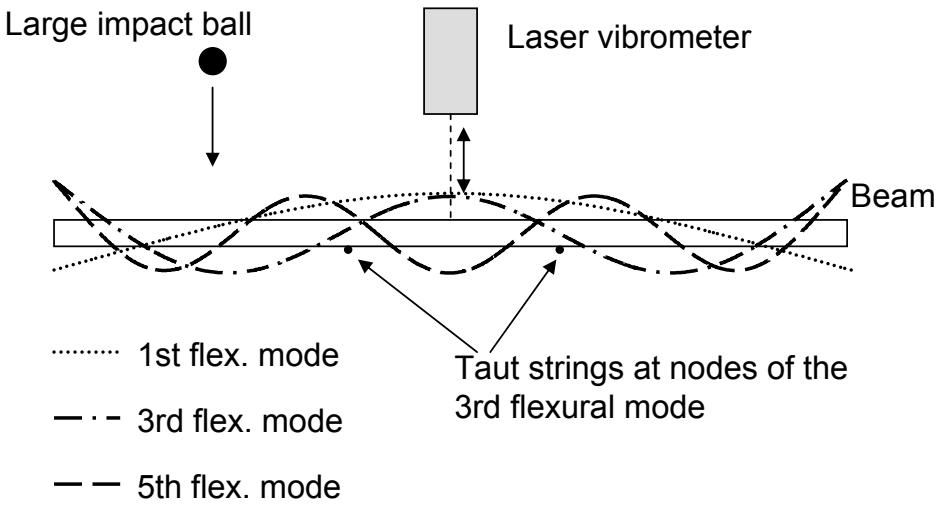

Figure 3.6: *Schematic representation of the setup for the measurement of the crack damping as a function of strain in the 3rd flexural mode.*

Bovsunovsky and Goken provide a reasonable representation of the behaviour of the cracks used in this investigation. Therefore, the loss per cycle, ΔV, could be measured in any odd flexural mode of the beams that is possible to excite up to strain amplitudes of the same order as the thermosonic amplitudes. Then, these values of ΔV could be used in equation 3.13 to compute the loss factors η at high amplitudes in any other odd flexural mode. This process would, in the end, give an estimate of crack damping at high amplitudes and high frequencies as required to calculate the exact amount of heat dissipated at the crack during vibration in thermosonics. Therefore, it was only necessary to excite high strains in one mode at low frequency, where it is easier to achieve higher strain amplitudes.

3.3.3 High amplitude impact tests

The arrangement in Figure 3.6 was devised to selectively excite the 3rd flexural mode of the beams to investigate the amplitude dependence of the energy dissipated by the crack in one cycle, ΔV. The 3rd flexural mode was chosen since (a) its resonance is at around 3 kHz, and hence is low enough to be easily excited by impact from a large steel ball (diameter 15 mm) and (b) its vibration maxima are conveniently

located close to the nodes of modes 1 and 5 (also represented in Figure 3.6); it was therefore easy to excite mode 3 with little contamination from the adjacent odd flexural modes. The even flexural modes 2 and 4, even though excited, did not contribute to vibrating the crack as they have a vibration node at the middle of the beams. The beams were supported on tiny (diameter 0.5 mm) taut strings positioned at the vibration nodes of the 3rd flexural mode, which was typically excited up to around 30 $\mu\epsilon$ (hence at amplitudes of the same order of those usually recorded in the thermosonic experiments). After the impacts, the vibration decayed freely and the velocity was measured by the laser vibrometer and recorded using a storage oscilloscope. A typical time-history of vibration decay is shown in Figure 3.7 (a); the corresponding FFT is given in Figure 3.7 (b). After filtering out the decay of the 3rd flexural mode [Figures 3.7 (c) and (d)], the loss factors $\eta(\epsilon)$ were calculated for decreasing vibration amplitudes by considering the logarithmic decrement of vibration (calculated according to equation 3.7) in successive slices of the vibration transient [these are shown in Figure 3.7 (c)].

The results of this procedure are reported in Figure 3.8 for all specimens. The maximum strain excited was around 30 $\mu\epsilon$ peak for all specimens. A strong amplitude dependence of η, with decreasing damping for increasing strain, was found only for specimen T-1 which had the biggest crack and the largest initial partial crack opening (lowest full opening strain as seen in Table 2.2). A much less severe reduction of η with increasing strain was measured for crack T-5, which was also relatively large. Specimens T-2, T-3 and T-6 showed a moderate increase of crack damping with increasing amplitude whilst the cracks of specimens T-4 and T-7 showed virtually constant damping. These results, obtained from the excitation of a single low frequency flexural mode, could be used to estimate the damping in any odd flexural mode using the assumption validated above that, at a given strain level, the energy loss per cycle (ΔV) is independent of frequency. Often, strain larger than 30 $\mu\epsilon$ was reached in the thermosonic tests; in such circumstances the value of η measured at the highest strain available for that specimen was used to represent the loss factor at higher amplitudes.

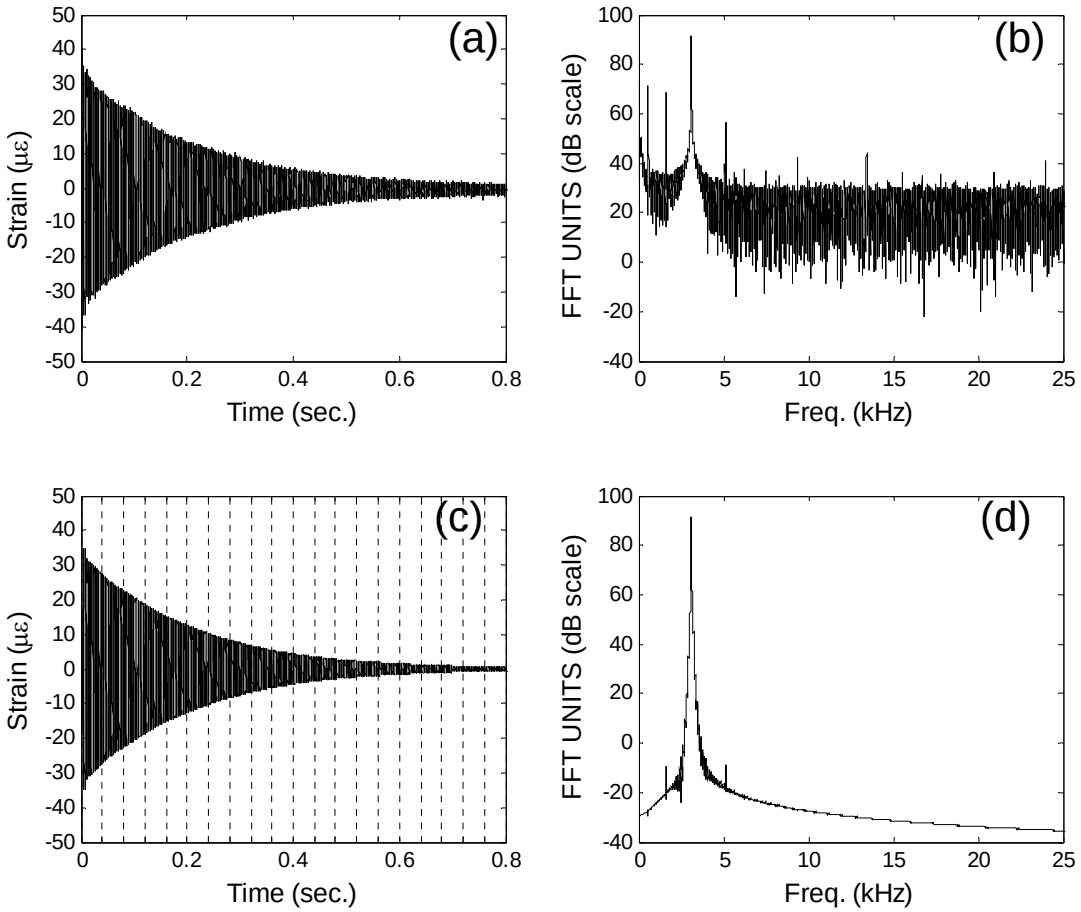

Figure 3.7: *Steps in the estimation of η as a function of time from the impact tests of Figure 3.6. (a) Time trace of the vibration decay after an impact on specimen T-7 and, (b), its Fourier transform. (c) Vibration decay of mode 3 of specimen T-7 after band-pass filtering and, (d), corresponding Fourier transform. The sections in (c) show the time step used to calculate η from the logarithmic decrement of vibration, δ, according to equation 3.7.*

The same single-mode measurements and post-processing were carried out on the specimens used later (see Chapter 6) for the study of the vibration thresholds required to detect small cracks (cracked cross section less than 10% of total cross section) in thermosonics. The details of these specimens, labeled TT-1, TT-2, etc., were presented in Chapter 2 in Table 2.3. Damping measurements were taken for these specimens to confirm that small cracks had been produced, and hence the specimens were suitable for such a study, and to estimate the approximate relative

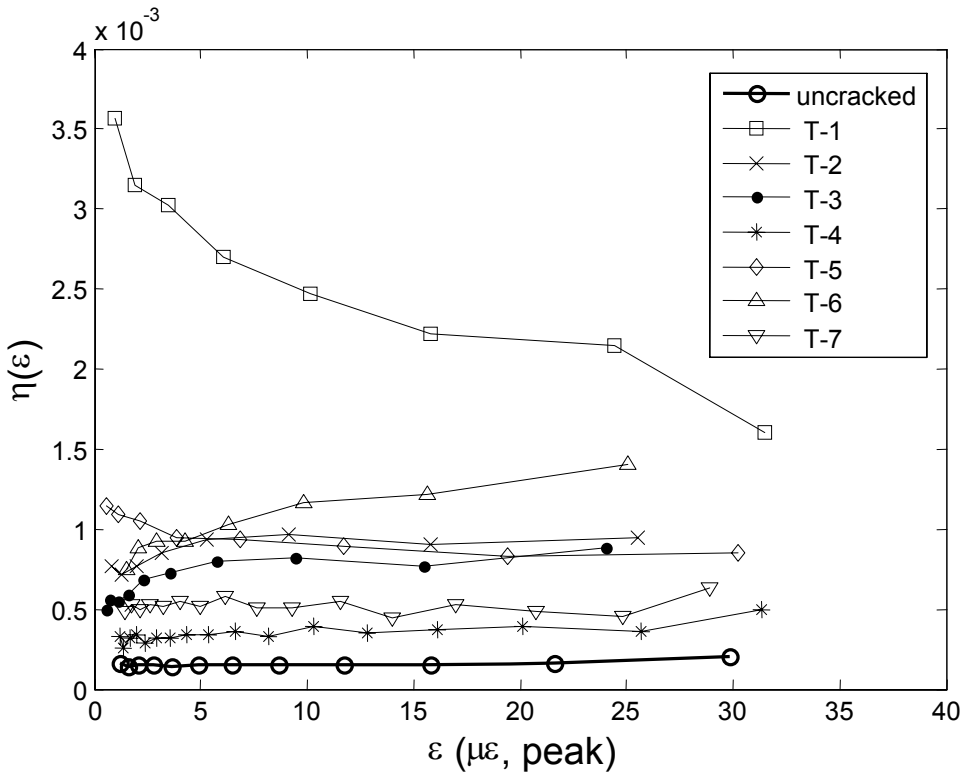

Figure 3.8: *Loss factors as a function of strain in the 3rd flexural mode for the beams T-1 to T-7 (Table 2.2) used for the prediction of the thermosonic signal.*

crack size within the batch prior to breaking the specimens. Since the specimens TT-1, TT-2, etc. are thicker (17 mm) than those from the previous batch (T-1, T-2, etc. all had a thickness of 10 mm), the 3rd flexural mode could be excited only up to around 25 $\mu\epsilon$ peak. This time, the beams did not show amplitude dependent damping. This was a first indication that the cracks could be as small as required, since for the previous batch amplitude-dependent damping was only observed for large cracks. To achieve an estimate of the crack damping as accurate as possible, 10 repeated measurements were carried out on each of the cracked specimens and on an additional uncracked one. The results of these measurements are presented in Figure 3.9 where the average η_3 is plotted vs the actual crack area given as a percentage of the total cross section (known after breaking the specimens). The average loss factor in mode 3 was calculated as the average with respect to the strain amplitude [readings available for each section of the transient of decay as in Figure 3.7 (c)] and over 10 repeated measurements. The uncertainty on the mean value

was expressed by plus and minus one standard deviation. The data show that the cracked specimens consistently exhibit a larger average damping compared to the reference uncracked specimen, although with overlapping uncertainty intervals, and the trend indicates an increasing damping with increasing crack size. The results on the cracked specimens were, thus, in line with expectations. The scatter is due to the variability of the morphologies of the cracks, including their initial partial opening. However, before breaking the specimens, the knowledge of the general level of damping of this group of cracked beams was not sufficient to establish that the crack samples definitely contained cracks of size 10% or less compared to the initial cross section. This was due to the fact that the cracks were embedded into initially thicker specimens compared to those of the previous batch (17 mm vs 10 mm). Hence, the measurement of generally lower loss factors (from Figure 3.9 it can be seen that η_3 falls in the interval $2.4-3.2\times10^{-4}$ compared to $0.3-3.5\times10^{-3}$ from Figure 3.8) could have been due to a higher value of strain energy per unit strain in mode 3 (V_3) for the thicker beams. An indication on the size of the cracks before breaking the specimens could be obtained by comparing the general level of energy loss at crack in one vibration cycle per unit strain amplitude (ΔV_3) rather than η_3. The strain energy per unit strain amplitude V_3 was calculated from a FEA analysis of these thicker beams, similar to that described in section 3.3.2 (these results will be used later in Chapter 6 and are given in Table 6.1). This was compared with the value of ΔV_3 previously obtained for the 10-mm-thick beams to conclude that cracks smaller than those produced in the former batch (hence likely to be less than 10% of cross-section) had been produced. This was later confirmed by measuring the size of the cracks after breaking the specimens.

3.4 Review of Chapter

In this Chapter, damping measurements for the beams that will be tested later using VAM and thermosonics have been presented. For the VAM specimens the damping measurements were optimized for the 1st flexural mode by reducing the support damping in this mode. Consequently, the results of such tests could be used to com-

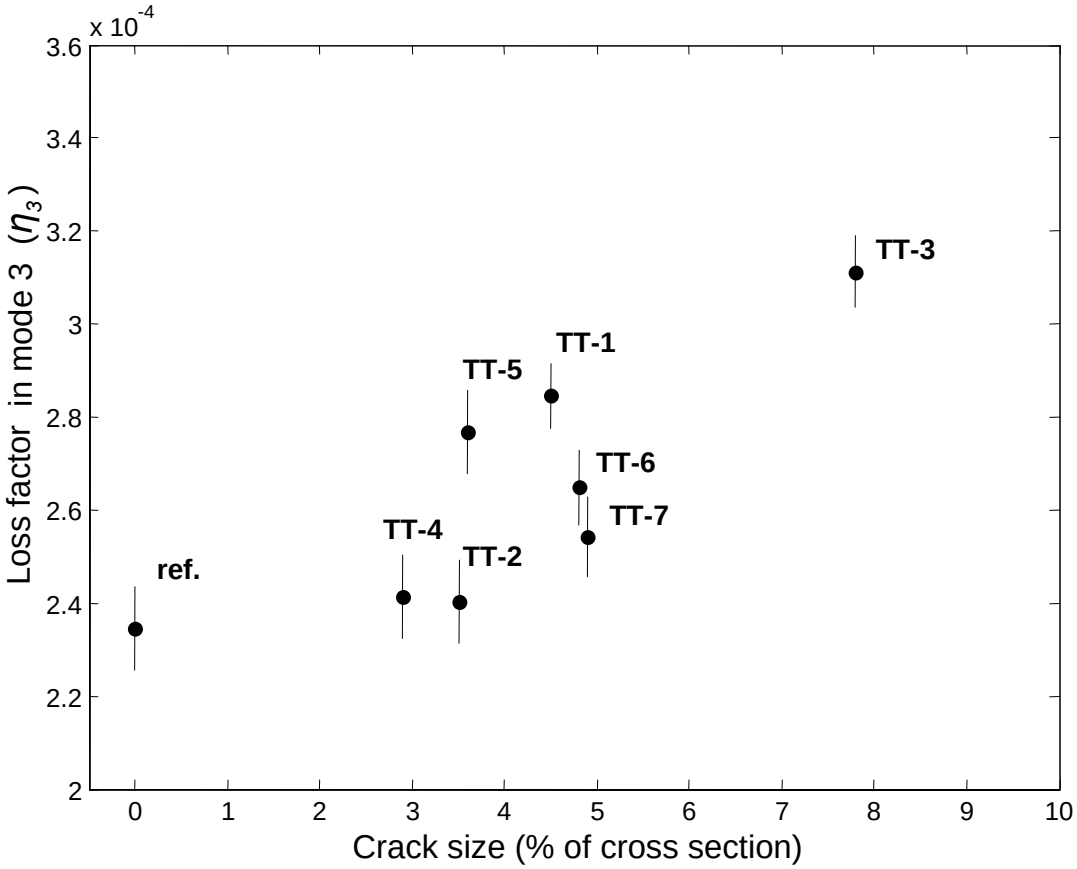

Figure 3.9: *Average loss factor in mode 3 plotted vs crack size for the specimens described in Table 2.3. The vertical error bars through each point indicate the range within plus/minus one standard deviation for 10 repeated measurements.*

pare damping measurement and VAM as NDT techniques. For the thermosonics specimens, the damping measurements were mainly used to characterize the extra crack damping at high strain and high frequency, close to those excited in the thermosonic tests. This information will be used in Chapter 5 to calculate the heat generated at the crack during the thermosonic excitation. In order to achieve the required characterization of the damping of the crack, different damping measurement methods have been applied to the beams. Each method has contributed to build an understanding of the behaviour of the crack damping at the amplitudes and frequencies of interest. It was found that the crack loss factor, η_{crack}, can be modelled as independent of vibration amplitude for small cracks (at least for cracks less than 10% of cross section). In the case of larger cracks, however, η_{crack} can

exhibit a variation for increasing amplitudes. It was also shown that, at a given amplitude, the loss factor tends to decrease for increasing mode order, with a rate of decrease which was demonstrated to be consistent with the assumption that the energy loss at the crack in one vibration cycle is independent of the mode.

Chapter 4

Vibro-acoustic modulation: an experimental study

4.1 Background

Acoustic nonlinear phenomena applied to nondestructive evaluation (NDE) have been an area of intense study since the 60s [36, 37]. The remarkable strength of many nonlinear effects introduced by defects makes their use for damage detection very attractive. Several nonlinear effects have been studied extensively for nondestructive testing (NDT) applications. It is possible, for example, to measure the wave speed dependence on the wave amplitude (acousto-elastic effect) [38] or to monitor the generation of super-harmonics [39, 40] or sub-harmonics [41] of the input signal. Another method is to detect resonance frequency shifts for increasing levels of vibration amplitude [42]. It is also possible to look at the nonlinear interaction of two or more vibration fields [43]. In all cases the evolution of the nonlinear effect can be studied over time (for example for fatigue monitoring [44]) or in space for defect location [45, 46]. Contact acoustic nonlinearities (CANs) are among the most efficient mechanisms generating nonlinear features [47]. CANs comprise all solid-to-solid interfaces with imperfect adhesion, such as cracks, disbonds, etc. Vibro-acoustic modulation (VAM) is based on this kind of nonlinearity. The phenomenon was first

reported in a US patent in 1975 [48] but the bulk of the scientific literature on the subject arose starting from the mid 90s [43, 44, 49, 50]. It can be described as follows: if an undamaged specimen is subjected to both a low frequency vibration and an ultrasound probing signal, the resultant field is simply the superposition of the fields obtained by applying the two excitations separately. However if the system is damaged (for example by a crack or some debonding), the two vibrations interact so that the ultrasound wave is modulated in amplitude and/or phase [51] by the low frequency oscillation. Therefore, the occurrence of amplitude modulation in such a setup can be taken as an indication of the presence of damage in the specimen and could be used as the basis of a nondestructive technique for damage detection. In practice, the phenomenon is usually studied in the frequency domain where the modulating effect is manifested by the presence of sidebands around the main peak at the ultrasonic frequency [52].

Using VAM, Donskoy et al. [53,54] successfully detected cracks in water pipes, measuring sidebands 30 dB higher compared to a reference measurement on a pipe without cracks. The detection was performed using one single ultrasonic frequency and the amplitude of the sidebands was shown to be proportional to the amplitude of the transmitted probing ultrasonic signal. Ekimov et al. [55] used torsional ultrasonic waves at one frequency to detect an artificially introduced interfacial defect. A thin aluminium plate with a single fatigue crack was studied by Zaitsev et al. [56]; the amplitude of the modulation sidebands was demonstrated to be dependent on the amplitudes of the high and low frequency vibrations, and on the global Q-factor of the system, the Q-factor being modified by attaching strips of insulating tape to the test structure. Several other examples of successful applications of VAM to NDT were later reported in plexiglass, sandstone and in automotive engines [57]. The sizing capabilities of the VAM testing were first experimentally studied by Donskoy et al. [58] using a set of laboratory specimens containing calibrated cracks. Here the dependence of the sensitivity of the technique on the chosen ultrasound frequency was taken into account by averaging the amplitude of the sidebands over nine measurements at nine ultrasonic frequencies between 110 and 150 kHz with 5 kHz increments. A damage index was defined by this frequency averaging, after hav-

ing normalized the amplitude of the sidebands with respect to the amplitude of both the ultrasound and low frequency vibrations. From the modelling point of view, the phenomenon was usually explained in terms of increasingly complex nonlinear models of the wave/crack interaction. The crack was typically modelled as a nonlinear spring [51, 59]. When the ultrasound frequency is fairly low, the system involves ultrasound standing wave fields [43, 53], whereas for higher ultrasound frequencies, travelling waves are a more suitable description [51, 60]. The interaction between surface waves and cracks in the presence of residual stresses around the crack was studied in detail by Kim et al. [60, 61]. The possibility to use VAM phenomena in real NDT and structural health monitoring applications has been recently confirmed by a UK patent [62], which proposes to look at the phase modulation of the probing ultrasound by means of complex signal processing using the wavelet transform. Furthermore, the possibility of using VAM in combination with conventional linear ultrasonic methods in order to obtain a classification of the defects between cavities and cracks has been also recently investigated by Kazakov [63] who detected manufactured cracks in steel plates and real cracks in large pipes.

The objective of this experimental study of vibro-acoustic modulation is to provide a systematic assessment of the potential of a particular and simple implementation of the VAM method - the one exploiting amplitude modulation of the ultrasonic standing waves in presence of low frequency structural vibrations - for NDT of metallic structures where small fatigue cracks may be present. Of particular interest is to identify quantitatively the sensitivity of this method to crack size, and how well it performs with respect to sizing. The minimum level of low frequency strain necessary for it to work also has to be determined for the method to be robust in a real inspection setting. With this objective in mind, the best choice of ultrasonic frequencies, and finally the susceptibility of the technique to noise must also be identified. A simple model of the phenomenon, used to explain qualitatively the trends in the experimental results [64], will be presented later in this Chapter to explain the main features observed experimentally.

4.2 Description and observation of phenomenon

Figure 4.1 (a) shows schematically the output spectrum of an undamaged system simultaneously subjected to a low frequency (LF) vibration at frequency f_m and continuous ultrasound (UT) at frequency f_0. In the ultrasonic region, the energy is concentrated at a single peak of amplitude F at the frequency f_0. In contrast, if a crack is present, the same peak is accompanied by two sidebands, one to the right and one to the left of the main UT frequency, of amplitudes respectively S_{+1} and S_{-1} [Figure 4.1 (b)]. Such additional frequency components are readily visible, as they appear at exactly the frequency of the probing UT (f_0) plus and minus the frequency f_m of the low frequency vibration. In the time domain, the equivalent of the appearance of sidebands in the frequency domain is a degree of amplitude modulation of the UT signal [shown in Figure 4.1 (b)]. However, it is common to analyze the ultrasonic signal in the frequency domain since the amplitude modulation in the time domain could be either extremely small compared to the overall amplitude of the signal or, at first glance, the modulation could be confused with acquisition artifacts typically arising from relatively low sampling frequencies [52]. The ratio R of the average sidebands amplitude to the amplitude of the fundamental (see Figure 4.1) can be taken as the reference quantity to be measured (crack "signature") since it expresses the strength of the modulating component of the signal due to the opening and closing of the crack under the effect of the structural vibration, and is independent of the amplitude of the received probing UT (which is a function of the frequency response function of the structure). The principal aim of this study is to find experimentally the relationship between R and:

1. the frequency of the UT probing signal;
2. the strain across the crack generated by the low frequency vibration;
3. the size of the crack.

A preliminary rig was set up with the intention to observe the phenomenon. In the initial VAM implementation, the transducers were not permanently coupled to

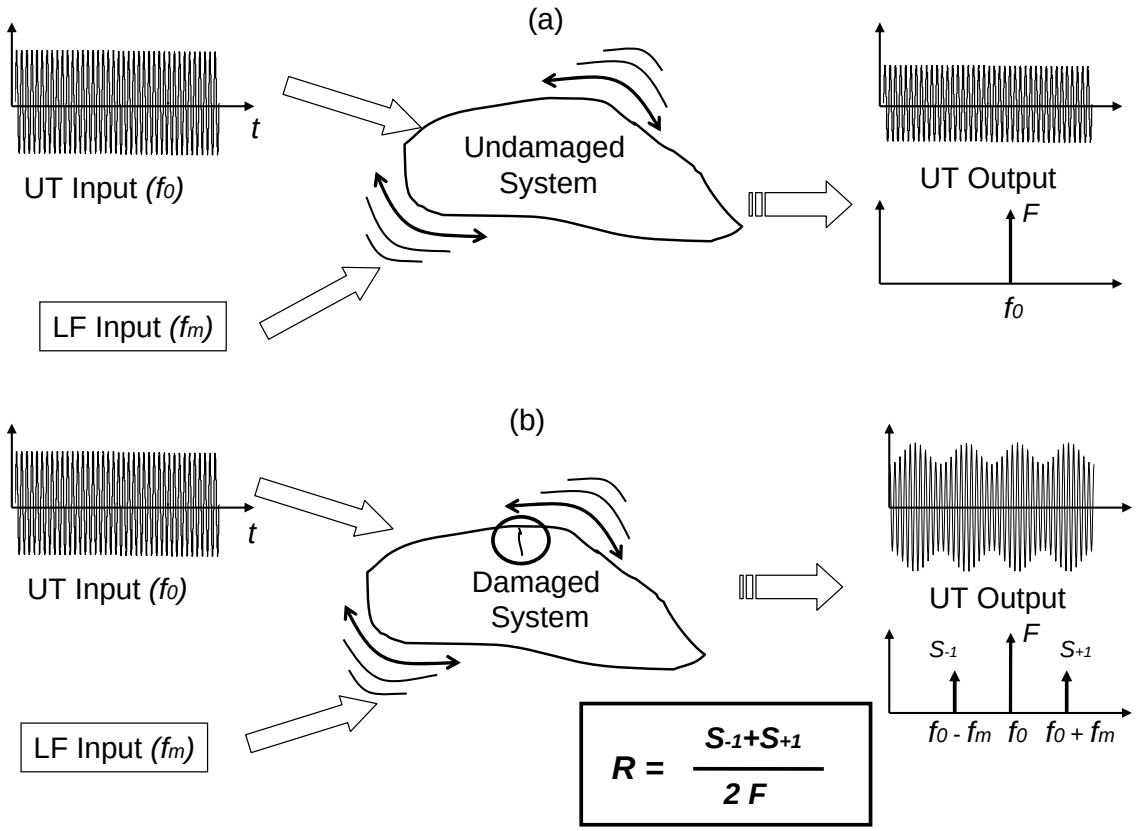

Figure 4.1: *Difference between an undamaged and a damaged system tested using vibro-acoustic modulation (VAM). (a) For an undamaged body, the spectrum of the output ultrasound (UT) does not contain sidebands. For a damaged structure, (b), the output UT presents sidebands in the frequency domain spaced at the frequency of the low frequency (LF) vibration. R is an appropriate parameter to measure the sensitivity of the method to the presence of a crack.*

the beams, but manually held against the beam ends using standard coupling gel as an impedance matching medium to transmit the ultrasound into the specimens and then receive it. Specimen L-1 (see Table 2.1 in Chapter 2) was used in these preliminary tests. The amplitude of the low frequency vibration was measured by an accelerometer. The beam was supported on foam pads. Sidebands were easily observed for this cracked specimen, as shown in Figure 4.2. The beam was excited tuning a shaker at the frequencies corresponding to the 1st, 2nd or 3rd bending mode resonance. In Figure 4.2 the 3rd bending mode of the beam was excited, which corresponds to a sideband spacing of approximately 5 kHz. It is possible to distinguish two sidebands to the left and two to the right of the fundamental

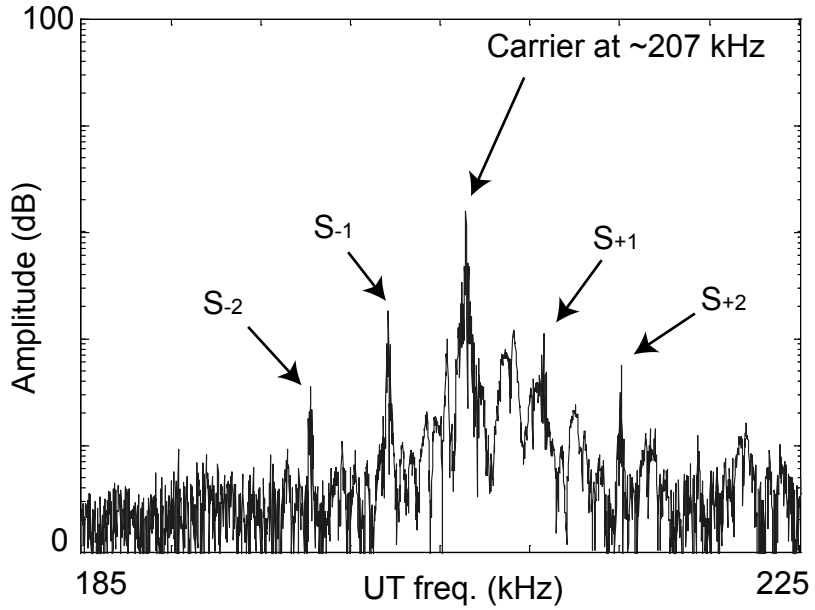

Figure 4.2: *Observation of sidebands in the cracked beam L-1 in one early VAM test.*

frequency (also called carrier frequency), labelled respectively S_{-1}, S_{-2} and S_{+1}, S_{+2}. Such prominent sidebands were hardly observed when the 2nd bending mode was excited, due to a nodal point at the middle of the beams in this mode. The second order sidebands (S_{-2} and S_{+2} in Figure 4.2) are a result of a non-perfectly sinusoidal modulating mechanism [65] at the crack and were measured to be significant only at relatively high amplitudes of the LF vibration, whereas they tended to disappear at lower LF vibrational strains and for smaller cracks. Since the first order sidebands (S_{-1} and S_{+1} in Figure 4.2), were typically the only ones measurable at lower strains, and because the purpose of this study was that of using VAM to detect small cracks, it was decided to consider only the first order sidebands in the ratio R defined above. Furthermore, it was decided to systematically excite only the 1st bending mode of the beams as the opening and closing of the crack (thought to be responsible of the generation of sidebands) is driven by the actual magnitude of the bending strain at the middle of the beams rather than by the mode shape. These initial observations encouraged a quantitative study and gave indications for the implementation of testing rigs suitable to carry out systematic experiments.

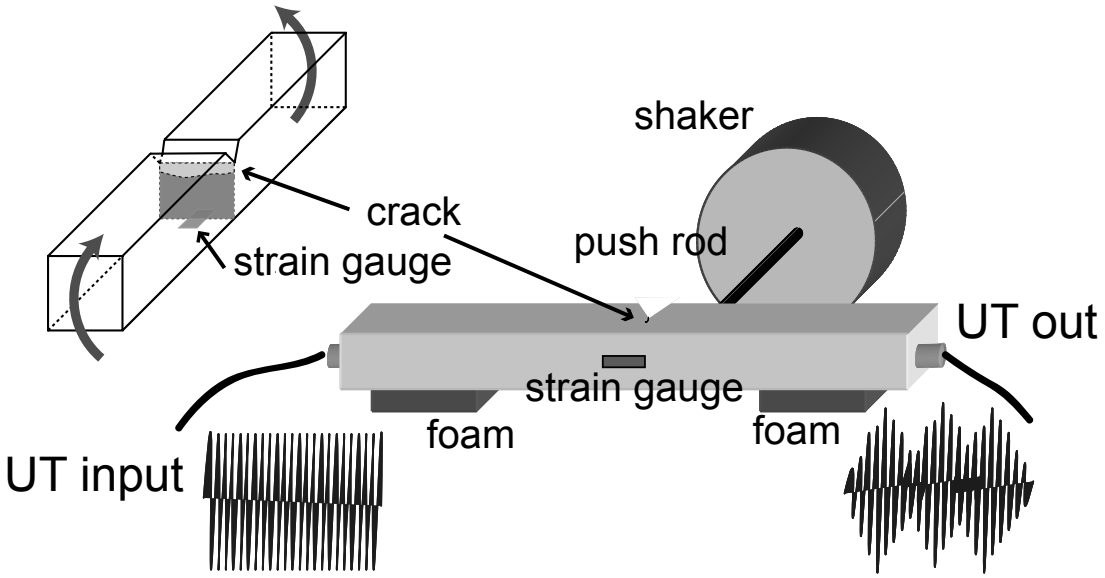

Figure 4.3: *First implementation of VAM testing for systematic measurements using a shaker to excite the 1st bending mode of the beams at resonance. The strain gauge provided a measurement of the bending of the beams and the consequent opening/closing of the crack, as illustrated on the top left.*

4.3 Systematic experiments: forced excitation

Two practical implementations of the VAM technique were investigated in this study. In the first setup, similar to the one used for the preliminary tests and shown schematically in Figure 4.3, the cracked beams were supported horizontally on two foam pads and instrumented with two permanently bonded PZT discs (so that the coupling conditions between the transducers and the beams were reproducible) of diameter 10 mm and thickness 4 mm for the transmission and measurement of the ultrasound typically in the range 50 - 230 kHz. The input PZT disc was driven by an amplified tone burst of 30 thousands cycles while the ultrasound and low frequency strain, measured respectively by the receiver PZT disc and the strain gauge, were simultaneously logged using a storage oscilloscope. The data were stored and processed later using standard fast Fourier transform (FFT) tools. An electromagnetic shaker (Data Physics model S-004) was attached to the beams in the proximity of the notch and in the direction perpendicular to its length; the connection was realized by first bonding an aluminum stud with a threaded hole to the beams and

connecting this to the shaker via a push rod. The frequency of the force applied to the beams was tuned to the resonance of the 1st bending mode of the beams at approximately 1 kHz (only beams L-1 and L-2 of Table 2.1 of Chapter 2 and one 300-mm-long uncracked beam were used at this stage) so as to maximize the amplitude of the vibration and thus the "breathing" of the crack. The amplitude of the low frequency vibration was varied by changing the output of the shaker amplifier (Data Physics model A-060). The resulting opening and closing of the crack was indirectly measured by the back-face strain gauge of Figure 4.3. With this setup, it was possible to automate the frequency sweep of the ultrasound over broad frequency ranges, while the low vibration was kept at a constant amplitude. This procedure was then repeated for increasing levels of the amplitude of the low frequency vibration up to a maximum of 80 $\mu\epsilon$ (peak value) measured at the strain gauge. The results of this procedure are shown in Figure 4.4 for the cracked beam L-1. While the amplitude of the carrier is virtually independent of the low frequency strain (group of nearly perfectly overlapping curves at the top of Figure 4.4), the ratio R is a function of the bending strain (curves at the bottom of Figure 4.4), which confirms the dependence between the ultrasonic sidebands amplitude and the amplitude of the low frequency structural vibration. The same experiment was repeated using one uncracked specimen in order to: a) verify that the amplitude modulation of the ultrasound, and hence the sidebands, were only caused by the crack and b) establish appropriate criteria for the comparison between damaged and undamaged specimens.

Typical results from this comparison are shown in Figure 4.5 where data from both a cracked (L-1) and an uncracked specimens are plotted for the same level of strain (40 $\mu\epsilon$ peak value measured at the middle cross section). Here the sidebands-to-carrier ratio is plotted against the ultrasonic frequency. As it can be seen from Figure 4.5, no clear indication of damage could be obtained, either by using the maximum ratio criterion as an indicator of crack presence or from the value of the average ratio over the whole frequency range. In the former case a difference of just 2 dB was measured, and only a slight improvement (4 dB) was obtained in the latter. It is believed that the poor reliability obtained with this rig is due to the contact nonlinearities between the shaker attachment and the beam, as well as the

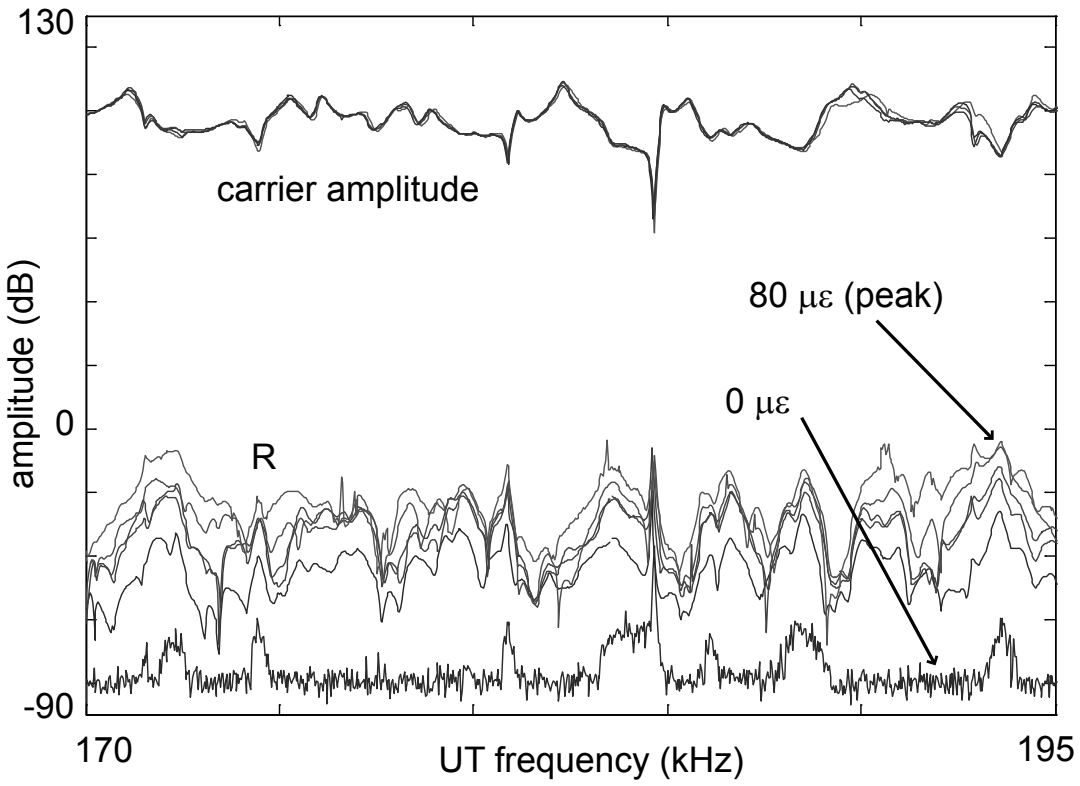

Figure 4.4: *Typical results obtained using the shaker rig of Figure 4.3 to test the cracked beam L-1 at different low frequency strain levels. Group of curves at the top: carrier amplitude (which represents the response of the structure to excitation over a range of frequencies). Group of curves at the bottom: sidebands-to-carrier ratio (R). The "zero-strain" curve corresponds to the shaker switched off (spurious peaks are created on this curve by minima in the response curve).*

beam and its supports, causing an amplitude modulation of the ultrasound which resembled that generated by the crack (the nature of this interaction would require further investigation). Various rubber washers or pads were inserted between the beam and the shaker attachment in an attempt to reduce this contact nonlinearity but this proved unsuccessful as the strain excited in the beams was then reduced drastically.

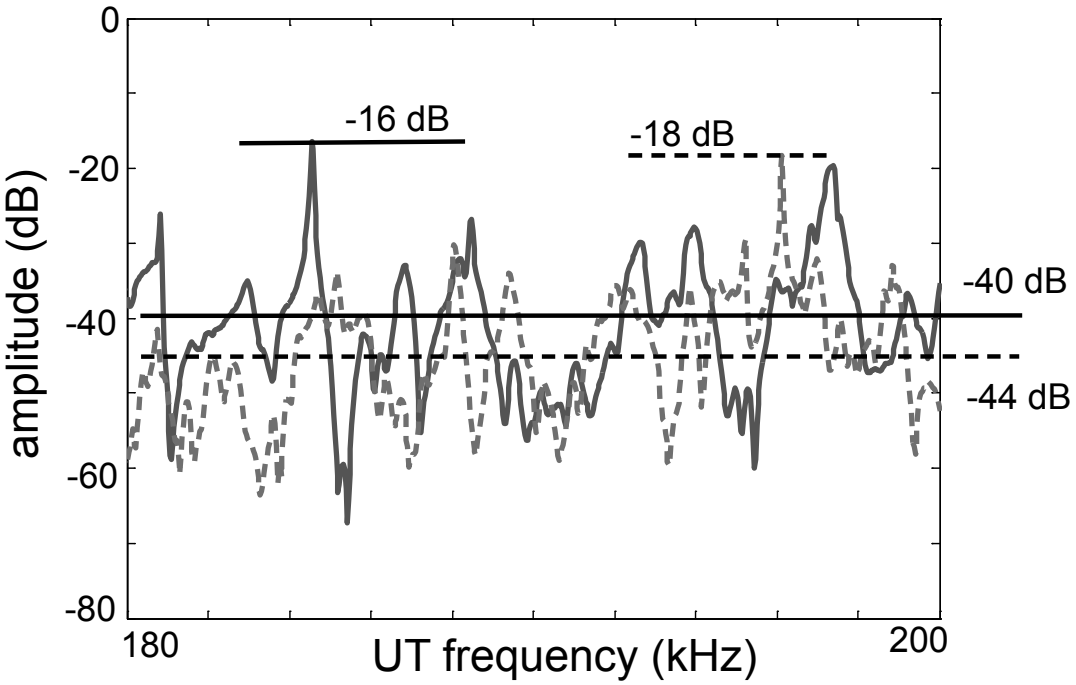

Figure 4.5: *Comparison between the levels of R in the ultrasonic frequency range 180 - 200 kHz at the same low frequency vibration amplitude (40 $\mu\epsilon$) for one cracked (solid line, beam L-1) and one uncracked (dashed line) specimen. The absolute maximum of R is only 2 dB higher for the damaged beam whereas the average level of R over the entire frequency range is only 4 dB higher.*

4.4 Systematic experiments: impact excitation

A suspension rig was set up to overcome the reliability problems of the shaker rig, and is shown schematically in Figure 4.6. The suspension was realized by bonding two rubber studs at the nodal position of the 1st bending mode of the beam and then by passing two elastic strings through them. The beam was instrumented with two PZT discs and with a strain gauge of the same kind described earlier. The excitation of low frequency modes was performed by hitting the beam at about mid-span using an automatic tapping device. This device was essentially formed by a ferromagnetic cylinder arranged inside a solenoid which was connected to a timed supply electrical circuit. Following the discharge of a capacitor internal to this circuit, the current passing through the solenoid induced a force on the cylinder which could freely

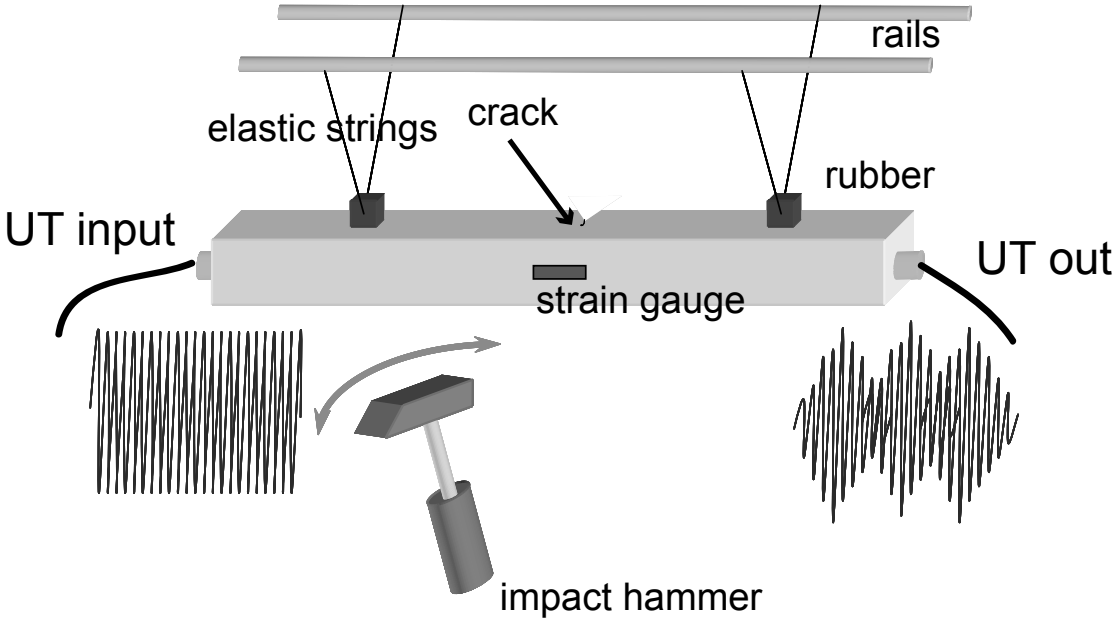

Figure 4.6: *Schematic of the impact-hammer suspension (IHS) rig.*

move in the horizontal direction thus impacting the test-structure. The tip of this cylinder/hammer was made of a soft nylon material so that the dominant mode excited was the 1st bending mode. Having automated the tapping, it was possible to automate the measurement routine. After every hit the ultrasonic frequency was incremented by 30 Hz and the measurements repeated. In this way the ultrasonic frequency could be swept automatically over a large frequency range (50 - 230 kHz). Another major advantage of this rig was that the amplitude of the sidebands for decreasing levels of the strain could be analyzed along the transient of decay of the 1st bending mode following every impact. An example of the strain excited in one of the beams after an impact is presented in Figure 4.7 (a). From the spectrum of this signal, Figure 4.7 (b), it can be seen that the dominant mode excited is the 1st bending mode although there is a little contamination from higher frequency odd flexural modes (3rd and 5th). The ultrasound was excited, at one selected frequency, during the whole duration of the vibration decay. The average amplitude of the sidebands was measured in each of the segments of Figure 4.7 (a).

A global view of the results obtained following this procedure is given in Figure 4.8. The carrier amplitude and the ratio R are plotted as a function of the ultrasonic

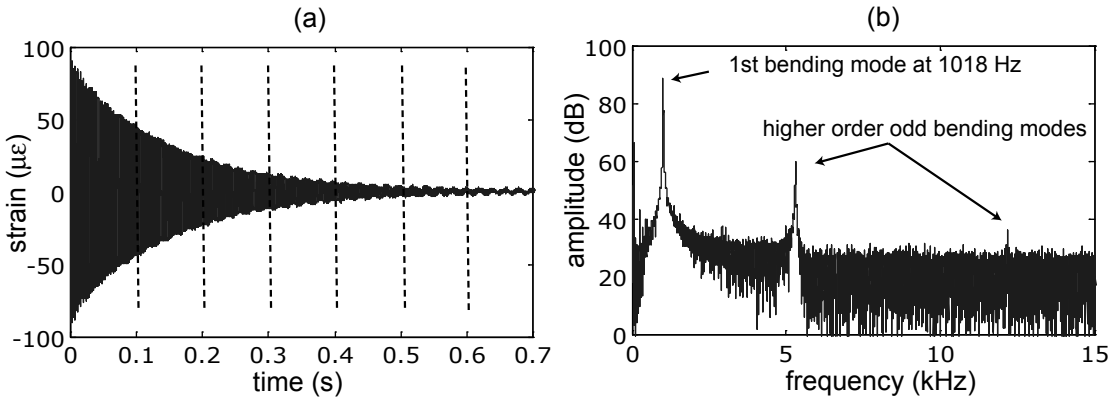

Figure 4.7: *Example of transient vibration excited by an impact, as measured by the strain gauge. (a) Record of strain vs time and segments used in the analysis of the sidebands amplitude as a function of strain. (b) FFT of the strain signal.*

frequency and low frequency strain. In Figure 4.8 (a) an uncracked beam is tested over the UT frequency range 100 - 220 kHz. One curve is plotted for the carrier amplitude and one for the amplitude of the ratio R for each of the segments shown in Figure 4.7. Virtually no strain dependence is measured for the carrier curves, and practically negligible strain dependence is shown by R: this proves that the ultrasound has been efficiently decoupled from the supports/attachments compared to the shaker rig. In Figure 4.8 (b) beam L-2 is tested over the UT range 70 - 230 kHz and the results plotted in the same way as Figure 4.8 (a). Although the carrier amplitude is still independent of the low frequency vibration, the ratio curves show a clear dependence on the bending strain especially from around 130 kHz onwards.

For a more detailed analysis, a further comparison between the cracked (L-2) and uncracked specimen of Figure 4.8 is shown in Figure 4.9 within a restricted frequency range. The ratio of the average of the amplitudes of the first sidebands over the carrier is clearly strain dependent only in the presence of a crack, and produces a "waterfall" graph for decreasing strain. For the uncracked specimen, the ratio curves (obtained with the same postprocessing routines) tend to a common level at about -65 dB, with two peaks at about -50 dB at the antiresonances of the ultrasonic carrier. This might be due to the small amplitude of the carrier signal at its antiresonances, causing errors in the ratio value. However, if a crack was not present, the high and low frequency vibration fields did not interact significantly and hence the

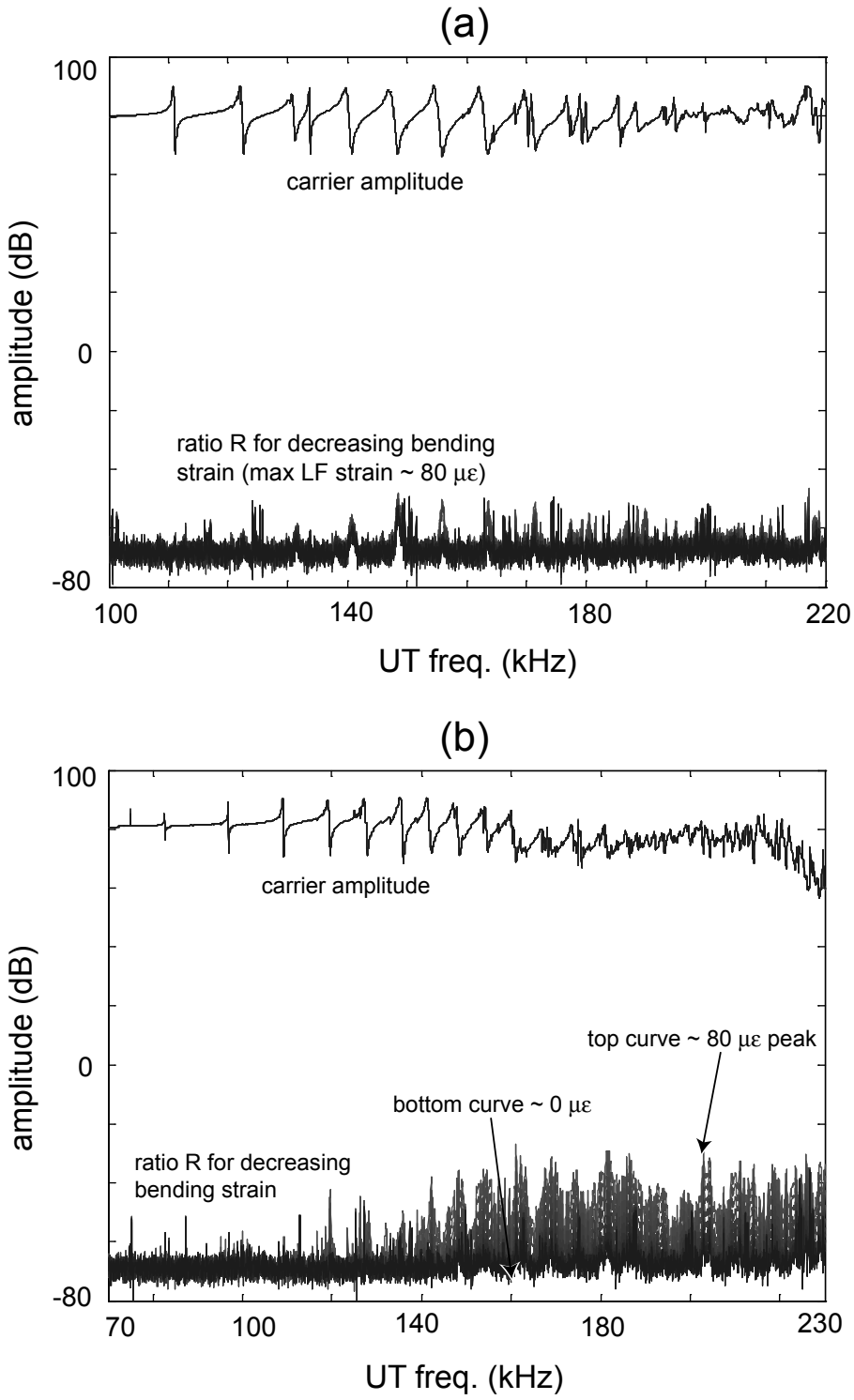

Figure 4.8: *Comparison between the results obtained testing one undamaged and one cracked beam using the IHS rig. (a) Amplitude of carrier and ratio R as a function of UT frequency and LF strain over the range 100 - 220 kHz for an uncracked beam. (b) Amplitude of carrier and ratio R as a function of UT frequency and LF strain over the range 70 - 230 kHz for the cracked beam L-2.*

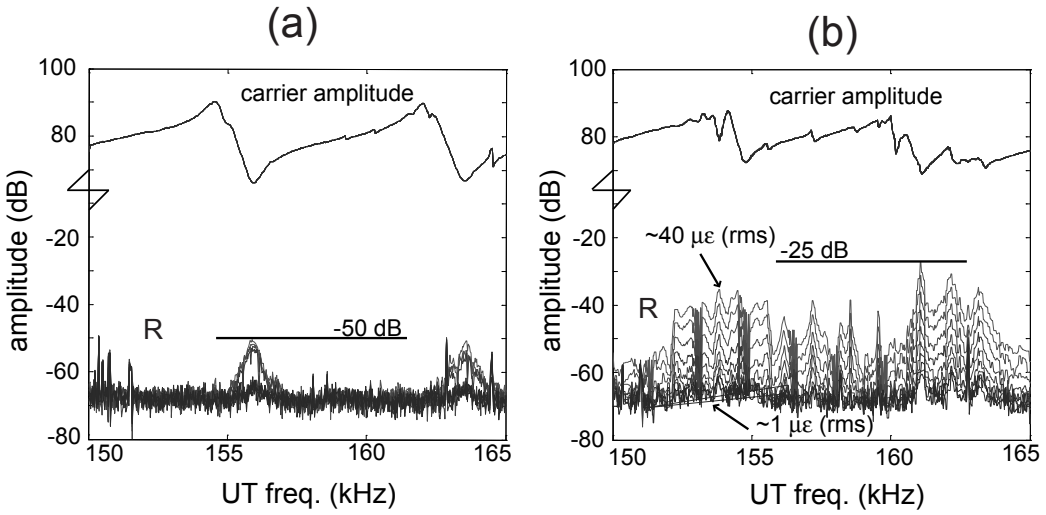

Figure 4.9: *Zoom between 150 and 165 kHz of the results presented in Figure 4.8. (a) Uncracked beam; (b), cracked beam.*

impact-hammer suspension (IHS) rig was judged suitable for further testing. These results also confirmed that the shaker attachment and the supports did produce the nonlinearity seen in the shaker rig experiments on uncracked beams. Using the IHS rig, in the case of the cracked specimen L-2, the maximum ratio was about -25 dB at around 80 $\mu\epsilon$ rms, allowing a good dynamic range for performing the crack detection by comparing the maximum values of the ratio across a chosen frequency range. However this dynamic range could be further improved by considering the average ratio over the whole frequency range. It is also interesting that local maxima of sensitivity seem to be present every approximately 3 to 5 kHz, starting at about 100 kHz. This suggests that a frequency sweep over about 5 kHz would be sufficient to ensure a high sensitivity point.

4.4.1 Analysis of sensitivity to crack size

The experiments were repeated for all the seven cracked beams available. For each beam the value of the average ratio (i.e. the average sensitivity) $\overline{R}$ across the whole UT frequency range swept from 70 to 220 kHz was plotted as a function of the average strain level, s, of the low frequency vibration. Then the strain range within

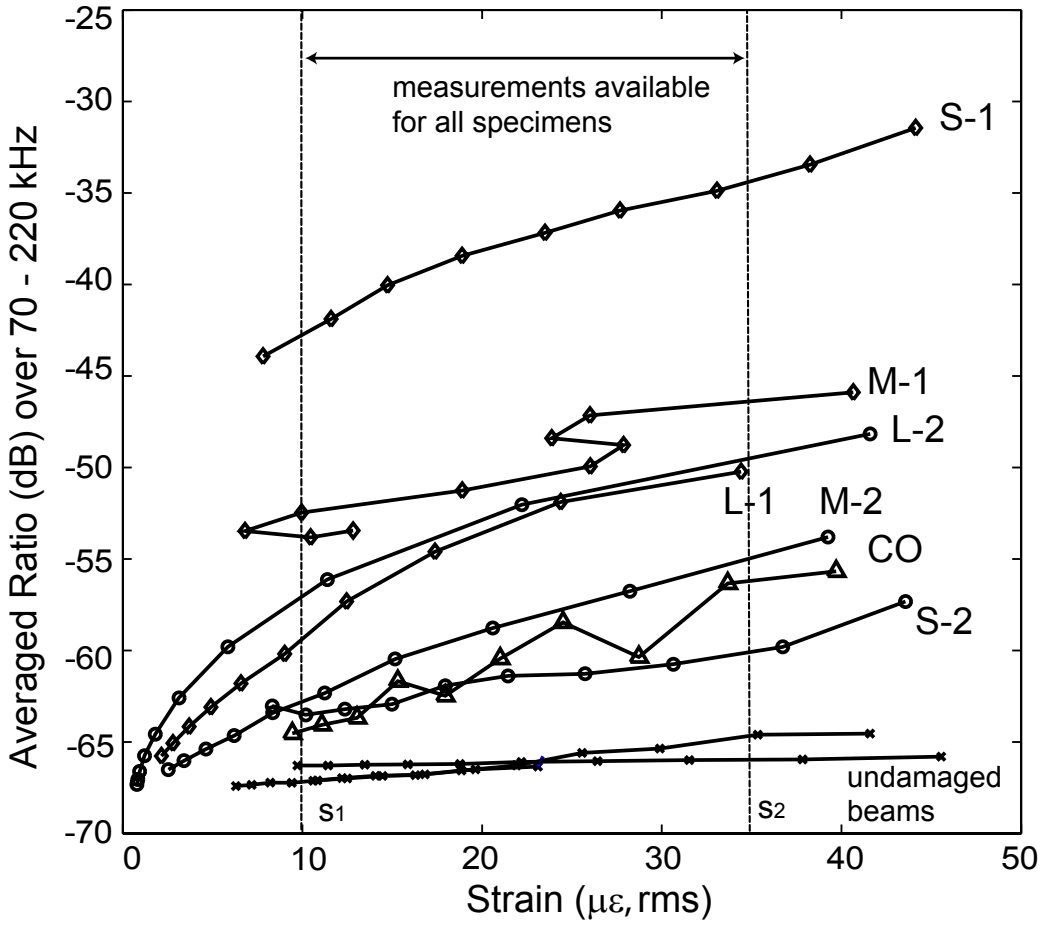

Figure 4.10: *Summary of the results of the VAM tests using the IHS setup for the cracked beams of Table 2.1 (Chapter 2) and for three other uncracked beams. The average of the sidebands-to-carrier ratio over a broad frequency range (70 - 220 kHz) is plotted vs the LF strain. The irregular behaviour of specimen M-1, with respect to the LF vibration, is due to beating of the 1st flexural mode about the two principal axes. This was absent for all the other beams.*

which experimental points were available for all the specimens was considered, from s_1 to s_2 (see Figure 4.10). A damage index (DI) was derived from the area of the graph delimited by the sensitivity versus strain plot (on a linear scale) for each damaged specimen, and that under the ratio versus strain curves for the undamaged specimens of the same size,

$$DI = \frac{\int_{s_1}^{s_2} \overline{R_{cracked}}(s)ds}{\int_{s_1}^{s_2} \overline{R_{uncracked}}(s)ds}. \tag{4.1}$$

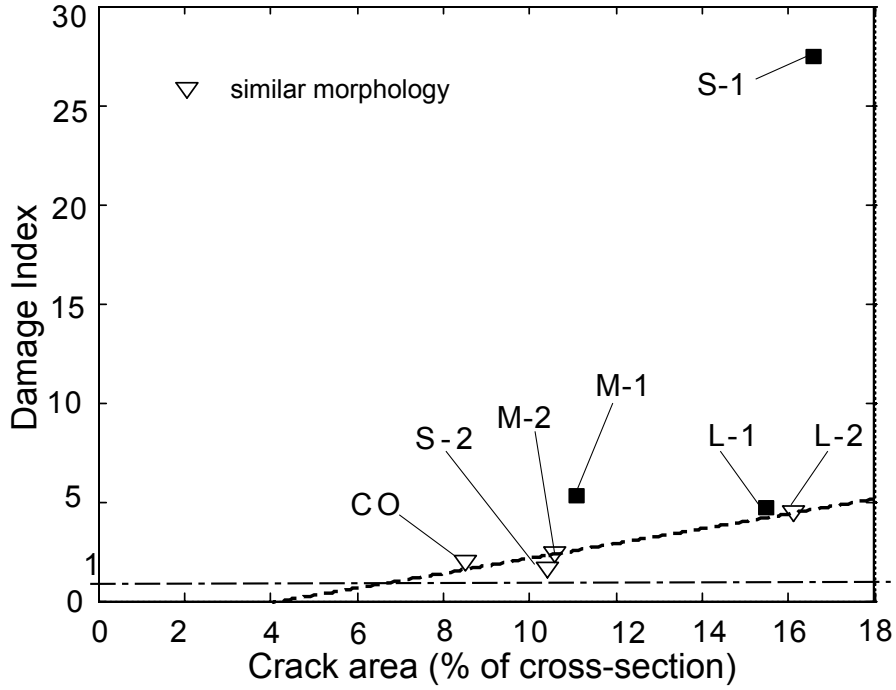

Figure 4.11: *VAM damage index (see equation 4.1) plotted against the crack area. The dash-dot line represents the reference value of 1 for undamaged specimens. The dashed line is the best linear fit considering cracks likely to have similar morphology (CO, S-2, M-2 and L-2).*

The damage index defined in equation 4.1 takes into account the dependence of the sensitivity of the VAM technique on the ultrasonic frequency and on the level of the low frequency strain reached during the tests. It also takes into account the nonlinearities that may be introduced by the supports and attachments by dividing the integral for the damaged specimen by the same quantity for undamaged specimens. The DI will therefore be a value greater than 1 for cracked specimens. If the same specimens were tested using different implementations of the VAM test (e.g. the shaker rig), reaching similar levels of the low frequency vibration and sweeping the ultrasound across the same frequency range, the DI as defined in equation 4.1 would also quantify the reliability of the different implementations. Figure 4.11 shows the damage index plotted against the percentage of actual cross section covered by the crack (see Table 2.1, Chapter 2). The damage index appears to increase with the severity of the damage but there is considerable scatter in the normalized exper-

imental data. For specimens L-2, M-2, S-2, and CO, it is likely that the initial opening of the corresponding cracks is similar (as discussed in section 2.4.1). A trend-line was fitted to the experimental data for these specimens. This allows the smallest detectable crack using the IHS rig to be estimated by the intersection of this trend-line with the horizontal line at $DI = 1$, representing the noise floor of the testing rig. From this it appears that a cracked area of 7% is the smallest that can be expected to be detected by this implementation of the technique. Specimen S-1 shows a much higher damage index compared to specimens L-1 and L-2 even though the crack is of very similar dimensions. This could be due to a different initial degree of closure of the crack that could result in an "effective" percentage crack size bigger than that of specimens L-1 and L-2. The meaning of the "effective" crack area and its estimation in VAM testing will be discussed later in section 4.6.

4.5 Overview of modelling work

As part of this vibro-acoustic modulation project, simple models were proposed to explain the trends observed experimentally that have been described earlier in this Chapter. Although this part of the work was conducted under the responsibility of Dr. Duffour [64], a description of his models is offered in this section for the completeness and clarity of the Chapter. The results of the modelling work will be used in the next section to discuss some experimental findings.

The geometry of the beam modelled was that of the long beams used in the experimental study (L-1 and L-2). Their 1st bending mode frequency was around 1 kHz while the ultrasound frequency used was up to 200 kHz. Therefore, at this frequency, for every cycle of the low frequency vibration, 200 ultrasonic cycles are transmitted. It will be assumed throughout the modelling section that in these conditions, the ultrasonic (UT) vibration is in steady state within each half bending cycle. To verify this assumption, the UT Q-factors were measured experimentally on some of the specimens. Q-values up to 130 kHz were measured by the half-power bandwidth method from the carrier amplitude vs frequency curves, an example of

which was shown in Figure 4.8. The measured Q-factors were mostly around 200. Given this damping value, a vibration at 200 kHz reaches approximately 80% of its steady-state value during each half of the bending period so the assumption is not entirely valid but comes close to being met. Results will be presented for different values of Q; it will be appreciated that the prediction will be inaccurate at Q above about 200. However, the general trends of the modulation at different frequencies and strains could still be obtained.

Duffour's approach is based on the principle that, in these conditions, an adequate way of describing the relationship between the ultrasonic input and output is to introduce the transfer function between the two points where the sensors are located. Transfer function measurements [19] alone have been used for crack detection for some time and several papers model the effect of cracks on transfer functions [66,67], but the resonance frequency shifts introduced by cracks often proved not to be sensitive enough for many practical applications. By contrast, in a VAM setup, two types of vibration interact. As the beam bends according to its 1st mode shape, the degree of opening and closing of the crack changes so that the transmission characteristics of the cracked cross section change. The transfer function then gradually shifts from the state when the crack is most open to the state where it is most closed. This is illustrated diagrammatically in Figure 4.12 (a). In the model used by Duffour, the geometrical deformation of the crack affects the ultrasound field globally by slightly shifting the beam resonances over the course of a bending cycle as shown by Figures 4.12 (b) and (c). When the crack is closed, the structure can be regarded as a structure without defects; conversely, when the crack is open one can think of a structure with a very small notch.

The same underlying idea was used by Kim et al. [60,61]. In both their model and this one, the presence of sidebands is accounted for by the parametric geometrical deformation of the crack induced by the low frequency vibration. However the operational conditions of the system they investigated were quite different. In the case of Kim et al., this geometrical deformation was probed locally using a surface acoustic wave at a frequency of around 1 MHz in a pulse-echo configuration. In the

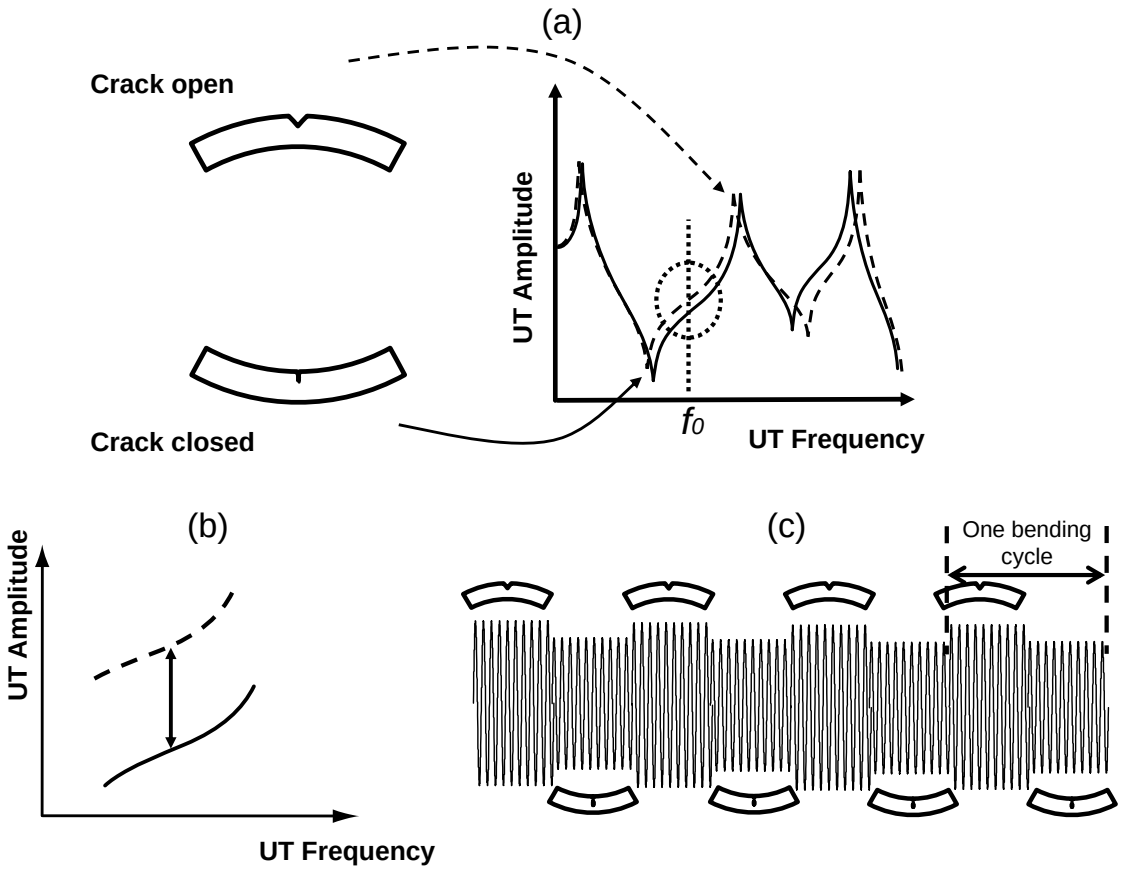

Figure 4.12: *(a) Scheme showing the shifting of the beam transfer function due to the opening and closing of the crack at low frequency (note that the carrier/response curves seen in Figures 4.4, 4.8 and 4.9 correspond to an average of the transfer functions shown here for the cases of crack open and crack closed). (b) Zoom around the ultrasonic frequency f_0. (c) Diagram showing the modulating effect in the idealized case that the cracked region is free of compressive residual stresses.*

model described here, the geometrical deformation of the crack affects the 200 kHz ultrasound field globally by slightly shifting the beam resonances over the course of a bending cycle.

A pure sine wave at frequency f_0 and modulated in amplitude in the time domain results in the appearance of smaller peaks on either side of the main peak centered on f_0 in the frequency domain. As in the experiments, the term "carrier" will refer to the pure sine wave, i.e. ultrasound, and the first smaller peaks on both sides of the carrier are called "sidebands". It is assumed here that a closed crack is

transparent to the ultrasound. Therefore the transfer functions in the closed state were calculated for beams without a crack. This amounts to neglecting the wave scattering properties of closed cracks [68]. However, at 200 kHz, the wavelength in steel is sufficiently large for this simplification to be justified. The transfer function in the open state was obtained by considering the crack fully open for various crack depths.

This type of modeling bears strong similarities to an earlier study by Richardson [69] who investigated the propagation of a wave through a planar interface with no tensile strength. However, in his one-dimensional model, the two sides of the clapping interface could only move parallel to each other so that the contact could either be complete or nonexistent. Here, the low frequency bending stress influences the ultrasound by cyclically changing the area of contact between the crack faces. This is different from some of the work on vibro-modulation cited in section 4.1 where the crack is usually modelled as a material nonlinearity having an elastic stiffness comprising a constant (linear) component plus a quadratic corrective term which varies with the low frequency stress.

It is also assumed here that the ultrasonic vibration, because of its higher frequency and much lower amplitude compared to the bending vibration, does not affect the opening and closing of the crack. For an ultrasound excitation at a given frequency f_0, the value of the transfer function at f_0 will then oscillate between two extreme values as the crack opens and closes (see Figure 4.12). Exactly how the ultrasound frequency changes from one extreme value to the other depends on the particular characteristics of the crack. In particular, the presence of residual stresses in the cracked region is likely to affect the degree of opening and closing of the crack induced by bending. Pursuing the analysis further requires making simplifying assumptions. First the case of a crack free of residual stresses is investigated. Then a simple model will be used to study how compressive stresses in the beam and initial crack opening interact with the cyclic crack closure caused by bending.

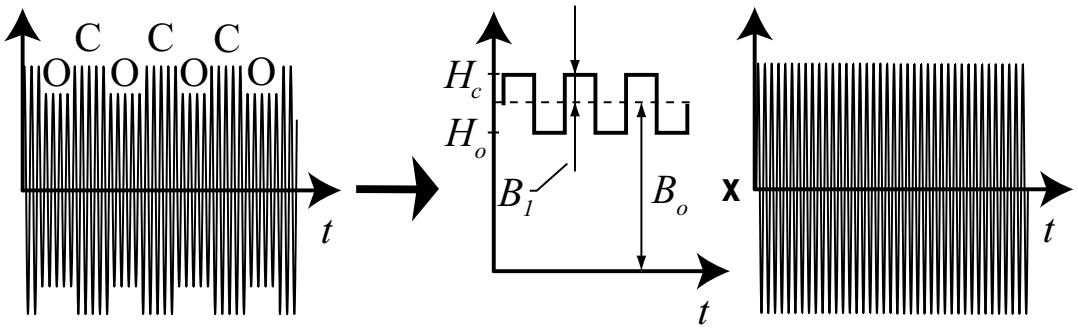

Figure 4.13: *Diagram detailing the modulating effect when the cracked region is free of compressive residual stresses. The modulated signal can be decomposed into a pure high-frequency sine wave multiplied by a square modulating function.* B_0 *is the mean value of the modulating signal.* B_1 *is the peak amplitude variation around this mean.* $H_{o/c}$ *are the amplitudes of the transfer function at a given ultrasonic frequency when the crack is respectively open/closed.*

4.5.1 Case with no residual stresses

Imagine that when the beam is at rest, the crack faces are two mating surfaces in "grazing contact" with no residual compressive stresses. Then the crack immediately and fully opens (closes) as soon as the bending stresses in the top half of beam become tensile (compressive), assuming the crack is in the top half of the beam. In this idealized situation, the magnitude of the bending strain has no influence on the crack closure. For half the bending cycle the ultrasound settles in a system with a completely open crack whereas during the other half of the cycle, the crack is closed. The measured ultrasonic output will then be a high frequency sine wave modulated in amplitude by a low frequency square wave as illustrated in Figure 4.13. This modulated signal can be viewed as a pure sinusoidal oscillation multiplied in the time domain by a square signal (modulating wave). This simple multiplication becomes a convolution of the corresponding spectra in the frequency domain [70]. At a given ultrasonic frequency f_0, the modulating square signal oscillates between the values of the two transfer function values $H_0(f_0)$ (open) and $H_c(f_0)$ (closed).

This modulation function must have a nonzero dc value to account for the fact that ultrasound is transmitted even when the crack is fully open. This dc value is simply the mean of H_o and H_c, which can be written, using the notation of Figure 4.13, as

$$B_0 = \frac{H_o + H_c}{2}. \tag{4.2}$$

Around the mean, the amplitude of the square oscillation is

$$B_1 = \frac{H_c - H_o}{2}. \tag{4.3}$$

If there is no crack, there is no difference between H_o and H_c and the amplitude of the sidebands is zero. If the crack is large, one can expect the shift between $H_o(f_0)$ and $H_c(f_0)$ also to be large at most ultrasonic frequencies f_0; consequently the value of the ratio R is also large. R can be calculated as a function of the modulating wave coefficients in the time domain, B_1 and B_o [70],

$$R = \frac{2}{\pi}\frac{B_1}{B_0}, \tag{4.4}$$

and will therefore only depend on the values of the transfer functions in the open and closed states. An alternative expression for R can be given by using the dc and first Fourier coefficients, labelled respectively c_0 and c_1, of the Fourier transform of the modulating wave in the frequency domain [70]:

$$R = \frac{c_1}{c_0}. \tag{4.5}$$

In both cases, to obtain quantitative predictions for the ratio R, it is therefore necessary to have plausible values for the two transfer functions $H_{o/c}(f)$, calculated for the beams considered in this study. The method used for this purpose was a finite-element (FE) model of the beam.

Simulation using a finite-element model

The beam was modelled as a three-dimensional solid using the FE package ABAQUS. The model was as close as possible to specimens L-1 and L-2 used in the experiments. The crack was modelled by unconstraining the nodes along the root of the notch

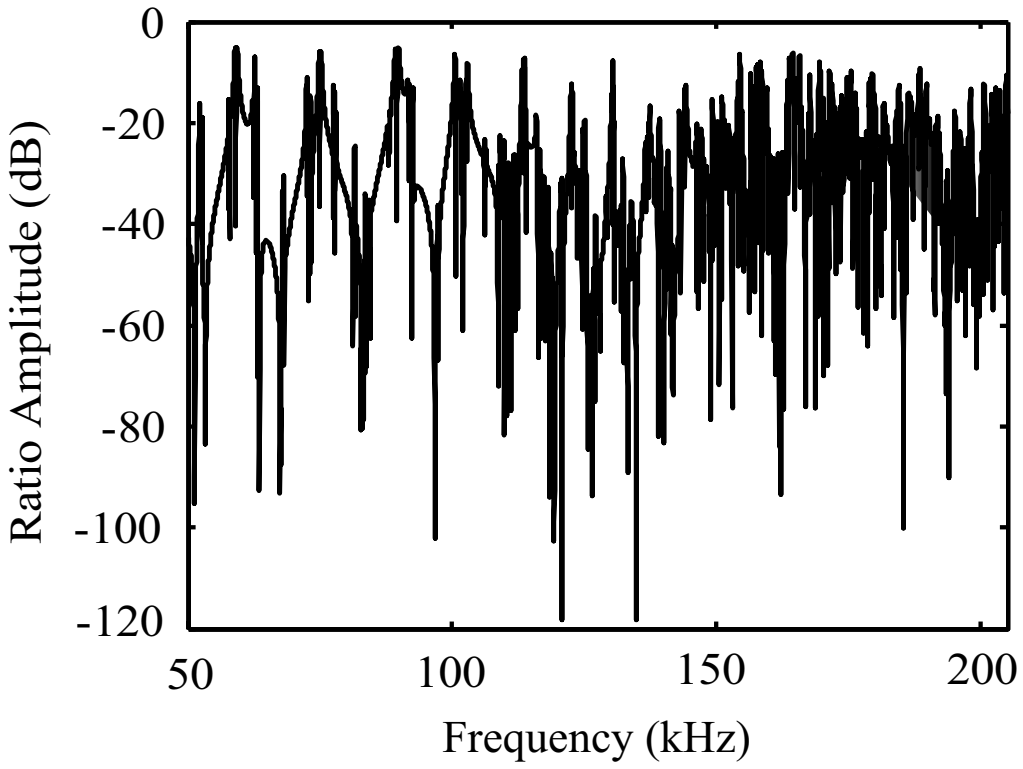

Figure 4.14: *Amplitude of the sidebands-to-carrier ratio (R) plotted versus the UT fundamental frequency obtained from finite-element computations with 10% crack depth and Q=1000.*

over 2 mm further down. The modes of the beam were computed using free-free boundary conditions. The transfer functions were computed using the standard analytical formula [34]

$$H_{ij}(\omega) = \sum_n \frac{u_i^n u_j^n}{\omega_n^2 + i\omega_n\omega/Q_n - \omega^2}, \tag{4.6}$$

where H_{ij} denotes the value of the transfer function at the angular frequency ω between points i and j. u_i^n is the mode shape value at location i for mode n, ω_n and Q_n are the natural frequency and the Q-factor for mode n. The Q-factor values could be varied from one simulation to another but for a given simulation all modes were assigned the same Q. The force input was applied at one end of the beam, along its axis, and the output was taken on the other end (at the location of the PZT discs in the experimental setup, however the discs were not actually modelled). A typical computational result is shown in Figure 4.14 where all modes were assigned a Q of

1000.

The ratio of the first sidebands amplitude over the carrier amplitude was calculated using equation 4.4 and plotted against the carrier frequency from 50 to 210 kHz. It is immediately apparent that the modal density is large. Even with a purely axial excitation, bending and other non-longitudinal modes will be excited due to the asymmetry introduced by the notch. Resonances become even denser above 100 kHz, which is around the frequency of the first cross-section resonance of the beam (i.e. the cut-off frequency of the first higher order mode). This plot provides a realistic frequency dependence of the value of the ratio with the ultrasonic probing frequency. It shows that the ratio peaks at around -7 dB throughout the frequency range. Figure 4.14 also shows that for high modal densities, it becomes extremely difficult to correlate peaks in the ratio curve with individual resonances in the open/close transfer functions. At high frequencies, the identification of resonances itself is problematic because of the strong coupling between closely spaced modes. This feature was also observed experimentally, for example in Figure 4.8.

Similar FE computations were carried out for varying equivalent defect sizes (from 1% to 10% cross-section area reduction) and Q-factors ranging from 100 to 1000. The result is shown in Figure 4.15. The quantity plotted along the vertical axis is the averaged ratio over the whole frequency range (50 - 210 kHz). It is clear that the damping in the system has a significant effect on the sensitivity. The average ratio reaches about -25 dB for a 10% cracked area and Q=1000. The sensitivity drops to about -40 dB for the same Q and a 1% crack depth and further drops to -50 dB for a 1% crack depth and Q=100. Recalling that the experimental "noise floor" given by the damaged index of undamaged specimens was around -65 dB, these simulation results suggest that it should be theoretically possible to detect cracks smaller than 1%. However in this simple model the strain dependence of the vibro-modulation effect cannot be explained and this theoretical sensitivity performance must be reviewed when the effect of residual stresses or initial crack opening are taken into account.

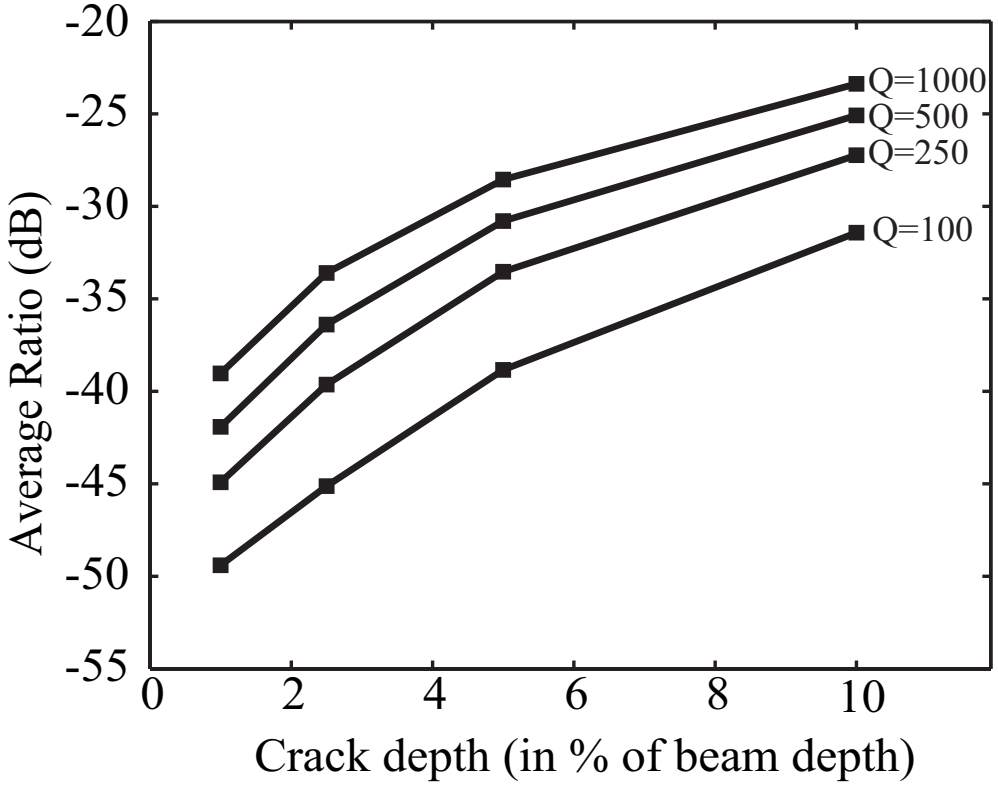

Figure 4.15: *Plot showing the amplitude of R (average over the ultrasonic frequency range 50 - 200 kHz) plotted against the defect size, for various values of the Q-factor.*

4.5.2 Case with residual stresses

In the case with no residual stresses analysed in this section so far, the crack faces are either completely mating or not at all in contact: effectively the crack tip acts like a hinge. In many real-life situations there is likely to be some residual stress in the cracked region [60]. The clear strain dependence observed in the experimental results (see Figures 4.8 and 4.9) also indicates that the cracks do not behave as simple on/off switch. When compressive stresses are present around the crack, the tensile bending stresses will have to overcome the residual compressive ones in order for the crack to open. The variation of crack closure with time is no longer a simple square function since it then depends on the instantaneous value of the bending strain. The crack faces gradually mate over an increasingly larger area thus progressively reducing the defect size so that the "breathing" is smooth. Intuitively it is clear

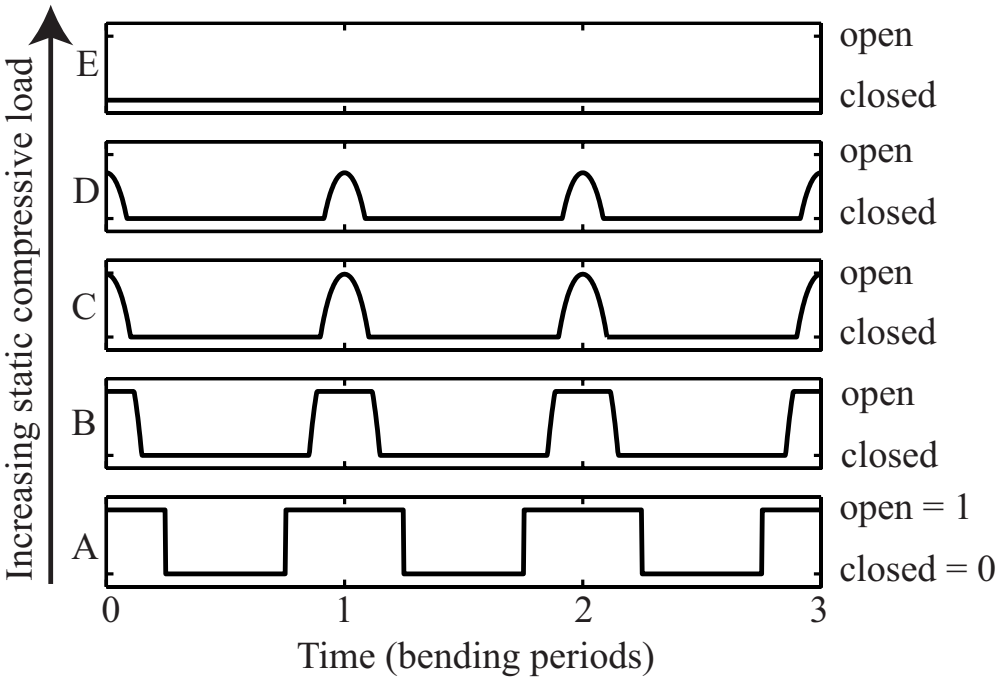

Figure 4.16: *Variation of opening of the crack with time for varying magnitudes of static compressive load. This load is very light in case A and is increased gradually from case A to E. The opening at a given time is represented by a number between 0 (fully closed) and 1 (fully open). The time is given in multiples of the bending mode period T.*

that the effect of this type of breathing on the modulation is that, depending on the relative value of the static stresses compared to the bending stresses, the "effective" crack size can be significantly smaller than the actual size [60,61]. This is confirmed by the following simplified analysis.

Crack closure in the presence of a static compressive stress

Consider a beam under a static compressive load P_c, also subjected to a sinusoidally oscillating bending moment. The resultant stress is then given by [71]

$$\sigma = \frac{yM_0 sin(2\pi t/T)}{I} - \frac{P_c}{A_{cs}} \tag{4.7}$$

where A_{cs} is the cross-section area of the beam, I its second moment of area, y the distance from the neutral axis, and M_0 the amplitude of the bending moment,

which oscillates with a period T. M_0 was chosen so that it induces a strain of 100 $\mu\epsilon$ at the top surface of a beam whose properties are the same as those assumed for the experimental specimens. Therefore the values of P obtained through this analysis are plausible experimental compressive stresses for the beams considered here. The crack was considered open when the resultant stress becomes tensile within the cracked region (here taken as the top 10% of the beam height). Figure 4.16 presents some results obtained from this model. This set of plots shows the degree of opening and closing of the crack as the bending moment goes through three periods of oscillation T. The opening is represented by a number between 0 (closed) and 1 (fully open). Each subplot, labeled from A to E, corresponds to a different value of the static compressive load. The particular cases shown were chosen because they illustrate the various possibilities of crack closure allowed by the model, whilst the numerical values used to obtain them are of no particular interest at this stage. Plot A shows the result obtained when the static load is very low. The crack then actually behaves as described in the previous section for a cracked region free of residual stresses. At the other extreme, case E corresponds to a very large value of the compressive load. The static stress is then so large that it cannot be overcome by the tensile bending stress; consequently the crack remains closed. Plots B to D are intermediate cases. In case B, the static compressive stress is low enough to allow the crack to open fully but the time it stays open is shortened compared to case A. In case D, the crack can never open completely. Case C is the limiting case between B and D where the crack just reaches full opening but does not stay open for a finite duration.

The influence of compressive stresses

Case D of Figure 4.16 will be treated as reference because it possesses the interesting feature that the crack is never fully open. According to the model, the transfer function shift is directly related to the change in crack closure; therefore, one can expect the shape of the modulating function to follow that of case D of Figure 4.16 although scaled so that H_o is the value reached when the crack is at its maximum

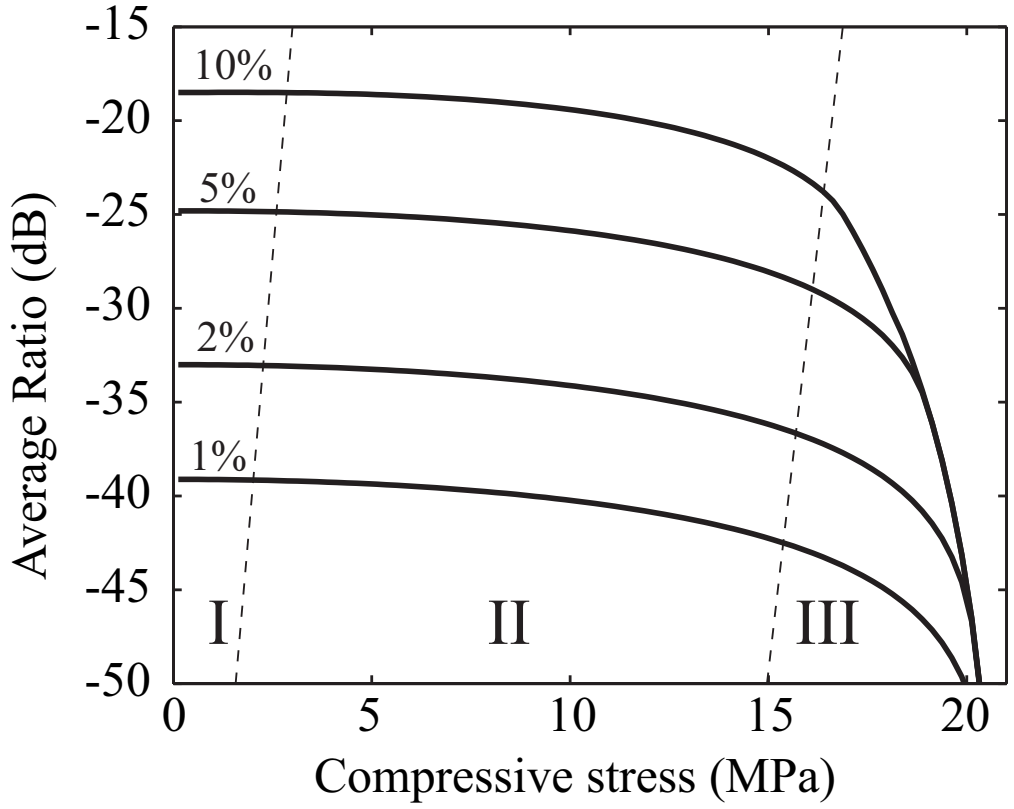

Figure 4.17: *Average ratio R vs compressive stress for different values of total crack depth (indicated above each curve as a percentage of beam cross-section area). In region I, the beam effectively behaves as if there was no compressive stresses. In region II, the crack opens fully but the time it stays open decreases gradually as the compressive stress increases. Region III corresponds to cases where the crack only partially opens. All four curves were obtained for Q=1000.*

(but partial) opening and H_c is the value when the crack is closed. In case D in Figure 4.16, the crack opens over 70% of its total depth. If the *total* crack depth is 10% of the beam depth, this means that the *effective* crack depth is around 7%. Once this is known, it is possible to compute the transfer function for a beam with a 7% crack depth; this transfer function is then used for $H_o(f)$. As before, $H_c(f)$ is computed for the reference uncracked beam. Once these two transfer functions are known, the modulating function (now normalized between 0 and 1) can be scaled appropriately for each ultrasonic frequency. The sidebands-to-carrier ratio is then obtained from the coefficients of the numerical FFT of this scaled modulating

function (refer to equation 4.5). This procedure can be repeated for various values of the static compressive load encompassing all the cases shown in Figure 4.16. The result from such an analysis is shown in Figure 4.17, which shows the averaged vibro-modulation ratio against the static compressive load. The different solid line curves show the variation of the averaged ratio for various total crack depths, indicated above each curve as a percentage of the beam cross-section area. All these curves were obtained for Q=1000. Two dashed lines define three regions, labeled I, II, and III in Figure 4.17. In region I, the beam effectively behaves as if there was no compressive stresses: the compressive stress is not large enough to alter significantly the square modulating function. Therefore the average ratio remains constant at around -18 dB for the top curve which was the value previously obtained with no residual stresses at an equivalent crack depth of 10%, and Q=1000. Case A in Figure 4.16 belongs to this region. In region II, the crack opens fully but the time it stays open decreases gradually as the compressive stress increases. In this region, the two transfer functions corresponding to the two extreme states are always the same: for the closed state it is still the reference $H_c(f)$ and in the open state it is $H_o(f)$ for a crack opened over its full depth. Within this range of stress, the slow decrease in the ratio is solely due to the shortening of the time the crack remains fully open. Therefore, although the two extreme transfer functions are the same, the average ratio decreases slowly from -18 to -25 dB with increasing compressive stress. This type of behaviour is exemplified by case B in Figure 4.16. Cases A and B in Figure 4.16 have different Fourier transforms although the crack opens fully in both cases. Region III corresponds to cases where the crack only partially opens as in case D of Figure 4.16. As can be expected, the averaged ratio then drops severely: as the stress increases in this region a point is reached at which the crack no longer opens. The average ratio then becomes minus infinity (this was cut off from Figure 4.17 to allow other features to be seen more clearly).

This analysis provides an insight into the effect of the level of bending strain necessary to observe a vibro-modulation effect. Some residual compressive stresses are often present around fatigue cracks. The strain induced by the low frequency vibration will then have to be large enough to overcome these compressive stresses.

This has important practical consequences since a defect will not be detected if the bending strain threshold is not reached. If the threshold is reached but the low frequency strain is not large enough to allow the crack to open fully, then the system effectively behaves as if the crack size had been reduced, thus resulting in a loss of sensitivity.

Other crack features can affect the modulation process. An important case is when the crack is partially open when the beam is unloaded. Intuitively, it is clear that the beam will have to bend further to cause the crack to be fully closed. One simple way to model this feature is to change the sign of the static stress P in equation 4.7. The residual stress then becomes tensile. The conclusions concerning the crack opening are similar, reversing the role of tensile and compressive stresses: it is necessary to reach a threshold of compressive bending stress for the crack to start closing and the modulation effect to be observed, thus resulting again in a loss of sensitivity.

4.6 Effect of partial crack opening

As the simulation work was carried out with a cracked area of 10% of the beam total cross-section area, the experimental and theoretical results were first compared for specimen M-2 whose cracked area was measured to be 10.6%. The average ratio level for this specimen ranged from -63 dB at 10 $\mu\epsilon$ to -55 dB at 50 $\mu\epsilon$ (see Figure 4.10). On the other hand, for an unstressed 10% crack size, the ratio obtained by finite-element modelling averaged over the frequency range 50 - 200 kHz ranged from -23 dB for Q=1000 to -34 dB for Q=100 (see Figure 4.15). Similar levels of discrepancies were obtained for all the other beams initially tested (L-1, M-1, S-1, L-2 and S-2). This confirmed the need to investigate more closely the state of opening of the crack when the beam is unloaded.

As mentioned in section 2.4.1, the specimen CO was manufactured after the main series of tests on the other six beams was completed, when it became apparent that the initial partial crack opening was likely to be significant in VAM testing. The compliance method described in section 2.3.1 was used in order to estimate the

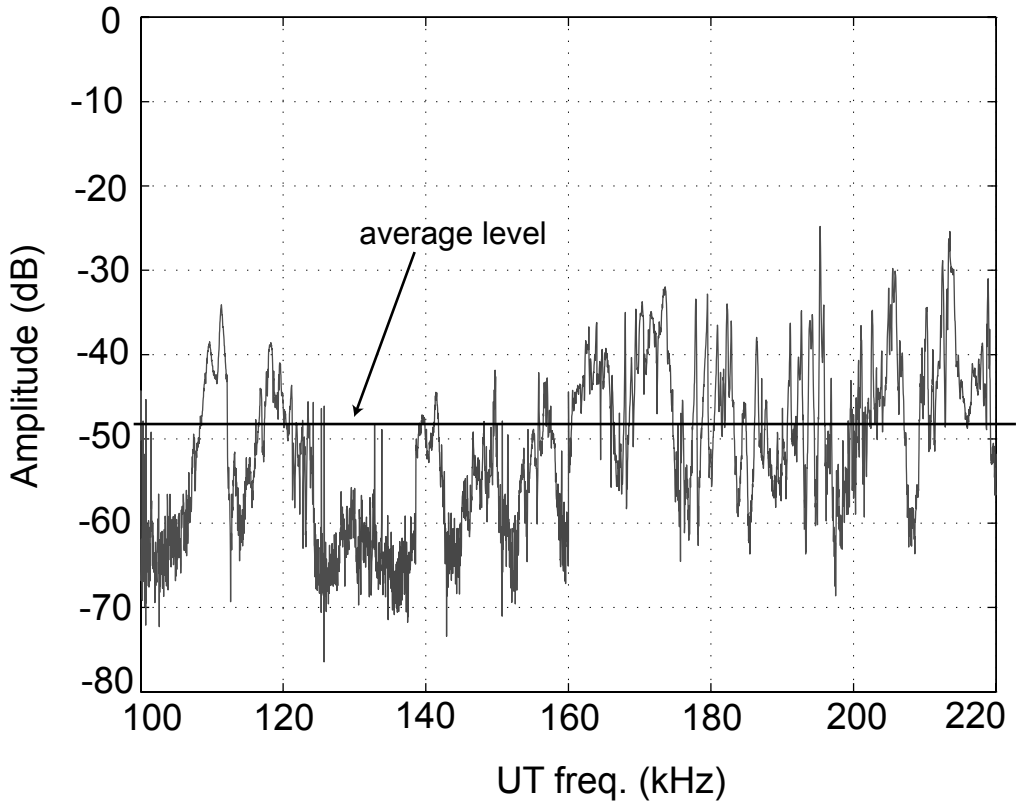

Figure 4.18: *Amplitude of the sidebands-to-carrier ratio vs UT frequency for specimen CO at 80 $\mu\epsilon$ (peak value, average during decay) LF vibration level.*

initial partial opening of specimen CO when the beam was in its unloaded state. It is recalled that, if the back-face strain is plotted against the load, a narrow ellipse is obtained, provided the load applied does not exceed the linear limit. This is shown in the upper curve of Figure 2.6 which corresponds to loading with the crack on the upper face of the beam in Figure 2.4, so that increased loading tended to close the crack. The hysteresis observed (area inside the stress/strain curve) is essentially due to damping. If the cross-crack strain is plotted against the load a straight ellipse cannot be obtained since the crack closure or opening changes the stress/strain characteristic. The results were shown in the lower curve in Figure 2.6. In the region between approximately -0.8 and -1.4 kN the crack is in transition between the full and partial closure states. Figure 2.6 showed that a compressive load of about -1.1 kN corresponding to a back-face strain of about 220 $\mu\epsilon$ was necessary to fully close the crack. The same experiment conducted with the beam turned over for opening the crack showed that the crack was fully open at a load of about -0.1

kN with a back-face strain around -30 $\mu\epsilon$. Since the full opening load (-0.1 kN) is smaller than the full closure load (-1.1 kN), it could be concluded that the interfaces of the cracks produced in specimens L-2, M-2, S-2, and CO (cracked using the same fatigue settings) were partially open at the end of fatiguing. The effect of this on the ultrasound modulation during the VAM tests can then be discussed.

It has been shown that for specimen CO, a strain of 220 $\mu\epsilon$ at the back-face was required to close the crack fully, and -30 $\mu\epsilon$ at the back-face resulted in the crack opening fully. The maximum low frequency strain just after impact was on average about $\pm$80 $\mu\epsilon$ for specimen CO. Therefore the degree of crack opening was changing between -30 and +80 $\mu\epsilon$. For the crack state to vary between fully open and fully closed, the strain would need to vary between (at least) -30 and +220 $\mu\epsilon$. Therefore the fraction of the crack area contributing to the modulation was (30+80) / (30+220)=0.44. Since the measured crack area was 8.5% for CO, the effective crack area was about 3.7%. For a crack of this size the finite element model predicted ratio levels around -45 dB for a Q of a few hundreds. The Q-factors of the isolated peaks around 100 kHz were measured for specimen CO. The values were mostly below 100 with a few reaching 200 to a maximum of 500. The experimental sidebands-to-carrier ratio for this specimen is shown in Figure 4.18. The average ratio for a strain of 80 $\mu\epsilon$ was measured at -48 dB. This value is similar to the predicted value of -45 dB, provided the effective crack size is considered. Given the simplicity of the models, the level of agreement is encouraging.

4.7 Example of detection of cracks in industrial samples

The reliability of the IHS rig made it possible to test real samples. The cracked nickel-base alloy specimen that was inspected is shown in Figure 4.19 (a); the crack is surface breaking on one side of the piece and measures approximately 18 mm in length whilst the maximum depth is unknown. The strain gauge was placed on top

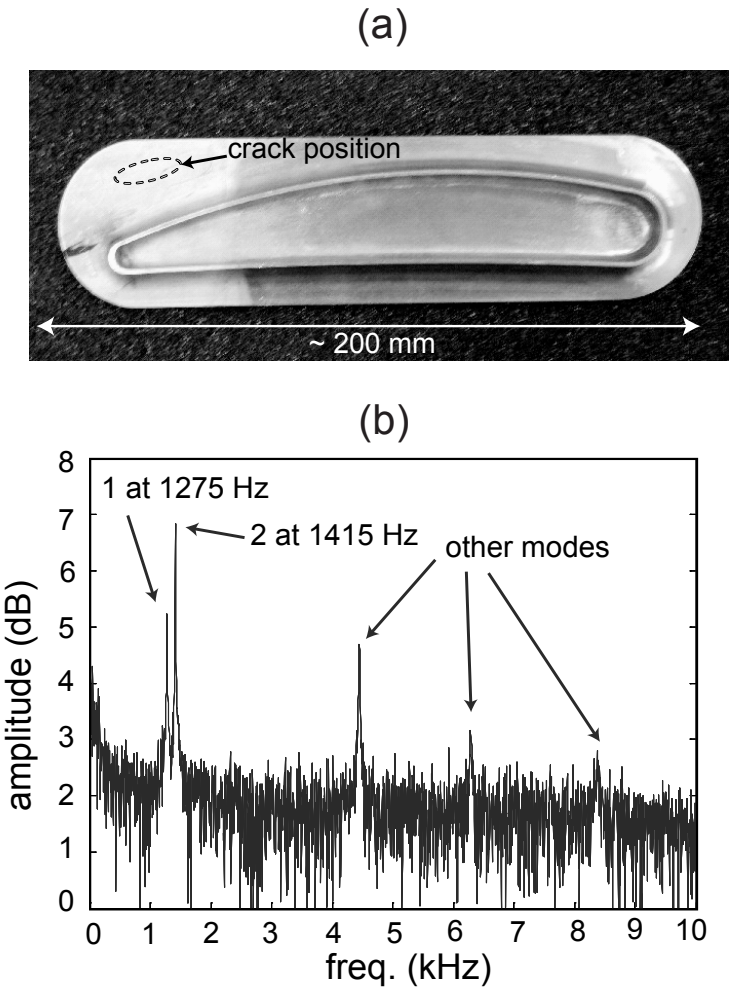

Figure 4.19: *(a) Picture of the nickel-base alloy industrial sample. (b) FFT of the strain recorded along the transient of decay of the LF vibration excited by an impact on this specimen.*

of the crack and in the direction transverse to its length, in order to obtain a measure of its geometrical deformation during the transient of the low frequency structural vibration. The sample was suspended in a similar manner to that described in the previous section. One rubber stud with a string passing through it was attached at the back of the specimens near the edge at one end, and the specimen was then suspended from this point. The low frequency modes [see Figure 4.19 (b)] were excited by tapping at the other end. Only the sidebands corresponding to the 1st and 2nd mode of Figure 4.19 (b) were taken into account in the post-processing of

the measurements. Figure 4.20 shows a comparison of the results obtained from tests on a cracked sample [Figures 4.20 (a) and (b)] and an undamaged one of the same type [4.20 (c)]. As usual, the amplitudes of the ultrasonic carrier and the sideband-to-carrier ratio are plotted vs the ultrasonic frequency and for decreasing values of average low frequency strain along the vibration decay following each impact. The difference in the level of the ratio of the average first sidebands over the fundamental is significant and the strain dependence of the sidebands for the cracked specimen is clearly visible, despite the very low level of strain excited at the crack location (about 8 $\mu\epsilon$ peak value) in both modes considered. This confirmed the reliability of the suspension rig. The ultrasonic frequency sweep carried out to obtain these results was performed over a relatively narrower band (only 6 kHz) compared to that used in the experiments on the cracked beams following the indication that a point of maximum sensitivity would be found inside that range. Although this was less time consuming compared to the broad range sweeps carried out on the set of laboratory beams, nearly half an hour was required to obtain a result on the presence of a crack.

4.8 Feasibility of "in-situ" measurements

A situation that can be of interest for the practical exploitation of VAM for NDT is the detection of cracks within assembled structures. Having experienced reliability problems due to supports and shaker attachment, a preliminary setup was used for an initial feasibility study. This rig is shown in Figure 4.21 (a). An uncracked rectangular-cross-section beam of sides 10 and 20 mm was instrumented with two PZT discs and a strain gauge. The constraint was realized by a holding the beam in a vice. Then an impact was used to excite the bending modes of the cantilever. The spectrum of the signal picked up by the strain gauge showed several low frequency bending modes excited. Figure 4.21 (b) shows the presence of substantial sidebands (comparable to those typically observed on the cracked specimens tested earlier using the suspension setup) even in absence of damage. It is thought that the ultrasound could be modulated by the contact at the interfaces between the beam and the vice,

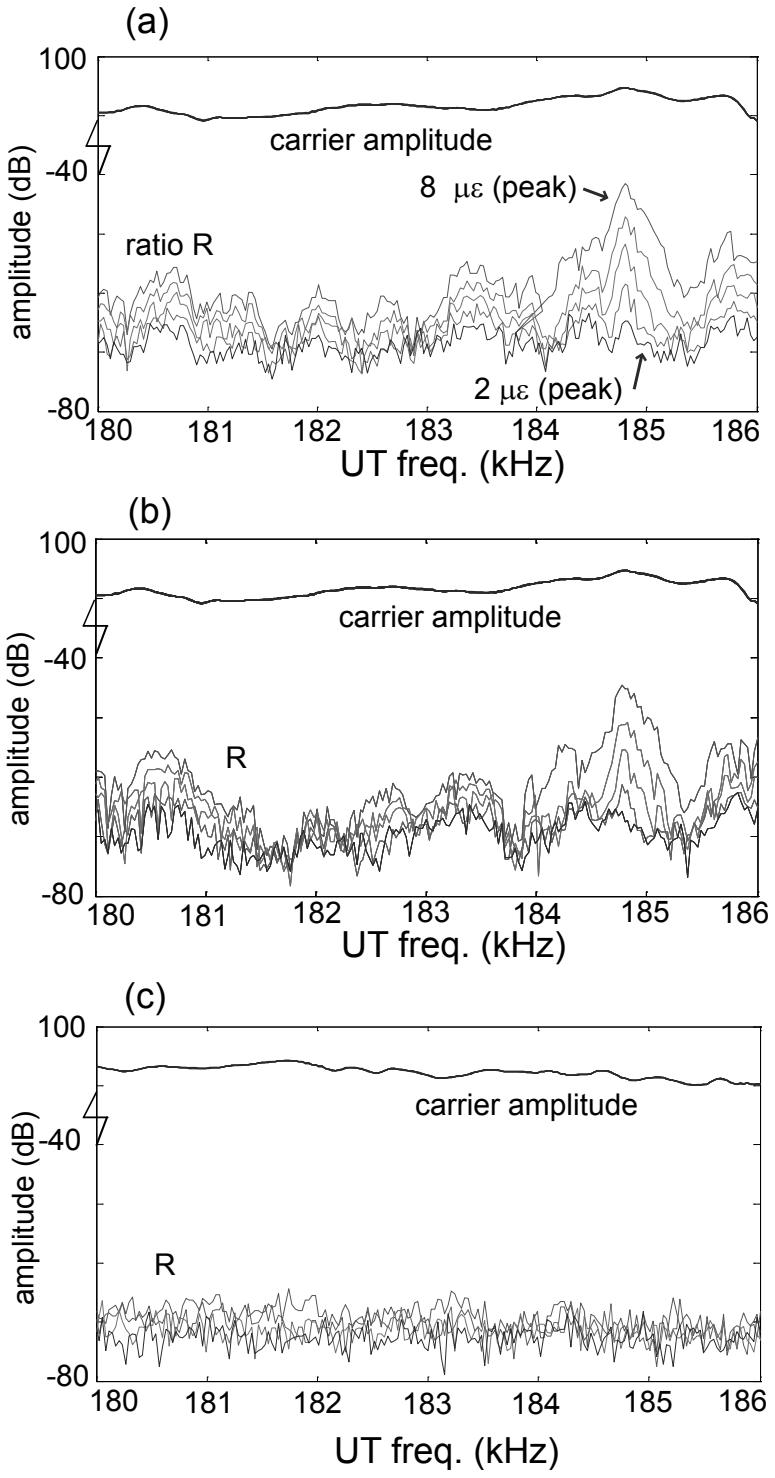

Figure 4.20: *Crack detection in the industrial component of Figure 4.19 using the IHS rig. (a) UT fundamental amplitude and ratio (R) curves for the sidebands generated by mode 1 of Figure 4.19 plotted vs UT frequency. (b) Fundamental amplitude and R for the sidebands generated by mode 2 of Figure 4.19 vs UT frequency. (c) Fundamental amplitude and R for an uncracked specimen vs UT frequency (mode 1 is considered).*

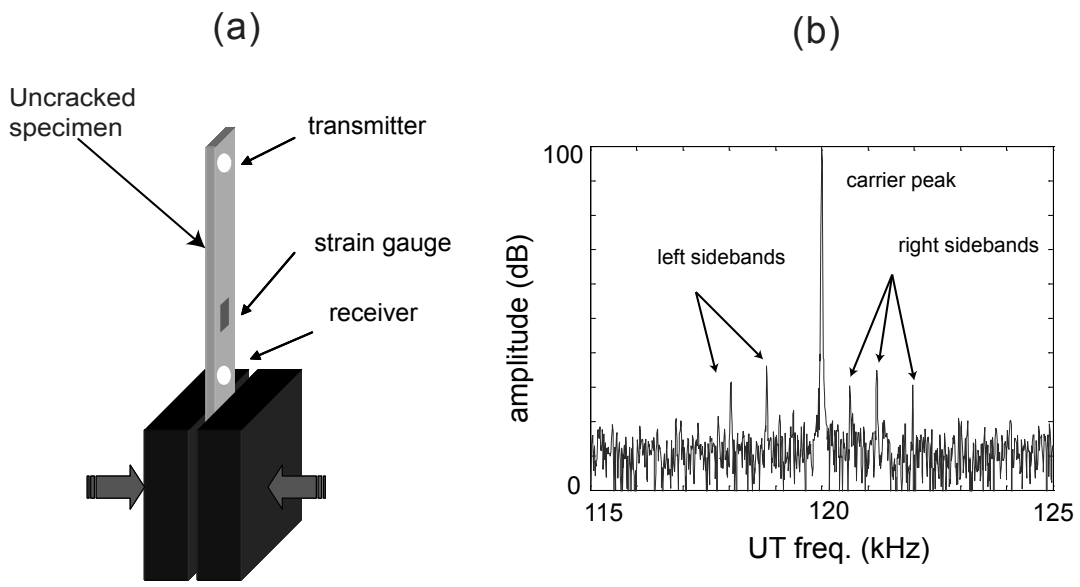

Figure 4.21: *(a) Schematic of the VAM rig with a cantilever beam. (b) Example of FFT of an ultrasonic probing signal received during LF vibrations excited using an impact.*

in such a way as to generate sidebands of the same kind as those observed in the presence of the crack. In testing practice, this corresponds to having an increased coherent noise level, if the detection of a crack had to be performed by VAM. In such a condition it is believed that only a very large crack would be able to provide an additional amplitude modulation of the ultrasound high enough to be detected reliably in the presence of such nonlinearities at the supports.

4.9 Review of Chapter

In this Chapter it has been shown that the engineering of the testing rig is crucial to detect cracks reliably using the VAM method. Appropriate supports and excitation devices have to be used in order to allow the modulation of the probing ultrasound (i.e. the sidebands in the frequency domain) due to the crack to be detectable. The supports and/or any other contact between the specimen and other external bodies are very likely to introduce sidebands at the same levels as those generated by a crack, and this could jeopardize the successful application of the VAM NDT method. It was found that the impact-hammer suspension setup gave sidebands

about -65 dB below the carrier amplitude for an undamaged specimen and this was satisfactory for crack detection. A damage index was defined and its value calculated for each of the laboratory beams using the impact-based rig. While the value of the damage index generally increased with crack size, the relationship was far from linear. This is likely to be due to different crack morphologies or initial degree of crack opening/closure due to the different fatigue conditions used to produce the cracks. The trend obtained suggests that the smallest cracks that could be detected must be at least 7% of the cross-section area. Therefore, the technique (in the implementation used in this study) will not be able to detect small cracks reliably. An overview of a simple model was included in this Chapter to explain that the overall level of the sidebands predicted was in broad agreement with the sidebands level measured experimentally, provided the state of static opening of the crack is considered carefully. Given the poor sensitivity to cracks and the time required to sweep the ultrasonic frequency in order to ensure that a peak of sensitivity is obtained, this implementation of the vibro-acoustic modulation technique does not appear to offer significant potential for rapid screening for the detection of small cracks. However, other vibro-modulation implementations (for example using surface acoustic waves and local probing [60, 61]) may be more sensitive. Based on the findings of this Chapter, it was decided to concentrate the research solely on the thermosonic method since it appeared to offer an important advantage over VAM: the crack can be detected and its position over a large area can be determined with a single quick thermal measurement.

Chapter 5

Prediction of the thermosonic signal

The purpose of this Chapter is to predict the surface temperature rise used to detect cracks in thermosonics nondestructive testing (NDT) from the measurement of the vibrational strain excited in the test-piece. This link between vibration input and thermal output will form the physical background necessary to allow, in the next Chapter, the prediction of the general threshold level of vibration required to detect cracks reliably.

5.1 Background

Thermal nondestructive evaluation (NDE) techniques have been an active subject of research since the late 70s [72]. The commercial availability of infrared (IR) cameras contributed to their continuing success, by offering rapid and large area testing methods at an increasingly affordable price [73, 74]. Thermosonics (or sonic-IR) is an emerging thermal NDT method which is based on detecting the heat generated by fatigue cracks in metals or delaminations in composites when a powerful ultrasonic excitation is applied to the test structure [72]. Vibro-thermal NDE techniques were pioneered in the early 80s: Pye et al. [75, 76] studied the heat emission from defects

in a low frequency steady state vibration field, whereas Mignogna et al. [7] applied ultrasonic excitation for several seconds and recorded IR images of the sample during that time. However, due to the limited sensitivity (in the order of 0.2 $°C$) of the IR cameras available in those years, successful practical applications of thermosonics have been reported only from the late 90s [77–79]. High power acoustic resonators (refer to section 5.2.1), with a fixed resonance frequency typically at 20 or 40 kHz, have been used to excite high amplitudes of vibration so that the heat generated at the defect is large enough to be detected by an IR camera as a surface temperature rise (thermosonic signal) [80, 81].

Thermosonics is currently implemented in two different fashions. In the first one, known as "lock-in" ultrasound stimulated thermography (UST) [77, 78, 80], the ultrasonic wave used to excite the structure is amplitude modulated at a very low frequency and the IR images are acquired for several seconds and processed in the frequency domain. The main advantage of this method is that a relatively low excitation power can be used. A conceptually similar version of "lock-in" UST is "burst phase" UST [82], which aims to reduce the testing time. The benefits of frequency modulation were also recently investigated to improve the reliability of the detection of damage in composites by eliminating heating patterns due to resonant vibrations [83]. In the second implementation, the vibration is applied for a very short time (normally under one second) with the aim of producing a quantity of heat at the defect that is large enough to be readily detected in the form of surface temperature rise by the IR camera [79, 81, 84]. In this way very quick defect detection can be achieved. Very small cracks in metallic structures, having a high conductivity coefficient, have also been successfully detected using this method [85, 86]. In this study we investigated the pulse variant of sonic-IR, since it is quicker and simpler to implement.

The acoustic horn is a very crude means of exciting high power vibration in structures. This device can be hand pressed against the test structure or can be loaded against the structure using a spring, but it is not usually rigidly joined [6]. The nonlinearity of the coupling between the test specimen and the acoustic horn typi-

cally results in the excitation of super-harmonics and sub-harmonics of the driving frequency [87]. When a large number of such frequency components are excited, acoustic "chaos" can result and this sort of broadband excitation has been demonstrated to enhance the thermosonic signal [88], although the vibrations produced in the test sample tend to be highly non-reproducible (this will be treated in detail in section 5.2.4). Researchers have recently advanced the understanding of the mechanisms of generation of acoustic "chaos" obtained using conventional acoustic horns, and have investigated the consequent improvement in the defect detection [89–91]. Nevertheless, more quantitative and systematic work is still needed for thermosonics to become a fully reliable NDT technique. This work proposes a further step in this direction and its objective is to determine quantitatively the relationship between the vibration strain level and the surface temperature rise obtained from a crack. The idea is to extend the approach proposed by Pye and Adams in the 80s [75, 76], who predicted the near-damage temperature field in composites through estimates of the defect damping. After this link between vibration input and thermal output has been established, it will be possible to find the minimum threshold strain amplitude that allows reliable crack detection (Chapter 6).

5.1.1 Proposed approach

The prediction process involves two logical steps: first, modelling the heat released *at the crack* when the specimen is vibrated and, second, obtaining the resulting temperature rise *at the surface* due to heat propagation. In this Chapter, the heat produced at the crack will be determined using the damping measurements discussed in Chapter 3. Ideally one would model directly the heat generated by a crack from the knowledge of the crack size and vibration pattern. However this is a difficult task as the result would depend strongly on the detailed features of that particular crack, such as its morphology, its surface roughness, the state of stress around it and its degree of initial partial opening. In contrast, vibration damping represents the global loss of energy in a vibrating system: it is a quantity which accounts for all forms of dissipation at work in a system [26] such as internal material losses,

dissipation at the joints and supports, etc. It has been known for a long time that the presence of a crack in a specimen can contribute to a significant increase in the overall damping and this is the basis of a NDT technique on its own right [19]. For this technique to be successful, the damping increase due to a crack must constitute a significant fraction of the overall damping. Therefore it works best for initially lightly damped structures but its sensitivity is severely affected if the baseline damping (i.e. without crack) is large, either because the material is lossy or because there is too much dissipation at the supports, joints etc. On the other hand, thermosonics offers a local monitoring of heating such that even if significant losses occur at the supports while the structure is vibrated, the heating produced by a defect can still be observed provided it is located far enough from the other heat sources. This study was carried out on the set of laboratory steel beams described in section 2.4.2. The estimate of the crack additional damping obtained in Chapter 3 can be combined with knowledge of the vibration amplitude as a function of time during the thermosonic tests to yield an estimate of the heat released at the crack versus time. This can then be input to a thermal model in which the crack acts as a heat source to give the monitoring surface temperature as a function of time. Investigations making use of experimental damping data were carried out by Pye and Adams [75, 76], but they only studied composite samples with impact or saw-cut damage vibrated at low frequency resonances (up to around 250 Hz). This study presents results obtained applying transient vibration at ultrasonic frequencies (40 kHz and above) to steel specimens with fatigue cracks.

5.2 Experimental setup

5.2.1 Characterization of exciter

Ultrasonic horns are not part of the standard equipment generally used in vibration research. These acoustic resonators [or sonotrodes, one of them is shown in Figure 5.1 (a)] were originally designed for a variety of applications such as cleaning baths,

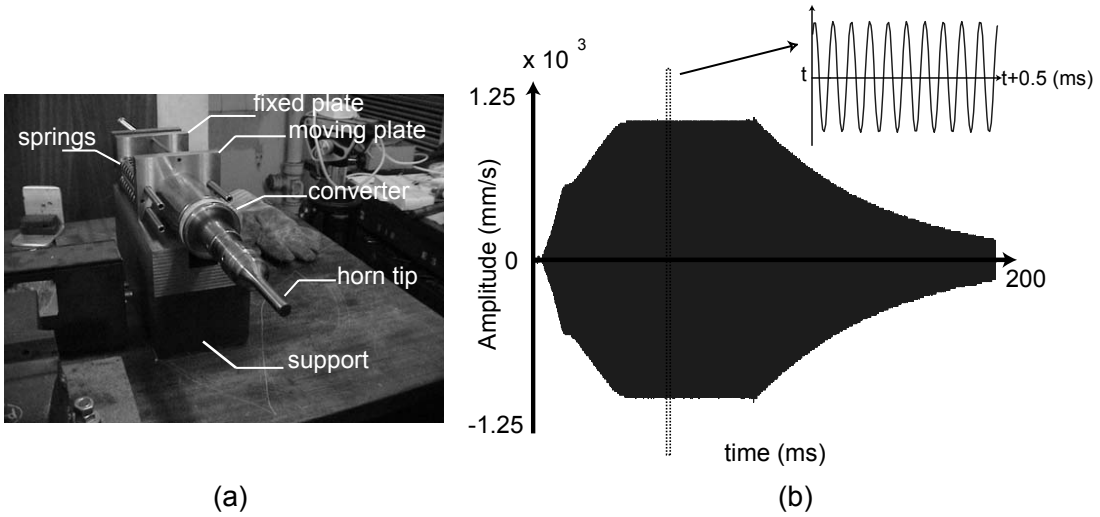

Figure 5.1: *Thermosonic exciter and its vibration characteristics. (a) 20 kHz acoustic horn mounted on spring supports for loading against the test-piece. (b) Vibration of the horn tip in the unloaded status: onset transient, regime and decay after interruption of electric alimentation.*

stimulation of chemical reactions, welding of plastics, industrial cutting of foods, surgical cutting of tissues or bones, etc.. However, they can be used successfully to excite the thermosonic signal. For a given material of known thermal properties, the magnitude of the temperature rise in the region of the defect depends on the excitation of a high number of cycles per unit time, and on sufficient energy being dissipated per cycle. These considerations have driven the selection of the ultrasonic horns as exciters in sonic-IR: they provide high frequency and high amplitude. The ultrasonic horn shown in Figure 5.1 (a) is part of the Branson digital sonifier model 450 system. It comprises a horn, a converter and a power amplifier. In Figure 5.1 (a), the Branson horn is shown with the support system specifically designed for thermosonics testing. The support is composed of a block of steel with a groove that allows the horn to slide in the horizontal direction with minimum friction. The assembled horn and converter are backed by a moving plate, which can slide on the same groove. The moving plate is pushed by a set of four springs hosted by a fixed plate mounted at the back of the supporting block using screws. The power amplifier, rated at 400 W, supplies an alternating electrical voltage across a system of two piezoelectric (PZT) discs which is housed in the converter. The

acoustic horn is a metallic (steel, titanium) longitudinal tapered element with a decreasing cross section. It is attached to the converter by a threaded stud placed at the larger cross-section end. The tapered shape can have several profiles, for example exponential, linear, or double stepped. The tapered shape shown in Figure 5.1 (a) is exponential. The horn is a mechanical amplifier of axial displacement, due to its tapered form. The system formed by the horn and the attached PZT discs is a mechanical longitudinal resonator. The horn resonance is tuned to 20 kHz via its length which corresponds to half wavelength of the first longitudinal mode of a one-dimensional structure. Although the nominal resonance frequency of this axial resonator is 20 kHz, the actual axial vibration of the horn may fall within the range from 19.5 to 20.5 kHz, depending on the external loading conditions. If the loading conditions are such that the resonance of the horn is outside this range, the horn tunes automatically to the point of maximum displacement within the allowed frequency range, and is able to supply, at this working point, up to the nominal limit of absorbed electrical power of 400 W. However, the actual power supplied to the horn depends on the matching between the electrical output impedance of the power amplifier (fixed) and the electrical input impedance of the converter/horn assembly (depends on the horn loading condition). If the impedance mismatch is too severe, the electric power is reflected back towards the power amplifier and a safety cut-off circuit prevents functioning. A laser vibrometer was used to measure the velocity of the horn tip (unloaded) in operation. Figure 5.1 (b) shows the measured value of the axial velocity over a time period of 200 ms. The onset transient lasts approximately 30 ms, after which a steady state is reached and a constant amplitude is kept until the time specified by the pulse duration setting [100 ms in Figure 5.1 (b)]. After the power supply has been interrupted the amplitude of the horn tip vibration decreases. In Figure 5.1 (b) a zoom on 10 cycles of the vibration in the regime region is also shown. The vibration appears to be a virtually perfect sine-wave at around 20 kHz, and this was also confirmed by a frequency analysis of the time trace shown in Figure 5.1 (b).

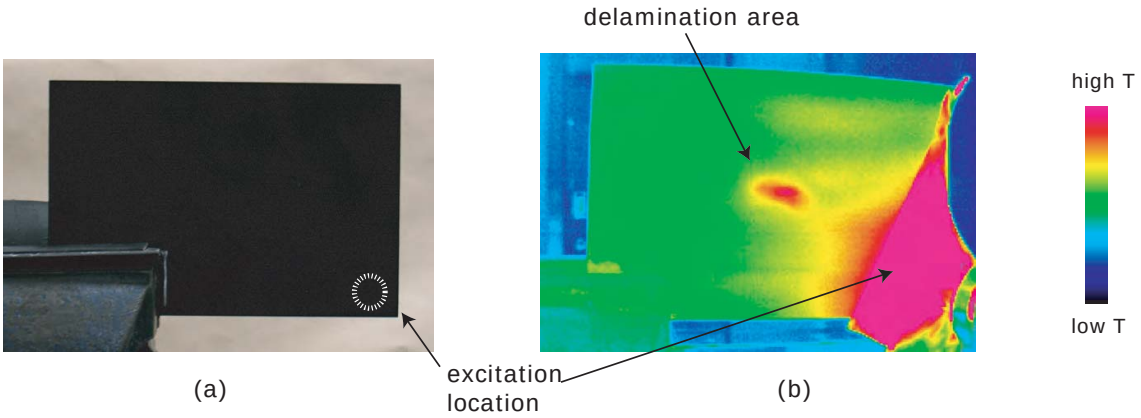

Figure 5.2: *(a) Example of CFRP plate held in a vice for thermosonics testing. (b) Thermal imaging of the delamination during thermosonic excitation using the 20 kHz system.*

5.2.2 Initial trials on perspex and CFRP

Initial tests were carried out on carbon fiber reinforced polymer (CFRP) plates as well as perspex beams since these materials have a lower thermal conductivity than metals, hence allowing a temperature rise to be measured on the defects even for relatively low vibration levels. An example of successful measurement of the thermosonic signal on a composite plate is shown in Figure 5.2. An impact damage was previously created in the plate by means of a metallic heavy ball dropped from a height. The damage typical of an impact is characterized by a portion of material with wide disbondings of the carbon fiber from the layers of resin. These disbondings are also referred to as delaminations. It is interesting to notice that the damage in this specimen was almost impossible to detect using conventional pulsed optical thermography techniques, due to effective heat transmission through the defect. The plate was held using a vice and the horn was pressed horizontally against either bottom corner of the plate, as seen in Figure 5.2 (a). The Branson horn was put in action for 1 second at 30% of the maximum output. The temperature signal measured with the thermal imaging camera reveals clearly a defective area [Figure 5.2 (b)]. The temperature map in Figure 5.2 (b) also shows a "hot" zone close to the excitation. Effectively this part is a "blind" zone for the thermosonic technique since

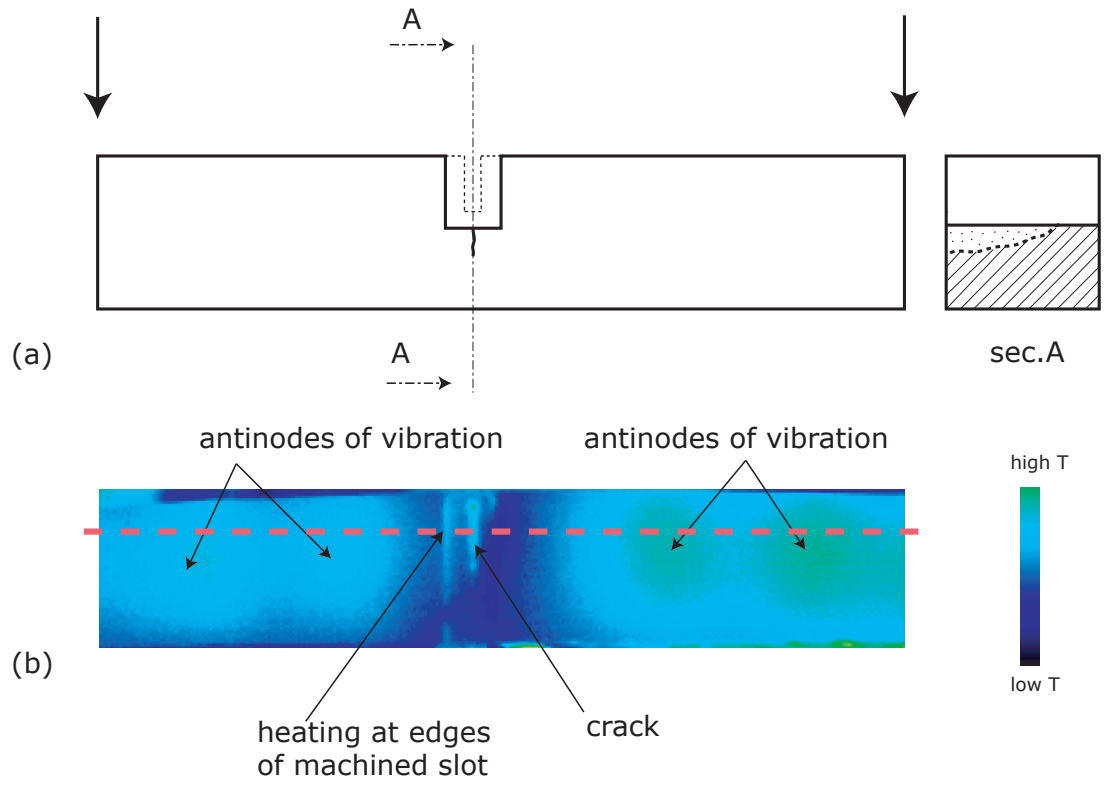

Figure 5.3: *(a) Drawing of specimen P-1 of Table 2.4 with notch machined off. (b) Example of thermal image during thermosonic excitation using the 20 kHz system; the vibration was measured along the dashed line using a laser vibrometer (see Figure 5.4).*

the heat coming from the dissipation at the excitation position locally increases the background temperature. Away from this confined zone the defect is correctly and quickly imaged. Further systematic studies were conducted on CFRP plates [P2], but are not part of the core work presented in this Thesis.

In Figure 5.3 (a) the drawing of a segment of the cracked perspex beam P-1 of Table 2.4 is shown; the crack was not through width and it was visible to the eye given the transparency of the material. The beam was instrumented with a strain gauge in order to measure the dynamic strain, and the cracked surface was painted in black to maximize the emissivity. The strain gauge was attached in the lengthwise direction, on the cross section containing the crack, on the side opposite to the notch. The Branson acoustic horn was operated in pulses of duration from 0.5 to 2 seconds for this specimen. The horn tip amplitude range was from 20% to 40% of the maximum

amplitude. The typical maximum value of strain measured in these experiments was around 90 $\mu\epsilon$. Figure 5.3 (a) shows the segment of the perspex beam P-1 which was later imaged using the IR camera during thermosonic excitation. It will be noticed that a portion of material around the notch was removed from the beam. This was done in order to have the crack mouth breaking across a flat surface. An example of an IR image taken from the image sequence recorded during a pulse by the thermal camera is provided in Figure 5.3 (b). It is possible to notice that a hot region formed on the crack mouth for its whole length (which did not extend over the full width of the beam). Furthermore, the edges of the slot machined in the specimen also appeared to have undergone a temperature increase; this was due to the stress concentration at the edges which resulted in a localized extra material dissipation. The dissipation of energy due to the material damping was certainly of relevance in this experiment as shown by the heating of the antinodes of the excited vibration mode in Figure 5.3 (b). If the direction of the dashed line of Figure 5.3 (b) is considered, it is possible to compare the amplitude of the vibration of the flexural dominant mode of this beam with resonance at around 20 kHz, measured using a single point laser Doppler vibrometer scanned along the length of the beam, with the magnitude of the thermal signal measured by the IR camera. This is shown in Figure 5.4. The crack is located approximately half way between an antinode and a node of the flexural mode that dominates the response of the beam. The zones of larger velocity match the zones of larger relative temperature increase, confirming that on these zones the temperature rise is generated by the dissipation of heat in the material. At this stage, perspex beams were regarded as suitable "learning specimens". The low thermal conductivity coefficient ($0.17 - 0.19 J/(K \times Kg)$ at 23 $^{\circ}C$) of the material allowed the heat to build up in the proximity of the defect. The result was an easily measurable temperature increase that revealed the cracks. However, the scope of this work was to test and study metallic cracked samples.

Although the initial thermosonic tests presented so far were carried out using the Branson system of Figure 5.1 (system designed for cleaning baths), this system proved to be unsatisfactory when the horn was heavily loaded against the test-piece due to excessive impedance mismatch. For the research on cracked metallic spec-

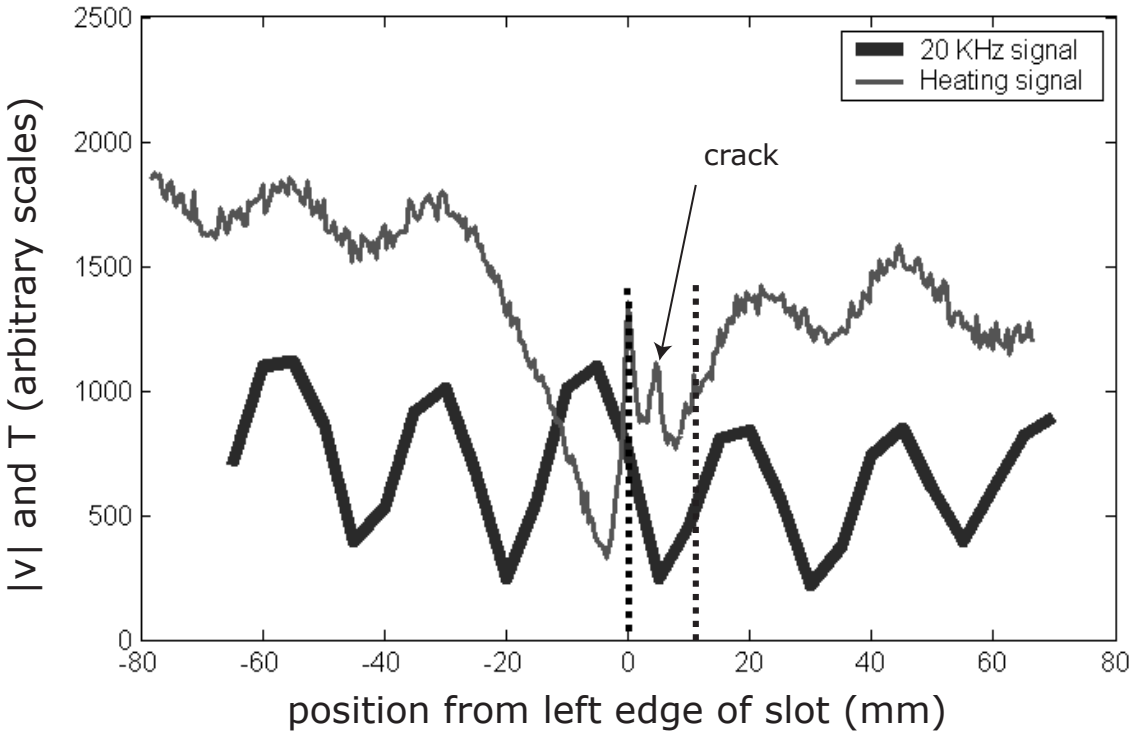

Figure 5.4: *Comparison between the modulus of the vibration velocity and the temperature rise measured along the dashed line of Figure 5.3.*

imens, the 20 kHz Branson system was replaced by a Sonotronic 40 kHz system originally designed for welding of plastics, and hence designed to work by loading it against a structure. The Branson and Sonotronic systems are two examples of acoustic horns, and comprise conceptually the same parts, which function in essentially the same way. The main differences between these systems are the center frequency and the output impedance of the power amplifier. The Sonotronic 40 kHz system was used for all the thermosonic tests on metallic samples presented in the remainder of this Chapter (this system is the one which appears in Figure 5.5).

5.2.3 Thermosonics testing rig

A picture of the standard experimental setup used on metals in this work is shown in Figure 5.5. The IR camera was pointed frontally at the cracked surface of the specimens, and the field of view adjusted over the whole crack width. This was the

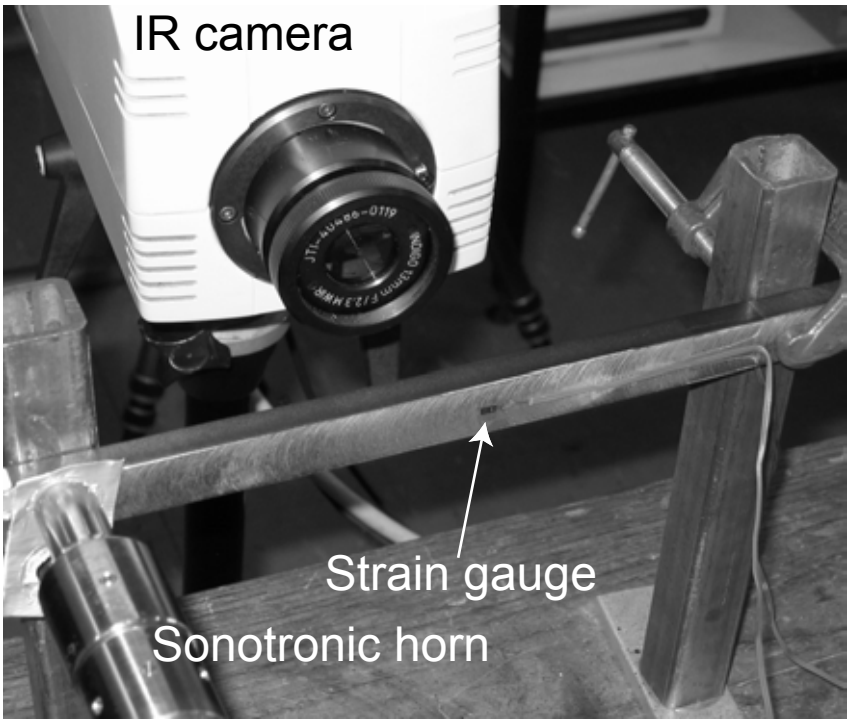

Figure 5.5: *Standard thermosonics testing setup; the camera is looking at the crack mouth ("top" of the crack) across the width of the specimen. The crack is on the other side of the strain gage.*

standard thermal measurement configuration. The beams were supported against two vertical posts. One end of the beams was held by a "G-clamp" and the ultrasonic horn was pressed against the other using the spring-loading supporting system of Figure 5.1 (a). Commercial duct tape was used between the horn and the beams to protect the latter from direct contact. Each beam was instrumented with a strain gauge bonded to the face of the beam opposite the crack (also called back-face, as defined in Chapter 2), in the longitudinal direction. The vibrational strain produced by each pulse was recorded for each test. The force applied to the beams by the horn acted in the direction perpendicular to their length, making the generation of axial and torsional vibrations of the beams unlikely. For this reason and because the cracks are located at the middle of the beams, and considering that the beams are long compared to the crack and cross-section dimensions, it was assumed here that the vibrations predominantly contributing to heat generation at the crack were

the odd flexural modes of the beams. Thus, the prediction of the thermosonic signal could be done on the basis of the damping measurements described in Chapter 3, as they were based on the excitation of such modes. Multiple tests were conducted on each cracked beam, varying the coupling conditions by repeatedly releasing and re-coupling the exciter to the beams.

5.2.4 Characteristics of excited vibrations

On the left-hand column of Figure 5.6 [Figures 5.6 (a), (c), (e) and (g)] four typical strain records are shown. The pulse duration was approximately 0.6 seconds in all tests. The amplitude of the strain was usually variable during the excitation time, as can be seen from the signal envelopes. In Figure 5.6 (a) the lowest average strain level amongst all tests carried out in this Chapter was excited (around 15 $\mu\epsilon$). The test shown in Figure 5.6 (c) is characterized by a strong variation of strain amplitude in time, with a maximum of about 60 $\mu\epsilon$ reached after around 0.2 seconds from the vibration onset. The cases of Figures 5.6 (e) and (g) show a less variable strain amplitude in time but a higher level of average strain, around 60 and 80 $\mu\epsilon$ respectively (this last test is an example of the highest strain amplitudes excited amongst all tests). Since the horn and the beams were not rigidly fixed and because the axial vibration of the horn tip reached relatively high amplitudes (the typical horn tip displacement was measured to be 6 μm), bouncing/hammering of the horn tip on the beams occurred in all tests, producing nonlinear vibrations. On the right-hand column, Figures 5.6 (b), (d), (f) and (h) show the strain spectrogram calculated using the short-time Fourier transform (STFT) method for the corresponding test on the left-hand column. In the case of Figure 5.6 (b), the spectrum is almost consistently formed by the driving frequency at around 40 kHz and by its first super-harmonic at around 80 kHz. For the test of Figure 5.6 (d), the super-harmonics at 120 kHz and 160 kHz are present in addition to the 40 kHz and 80 kHz components; around the time at which the strain reaches its maximum amplitude, the 120 kHz component (second super-harmonic of the driving frequency) seems to be the largest before vanishing and reappearing again at around 0.5 seconds. From this time until

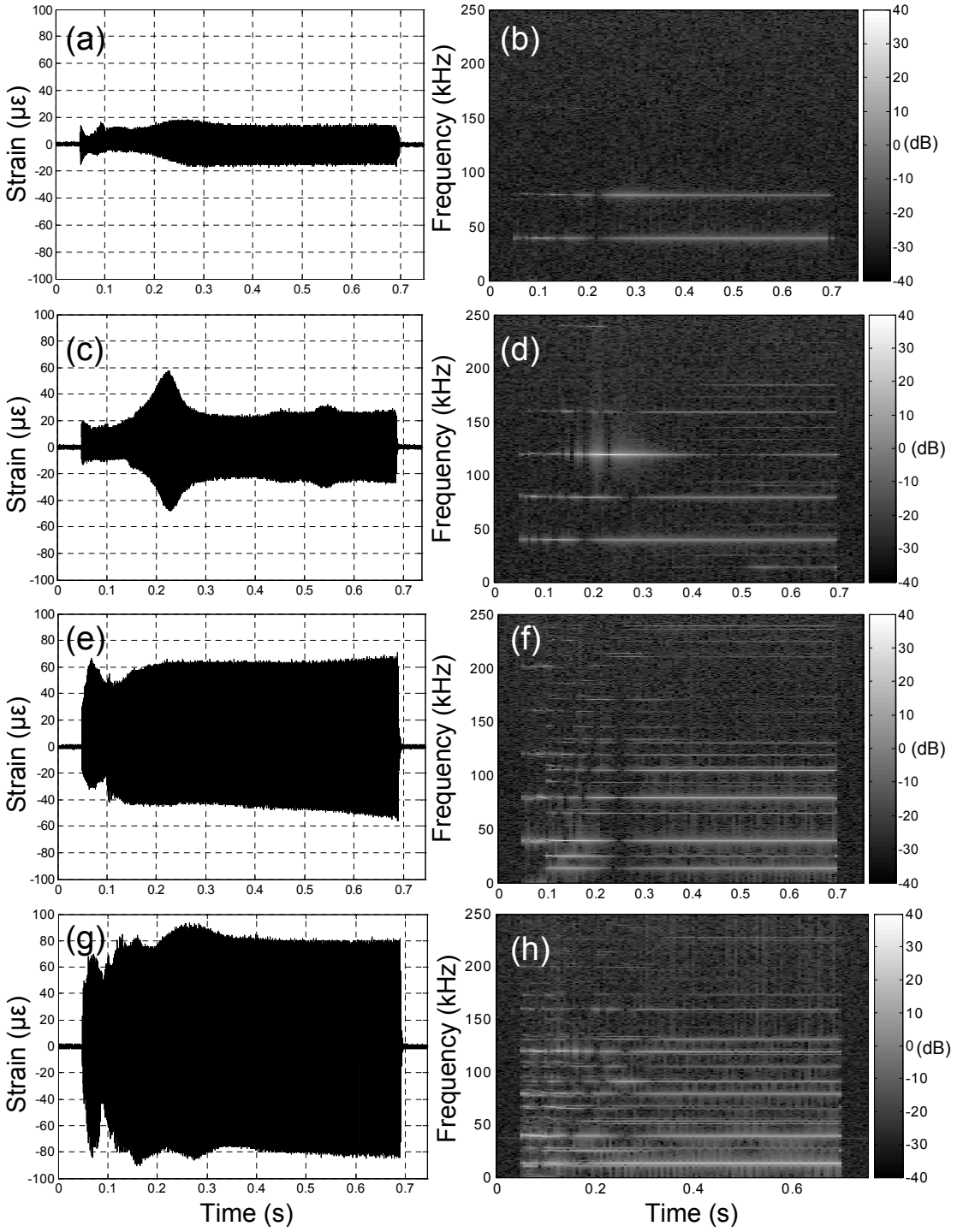

Figure 5.6: *Examples of strain records and corresponding short-time Fourier transform (STFT) spectrograms. (a) Strain record for test 7 on specimen T-4 and, (b), its STFT. (c) Strain record for test 15 on specimen T-1 and, (d), relative STFT. (e) Strain record for test 15 on specimen T-5 and, (f), corresponding STFT. (g) Strain record for test 18 on specimen T-6 and, (h), its STFT.*

the excitation is switched off, in this test-case, other frequencies seem to enrich the strain spectrum: these components are the sub-harmonics at 1/3 of the driving frequency and some of its multiples. The spectrogram in Figure 5.6 (f) is richer compared to the case of Figure 5.6 (d). Frequencies above 200 kHz are excited, although most energy is concentrated in the range between approximately 13 and 133 kHz (1/3 to 10/3 of the driving frequency) with the largest strain amplitudes seemingly concentrated at 13 kHz, 40 kHz, 80 kHz and 106 kHz (1/3, 1, 2 and 8/3 the driving frequency). After an initial interval during which the vibration seems to be unstable (until around 0.25 seconds), the strain settles to a nearly constant amplitude and frequency content before the excitation is interrupted around 0.7 seconds. The last test [Figure 5.6 (h)] presents an extremely rich spectrum, again with frequency components in excess of 200 kHz excited. Most of the vibrational energy is however concentrated in the band between 13 kHz and 173 kHz (1/3 to 13/3 of the center frequency). As seen for the former case, the vibration tends to stabilize after an initial unstable phase near the start of the excitation. Interestingly, the white tracks that represent the amplitudes of the frequency components of the strain spectrum are generally wider in this test than for the three cases previously analyzed; at around 0.4 and 0.7 seconds (immediately before the excitation terminates) a relatively continuous band of frequencies between 13 kHz and 40 kHz seems to be excited. This situation is similar to the acoustic chaos recently reported by Favro et al. [87].

5.3 Crack damping as input in the prediction procedure

The damping measurements described in section 3.3.3, obtained by the controlled excitation of a single low-frequency flexural mode of the beams T-1, T-2, etc. of Table 2.2, could be used to estimate the damping of the crack in any odd flexural mode using the assumption validated in section 3.3.2 that, at a given strain level, the energy loss per cycle is independent of frequency. Thus, the calculation of the total

energy released by the crack after each thermosonic excitation pulse could be done in the time domain by considering the sum of the contributions during each vibration cycle undergone by the crack. The value of η to be used in such computations was derived from the curves of Figure 3.8, which express its strain dependence (this loss factor will be called $\eta_{crack,3}$ i.e. the extra loss factor due to the crack and which was previously measured at high strain in the 3rd flexural mode). Since these curves were measured by exciting mode 3 of the beams, the strain energy in this mode V_3 was used for the calculation of the heat dissipated by the crack ΔV_i during each cycle i:

$$\Delta V_i = 2\pi\eta_{crack,3}(\epsilon_i)V_3(\epsilon_i). \tag{5.1}$$

The energy stored by the beams in the 3rd flexural mode was previously obtained from the eigenvalue finite-element analysis (FEA) of an uncracked beam (see Table 3.2 in Chapter 3).

A summary of all tasks involved in the prediction process is shown in Figure 5.7. It comprises experimental, FEA and postprocessing steps. The calculation of the heat released at the crack versus time is possible after the extra damping due to the crack has been characterized at realistic vibration amplitudes (first horizontal branch of the flow-chart of Figure 5.7). The vibrations of the beams will be analyzed in the time domain, decomposing the strain records into individual vibration cycles and calculating for each one of these the rms strain amplitude. Next, the function $\eta(\epsilon)$ measured in Figure 3.8 will be used to retrieve the appropriate value of ΔV according to equation 5.1. This is shown by the second horizontal branch of Figure 5.7 which merges with the first one at node 1. When the strain in the thermosonic test exceeded the maximum strain excited in the damping measurements, the value of ΔV for the maximum available strain was used for higher strain levels. The work illustrated by the third horizontal line was necessary to model the crack as a non-uniform heat source, and combines with the rest of the work-flow at node 2. The resulting temperature increase at the monitoring surface (over the crack width) can be obtained at this point using an analytical thermal model of the specimens (this will be presented in detail in section 5.4). The predicted temperature rise will

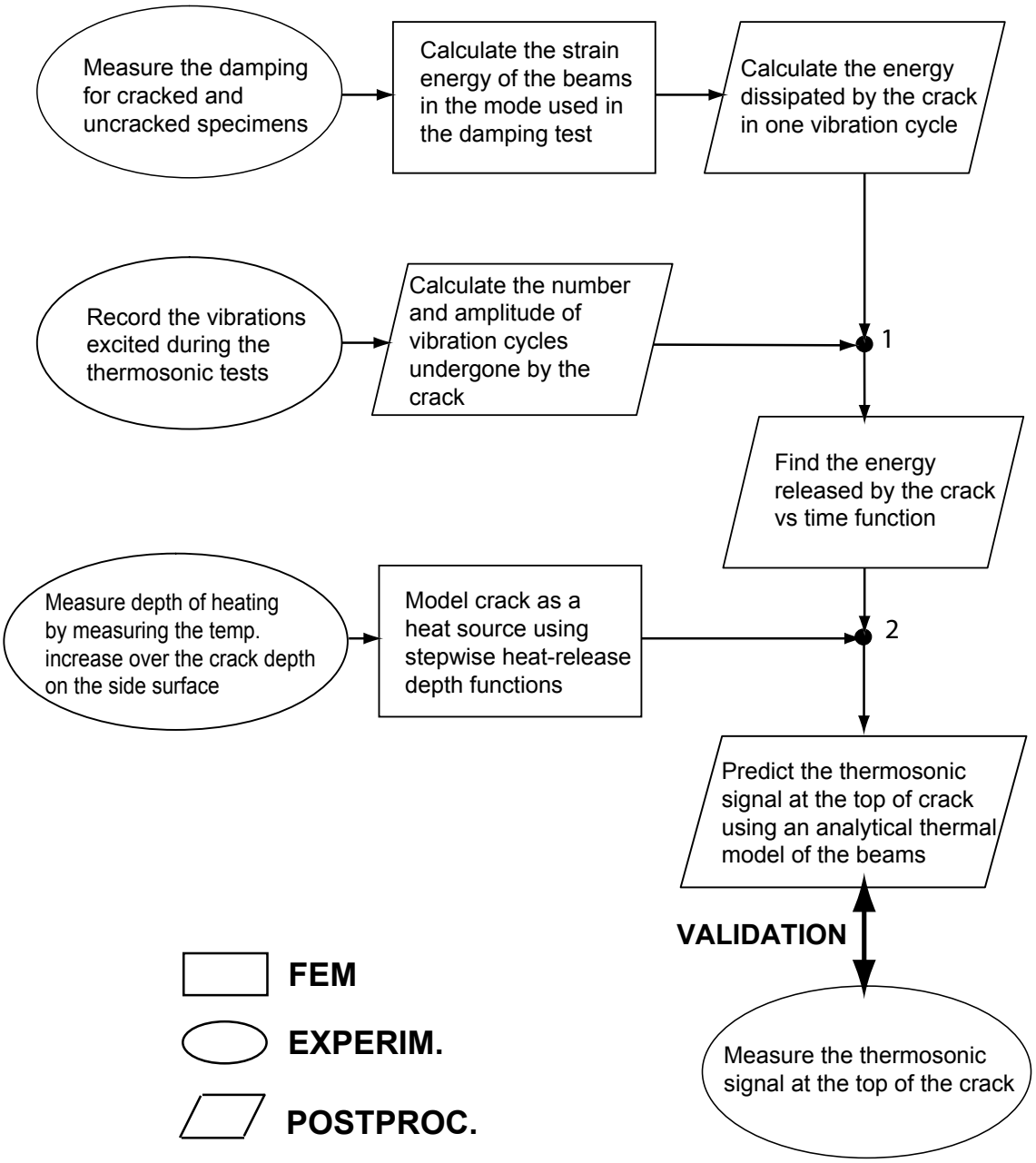

Figure 5.7: *Block diagram representing the tasks involved in the prediction of the thermosonic signal.*

eventually have to be compared to the experimental temperature increase measured by the IR camera during each test in order to validate the prediction algorithm. The modelling of the crack as a heat source constitutes an extra preliminary stage of work, in addition to the measurement of the crack damping carried out in Chapter 3. These two preliminary steps are both required before the calculation of the predicted

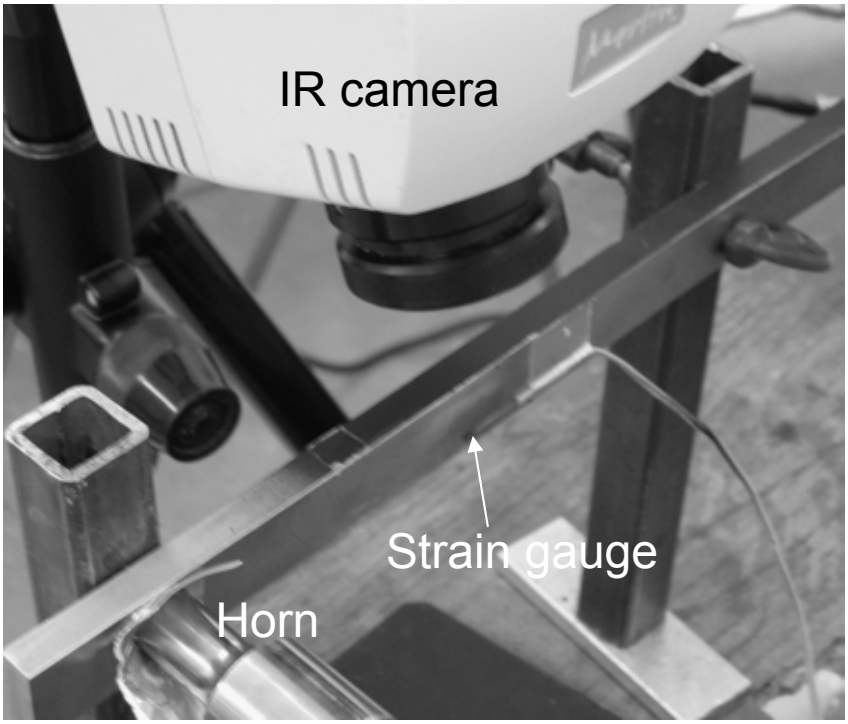

Figure 5.8: *Thermosonics testing configuration with the IR camera pointed towards the thinner dimension of the cross section of the beams (the crack is said to be seen from the "side"). This configuration (with the camera rotated of 90 degrees with respect to the configuration of Figure 5.5) was used to estimate the distribution of heat vs depth.*

temperature rise can be carried out for each test.

5.3.1 Estimate of heating distribution

As mentioned in the Introduction of this Thesis, the thermal models used to achieve the prediction of the thermosonic signal were developed by Tim Barden; however they are described here for completeness. Simple models of heating at the crack tip only (uniform linear heat source) and uniform heating over the crack sides (uniform rectangular heat source) are not realistic, given the complexity of the crack morphology (described in section 2.3). In particular, since the cracks considered in this study "breathe" under the action of flexural vibrations, it could be expected that heat will be released at the crack tip (in the plastic stress concentration zone) as well as over

the crack interfaces due to friction during contact of the interfaces. An accurate characterization of where the heat was dissipated over the crack faces would have required an in-depth study of the crack microscopic features (size and distribution of the asperities, size and shape of the plastic zone, characterization of the crack mouth and tip displacements etc.). For this reason some simplifications were made. Since the largest dimension of the cracks is their width across the specimens, and because the cracks mainly vibrated in their opening mode, the heat dissipation was assumed to be uniform in the transversal direction of the beams. However, it was assumed that the heat could be generated in different amounts at different depths. The cracks were modelled as rectangular heat sources with non-uniform power over their depth. In order to enable the use of a simple analytical model of heat propagation, the crack was divided into a number n of uniform-power rectangular layers over its depth. The crack spatial heat distribution function was therefore a stepwise function of the crack depth. The stepwise functions (one for each crack) were found on the basis of the temperature rise measured at the crack side (Figure 5.8) at the onset of the vibration, when the effects of heat diffusion were negligible. The temperature measurements using the setup of Figure 5.8 were taken a few times for each cracked beam. All the other tests involved measuring the temperature rise at the top of the cracks across their width (standard testing configuration of Figure 5.5) for the validation of the prediction method. An example of temperature rise vs crack depth for the crack of specimen T-5 is provided by the solid line in Figure 5.9 (a). This measurement was done in a test with vibration amplitudes similar to those normally reached during the previous tests with the camera focused on the top of the crack. The measured temperature profile over the crack side was fitted by one obtained via finite-element (FE) simulations. A three-dimensional thermal FE model of the beams was used for this purpose. An iterative trial-and-error analysis was carried out. Initially, an arbitrary heat-release step function was assumed to model the crack. The results of the FE thermal analysis produced a corresponding temperature profile on the crack side. Based on this, a new heat-release step function was defined and then updated iteratively until a FE temperature profile along the crack side nearly matching that seen experimentally was achieved. For the crack

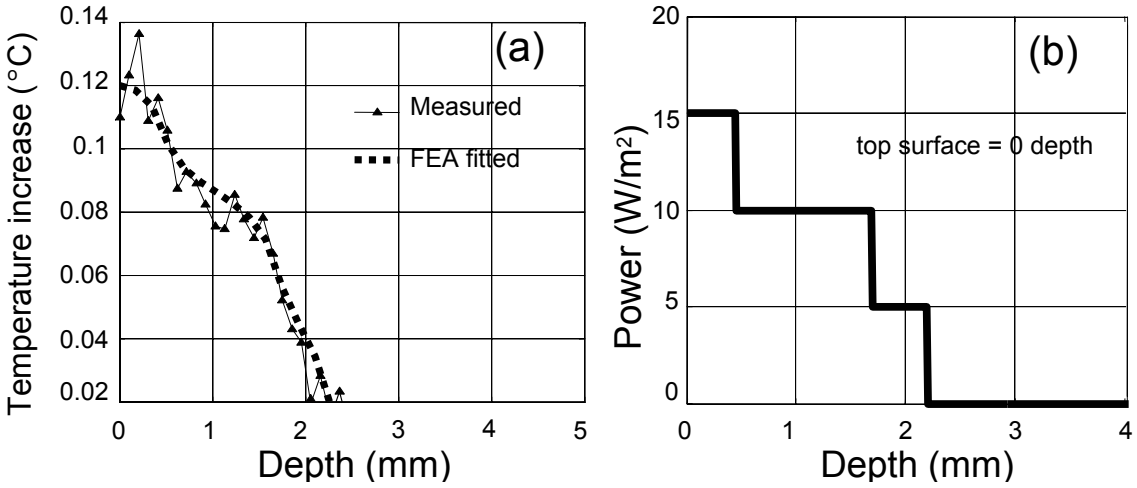

Figure 5.9: *Estimation of the heating distribution over the crack depth. (a) Measured temperature over the crack size for specimen T-5 and matching curve-fitted temperature profile obtained by finite-element analysis (the y-axis origin is set to 0.02 °C as this was the IR camera noise level for these measurements). (b) Corresponding heat-release step function modelling the crack as three uniform power rectangular heat sources embedded at increasing depth.*

in specimen T-5, a good fit was obtained assuming a 3-step function [see Figure 5.9 (b)]. The fitting FE temperature profile, obtained using the heat-release profile of Figure 5.9 (b), is shown in Figure 5.9 (a) by the dotted line. Table 5.9 summarizes all the heat-release step functions that were used to model each crack. The heat dissipation is given in percentage over the crack depth. For the biggest crack (specimen T-1) it was necessary to use four segments, whereas two segments were enough for the smallest crack of this batch of specimens (specimen T-4). For the cracks in beams T-1 and T-6, no dissipation was assigned to one intermediate segment. This may appear unlikely, but it can be explained by an internal concavity of the crack and therefore can be the result of the crack morphology. From Table 5.1 it can also be seen that in most cases the thermal depth of the defect was slightly smaller than the observed crack depth at either side (refer to Table 2.3), meaning that a negligible fraction of the heat was coming from the crack tip and the plastic zone around it. In contrast, a significant fraction of heat was often released close to the surface of the specimens. The average roughness of the crack surfaces (see section 2.3.3) was around 6-7 μm, and was thus comparable with the average crack-mouth opening

Table 5.1: *Step-functions used to describe the distribution of the heating (given as the percentage of the total power, P_n) over the segments (d_n) of the crack.*

Crack	T-1	T-2	T-3	T-4	T-5	T-6	T-7
d_1 (mm)	0-0.2	0-0.2	0-0.25	0-0.25	0-0.45	0-0.2	0-0.25
P_1 (%)	55	64	59	50	50	53	8
d_2 (mm)	0.2-0.4	0.2-0.75	0.25-0.9	0.25-0.45	0.45-1.7	0.2-0.65	0.25-1.25
P_2 (%)	41	3	24	50	33	0	69
d_3 (mm)	0.4-2.5	0.75-1.7	0.9-1.4	-	1.7-2.2	0.65-1.7	1.25-1.6
P_3 (%)	0	33	17	-	17	47	23
d_4 (mm)	2.5-3.5	-	-	-	-	-	-
P_4 (%)	4	-	-	-	-	-	-

displacement (CMOD) for all specimens as discussed in section 2.3.1. Therefore, contact between crack asperities (hence friction) could occur over the whole cracked area up to the crack mouth. At certain locations along some of the cracks, CMODs of up to 10 μm were observed, but even in this case friction at the asperities could occur since the average roughness was measured along 15 mm across the crack near the top surface and peaks of asperities as high as 20-30 μm above the roughness zero line were observed to be regularly present along the crack width in all specimens.

5.4 Predictions

One vibration cycle was defined by three consecutive "zero crossings" of the recorded vibrational strain with the two halves of the cycle having strain of opposite sign [as shown in the inserts a/1) and a/2) in Figure 5.10 (a)]. The heat liberated by the crack in one cycle was calculated using equation 5.1 and then averaged within time windows of 6 ms (corresponding to approximately 240 cycles at the fundamental

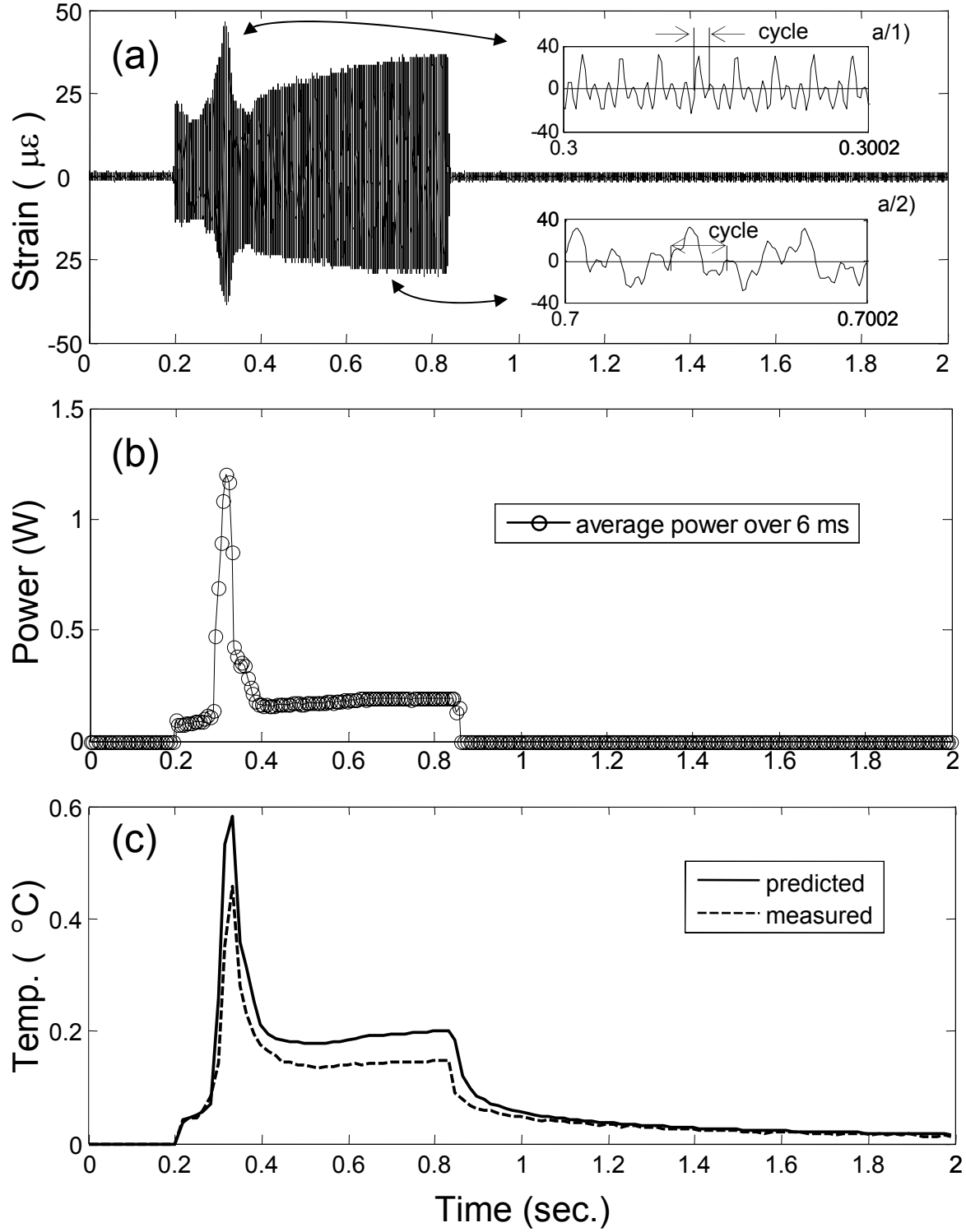

Figure 5.10: *(a) Strain record for test 5 on specimen T-1; the inserts a/1) and a/2) show different instantaneous vibration regimes within the pulse. (b) Average power generated at the crack plotted vs time during the excitation. (c) Prediction and measurement of the average temperature rise on the top of the crack.*

excitation frequency of 40 kHz) to obtain the power $P_{crack}(t)$ as:

$$P_{crack}(t) = \frac{\sum_{i=1}^{n} \Delta V_i}{\Delta t} \tag{5.2}$$

where n is the number of cycles undergone by the crack in the chosen time step Δt of 6 ms. An example of the variation of $P_{crack}(t)$ over the duration of the test is plotted in Figure 5.10 (b) for specimen T-1, test 5. The heat released globally by the crack was calculated in this way as a function of time during the excitation in each test and the heat released as a function of depth was obtained as described in section 5.3.1. The heat-release-vs-depth functions actually used for the predictions have to express the fraction of the total instantaneous heat generated which is being released at a certain depth. For this reason the heat-distribution step functions used in the predictions were expressed as percentages in Table 5.1. For example, specimen T-2 had the crack which released most heat close to the top surface, whereas for the crack of specimen T-6 a large fraction of the heat was released at approximately mid-way from the surface to the root of the crack.

The temperature rise on the monitoring surface of the specimens (top of crack) could be predicted on the basis of the model of the crack as a heat source described in the previous section, using the principle of superposition. Since the crack was described as a finite number of rectangular sources of uniform power embedded in the beam at different depths over the cracked cross section, the temperature rise at the top of crack was the sum of the temperature rises caused by each rectangle separately. The problem of finding the surface temperature rise when a rectangular heat source is embedded in the material can be solved numerically and has been already used in thermosonics [92]. In this work (this part was carried out by Tim Barden, responsible for thermal modelling for the project), adiabatic conditions at the surfaces were used and no lateral heat flow (no edge effects, equivalent to using a two-dimensional heat propagation model) was also assumed, given the geometry of the cracked specimens. The temperature solution $T(t)$ on the top of the crack for pulsed heating from a series of n uniform rectangular sources of powers P_h embedded in a medium was numerically derived by integrating the solution for a line source

over the height of the rectangles d_h [93]:

$$T(t) = \sum_{h=1}^{n} \{ -\frac{P_h}{4\pi\kappa d_h} \int_0^{d_h} Ei(-\frac{z^2}{4\kappa t}) dz \} \quad with \quad -Ei(-x) = \int_x^{\infty} \frac{e^{-u}}{u} du \quad (5.3)$$

where κ is the thermal diffusivity of the homogeneous and isotropic material and z is the coordinate of the thickness direction of the beams.

The predicted thermosonic signal is shown in Figure 5.10 (c). Since edge effects at the crack corners were not considered, the predicted temperature rise is uniform over the width of the beams. This can be compared to the temperature measured by the IR camera during the same test [shown by the dotted line in Figure 5.10 (c)]. For such comparisons, the average experimental thermosonic signal from all camera pixels over the crack width was considered (around 140). This had to be done because of the non-uniform temperature distribution measured on top of the crack, which was a consequence of the non-uniformity of the crack over its width as well as the presence of edge effects etc. An example thermal measurement with the IR camera in the configuration of Figure 5.5 is given in Figure 5.11 (a). This IR image is taken from the acquisition sequence at the instant of maximum (space) average temperature rise. The temperature rise measured at the edges is slightly different that at the center of the crack; this is a combination of edge effects in the heat propagation as well as possible local anomalies in the crack morphology. The temperature rise versus the width of crack is plotted in Figure 5.11 (b) together with the average level and plus/minus one standard deviation boundaries to give an estimate of the non-uniformity of the temperature profile.

The analysis of the results obtained in this Chapter can now be divided into two distinct parts. First, it is necessary to validate the prediction procedure by systematically comparing the predictions with the measurements. Second, an analysis of the sensitivity of thermosonics with respect to crack size can be carried out since cracks of different size were tested.

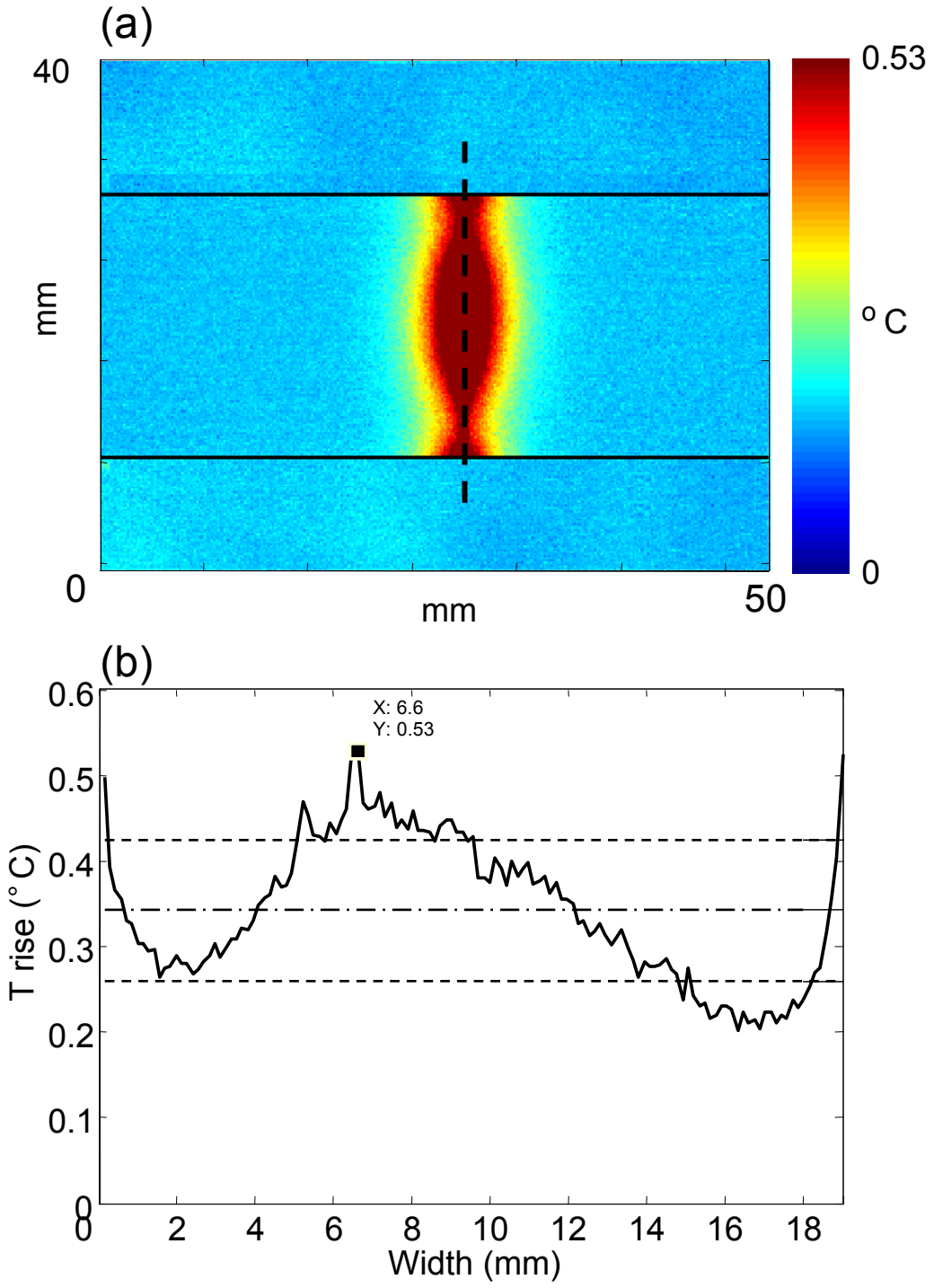

Figure 5.11: *Example of thermal measurement across the crack ("top" view as in Figure 5.5). (a) IR camera image during test 13 on specimen T-5 at the instant of maximum average temperature rise across the crack width. The dashed line indicates the line of pixels considered for spatial averaging. (b) Temperature rise across crack width (solid line, the cursor shows the X and Y values in the graph for the point of maximum), average temperature rise (dash-dot line) and plus/minus one standard deviation (dashed lines).*

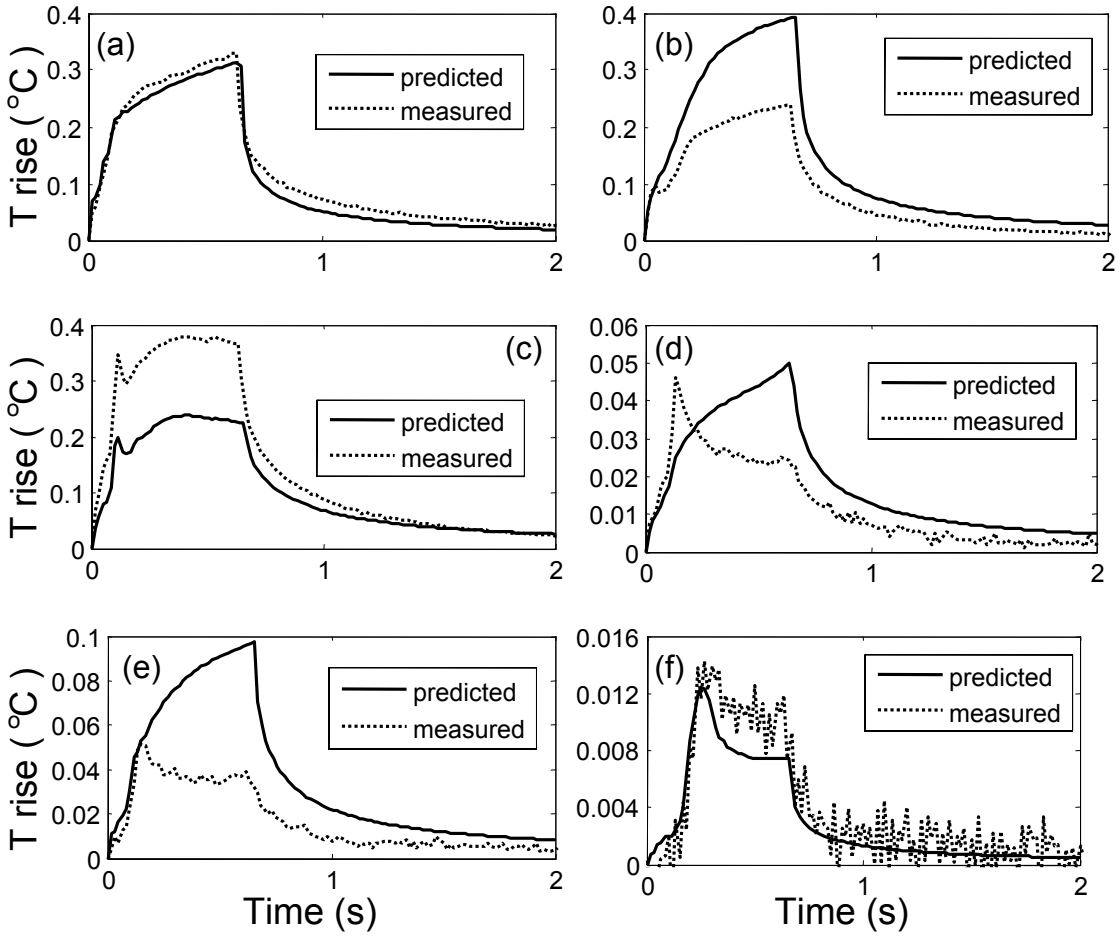

Figure 5.12: *Examples of comparisons between measured and predicted thermosonic signals from different tests in different specimens: all significant cases are encompassed, from excellent agreement as in (a) (specimen T-1, test 16) to the worst obtained correlation in (e) (test 18 for specimen T-2), including the case (f) of barely measurable temperature rise (specimen T-4, test 7) and intermediate cases such as (b) overestimate (specimen T-3, test 15), (c) underestimate (specimen T-6, test 17) of the thermosonic signal from predictions and (d) disagreement in the shape of the transient (specimen T-7, test 9).*

5.5 Validation against measurements

Six examples to illustrate the different degree of agreement between predictions and measurements obtained in a total of 116 tests on 7 cracked specimens are shown in Figure 5.12. These tests represent all the relevant cases, and will be used later to divide the total number of tests into six distinct categories. In Figure 5.12 (a) the prediction showed good agreement with the measurement, both in terms of

maximum temperature rise and the shape of the transient thermosonic signal (rise and fall of temperature). In Figure 5.12 (b) the shape of the predicted thermosonic signal was the same as the measured one, but the two curves differed by a factor of about 2 with the prediction overestimating the magnitude of the measured signal. In contrast, for the case shown in Figure 5.12 (c) the prediction underestimated the measured temperature rise, although there was still agreement in the shape. In Figure 5.12 (d) the shapes of the measured and predicted thermosonic signals were different even though the maximum temperature rise was of the same magnitude. The test in Figure 5.12 (e) was the worst case out of all tests: the shape of the transient temperature rise and fall was different and the discrepancy between the maximum temperatures reached in the test was the largest (around a factor of 2). The case shown in Figure 5.12 (f) was also of interest because the temperature rise was barely measurable using the IR camera (Cedip Jade, which allowed a noise floor of just under 0.01 $^{\circ}C$ with background subtraction), although there was general agreement in terms of shape and magnitude between prediction and measurement. From the strain record for this test, it could be argued that the threshold strain for crack detection was, for the crack in specimen T-4, in the region of 15 $\mu\varepsilon$ peak. Six categories, encompassing all possible outcomes from all the tests, were defined according to Figure 5.12 and labeled from (a) to (f). The variability of the magnitude and shape of the predicted and measured temperature rise among different tests carried out on different specimens (shown in Figure 5.12) was caused by inevitable differences in the coupling and loading conditions of the exciter against the specimens as well as by changing clamping conditions of the specimens against the supports.

5.5.1 Accuracy of predictions

An estimate of the average agreement between predictions and measurements could be obtained by plotting the average measured and predicted thermosonic signals (during temperature rise and fall, over a period of approximately 2 seconds) against each other, as illustrated in Figure 5.13. The criterion of comparing predictions and measurements by looking at the average temperature increase was chosen for

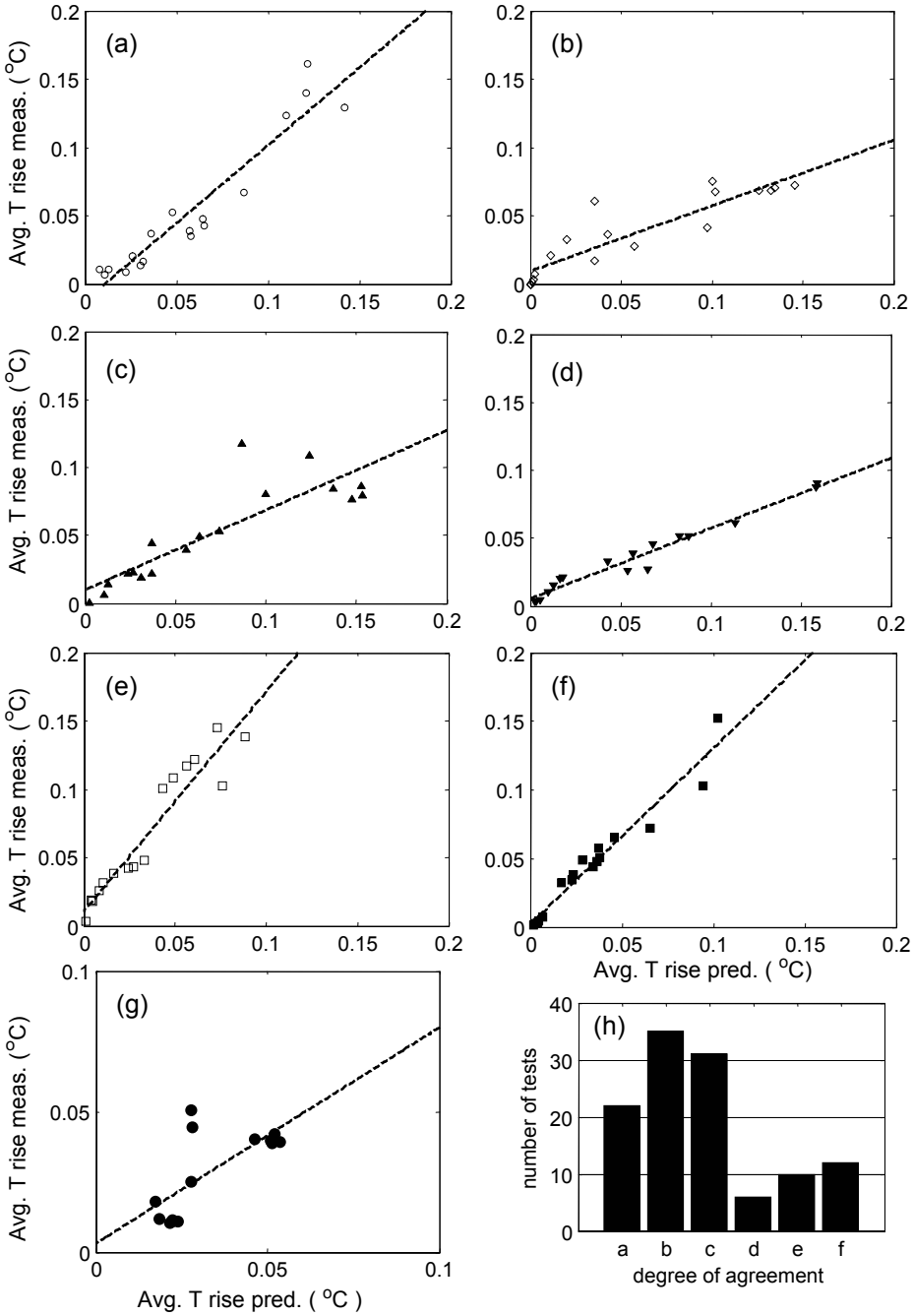

Figure 5.13: *Average magnitude of the measured thermosonic signal vs average magnitude of the predicted thermosonic signal for all tests in all specimens. (a) Specimen T-1; (b) specimen T-2; (c) specimen T-3; (d) specimen T-4; (e) specimen T-5; (f) specimen T-6; (g) specimen T-7. The dotted line is the linear fit. The histogram (h) represents the distribution of the 116 tests in the 6 categories defined in Figure 5.12.*

Table 5.2: *Summary of the number of tests carried out for each specimen, the slope of the lines fitted to the predicted vs measured temperature rises and the average variability of the temperature across the width of each crack expressed as the standard deviation (sd) divided by the mean value (T_a).*

Specimen	T-1	T-2	T-3	T-4	T-5	T-6	T-7
Tests available	18	16	17	17	16	18	14
Slope	1.1	0.45	0.59	0.53	1.6	1.3	0.77
$\overline{(\frac{sd}{T_a})}$ (%)	52	33	26	41	37	27	27

practical reasons: analyzing the detectability of the cracks by finding a relationship between vibration input and the temperature rise. Since the crack signature temperature rise was measurable during the whole time that the temperature was higher than the base background level, an appropriate period was about 2 seconds as indicated from Figure 5.12. From Figure 5.13 (a) to (g) it can be seen that perfect agreement was not always obtained, as this would have been equivalent to the measured points lying all on the line with unit slope. However, the predictions show a clear linear trend with the measurements, with the least square line having different slopes for different specimens. The slopes of the fitted lines are reported in Table 5.2. For slopes greater than unity the predictions tended to overestimate the measurements and viceversa. In the case of specimen T-1 a fitted line with a slope very close to unity was obtained. The worst case is specimen T-2.

The scatter of the data was due to the general level of accuracy of the prediction methodology. The cracks had a rather complex morphology as documented in section 2.3, but were modelled using multiple rectangular uniform heat sources as described in section 5.3.1). The measured temperature rise was the average over a straight line of pixels approximately covering the crack mouth, even though the cracks often had an irregular shape. Furthermore, during the excitation pulse, micro slipping of the specimens in their supports could occur, hence producing a small offset of the array of monitoring pixels with respect to the crack location. The tem-

perature was measured over approximately 140 pixels covering the crack width and its variability was quantified by the ratio between the standard deviation (σ) and the mean value (m). The average value of this ratio (expressed as a percentage) for all tests available for each specimen is reported in Table 5.2. The lowest average temperature variability across the width was measured for specimen T-3 (around 26%) whereas the highest was recorded for specimen T-1 (around 52%). These values did not correlate with the average scatter for each specimen shown in Figure 5.13 (a) to (g). We also considered each test individually to see whether the tests which showed worst agreement [Figures 5.12 (d) and (e)] had the largest temperature variability across the specimen width, but it was not possible to find a correlation. However, there are several other possible reasons for the scatter in the measurements versus predictions plots. For example, several approximations were used when considering the damping data (section 3.3.3). Measurements of η were only available up to 30 $\mu\epsilon$ even though in most tests amplitudes of 40 - 60 $\mu\epsilon$ were excited. In addition the energy dissipated per cycle at a given strain level was assumed to be completely independent of frequency, a good-enough first approximation which however did not perfectly match the experimental data. The histogram in Figure 5.13 summarizes the level of agreement for all tests according to the classification introduced earlier in Figure 5.12, with categories from "a" to "f". The tests falling in category "e" (discrepancy both in magnitude and shape) were less than 10% of the total number of tests. Most tests (88 out of 116) fell in categories "a" to "c", meaning that the shape of the predicted and measured signals was usually the same. For 34 out of 116 tests (22 for column "a" and 12 for column "e", a total of about 33% of the total tests) the level of agreement was good, with a discrepancy between the average predicted and measured thermosonic signals within 20%.

5.6 Analysis of sensitivity to crack size

The second step of the analysis of the results is a sensitivity study to find, if possible, the minimum detectable crack size using this implementation of the thermosonic method and the current specimens. The amplitude and frequency content of the

strain record for each test was non-stationary, hence we computed the rms value of the strain during the whole duration of each pulse (ϵ_{rms}) as the quantity to represent the intensity of vibration. The average temperature rise T_{avg} over the duration of each pulse was also computed. In Figure 5.14 (a) the ratio T_{avg}/ϵ_{rms}^2 (the heat generated is proportional to ϵ^2), averaged among all tests available for each specimen, is plotted versus the percentage cracked area for each specimen. This ratio clearly increases with increasing crack size, although there is considerable scatter in the data. It is believed that the scatter is related (1) to the different levels of initial crack partial opening which could affect the magnitude of the thermosonic signals for any given crack size and (2) to the non-uniform shape of the cracks across the width and through the depth of the specimens. A least square linear fit is also shown in Figure 5.14 (a), and it can be seen that it does not intercept the x-axis near the origin. This is not physically possible, as virtually no temperature increase must correspond to the absence of a defect (an extremely small temperature rise would in theory be possible in the absence of a defect due to internal damping, but this was never measurable in our experiments). In fact the relationship between temperature rise and crack size is likely to be nonlinear [17]. A study of the relationship between defect size and temperature rise for smaller cracks, which are of most interest in practice, is now needed.

5.6.1 Thermosonic efficiency vs damping efficiency

Figure 5.14 (b) shows the relationship between the average crack-related loss factor from Figure 5.14 and the crack size. Unsurprisingly the trend is very similar to that of Figure 5.14 (a) since the increase in loss factor is what produces the temperature rise. The good correlation between the capability of the cracks to generate a thermosonic signal and to absorb mechanical vibrations is shown in Figure 5.14 (c) where the average temperature rise per unit strain squared is plotted directly against the crack loss factor.

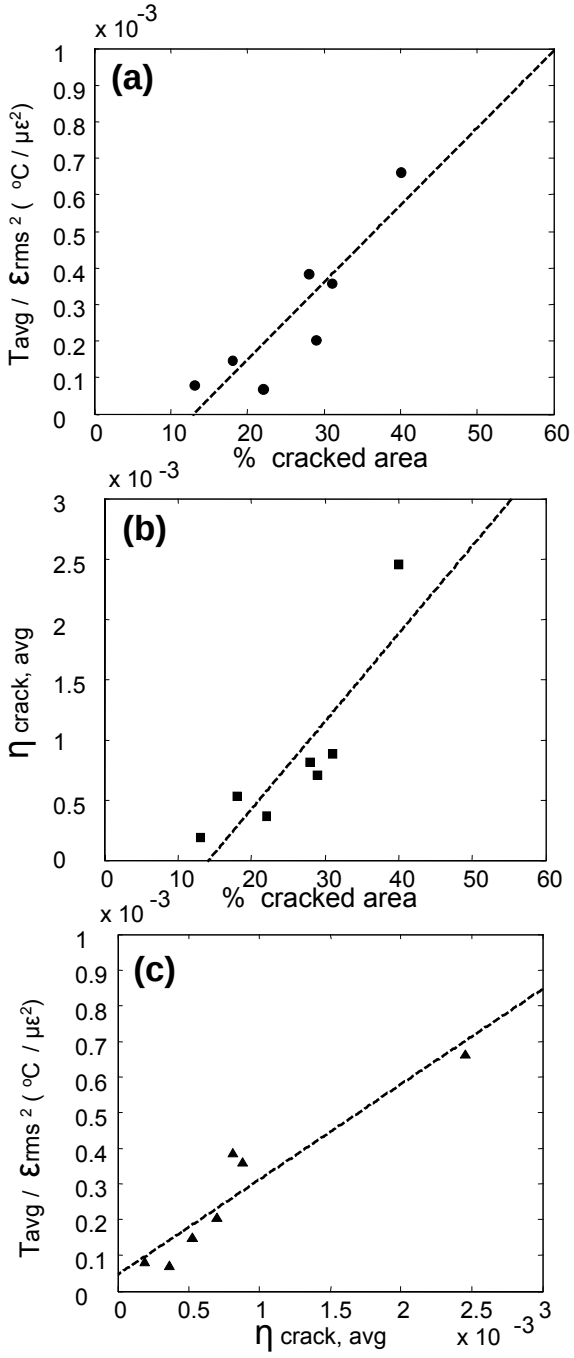

Figure 5.14: *(a) Measured average temperature rise per unit strain squared plotted vs percentage of cracked cross section. (b) Crack loss factor vs percentage of cracked cross section. (c) Measured average temperature rise per unit strain squared plotted vs crack loss factor for each specimen. The dashed lines represent the linear fit.*

5.7 Review of Chapter

The purpose of this Chapter was to establish a quantitative link between vibration amplitude and thermal response measured during thermosonics testing of metal samples with fatigue cracks. The prediction of the temperature rise near the crack was achieved on the basis of the independent measurements of the additional crack damping presented in Chapter 3. This approach has the advantage of globally evaluating the extra losses at the crack and assumes such extra losses to be responsible for the local temperature increase. The thermosonic signal could be predicted by measuring the amplitude of the excited vibrations, even though variable and uncontrolled coupling conditions between the horn and the specimens were responsible for the excitation of complex vibrations. A clear linear correlation between the predicted and measured average thermosonic signal was found. The deviation of the line from perfect agreement observed in some specimens is likely to be mainly due to the complexity of the crack morphology (hence the presence of three-dimensional effects) and to the difficulty of measuring the crack damping up to the amplitudes excited in the thermosonics tests. After having established a methodology which produces a quantitative link between vibration strain, damping and thermosonic signal, the next task will be to test smaller cracks and derive a criterion for their detectability.

Chapter 6

Reliable crack detection using thermosonics

6.1 Introduction

Thermosonics is a potentially attractive NDT tool which could soon find application in industry for fast screening of structures. The method is intrinsically rapid and the pass/fail response after each test could be fully automated to be independent of human judgement. Major costs arising from the purchase of IR equipment will decrease as new higher sensitivity cameras will enter the market. The crucial issue for thermosonics to become a routine NDT method in industry is *reliability*. The work described in Chapter 5 sets the necessary background to advance into this further field of investigation. The local temperature rise exploited by thermosonics was linked to the energy dissipation occurring at the crack through information on the crack extra damping. The heat generated at the crack after one vibration cycle is a fraction of the total strain energy stored in a beam vibrating at a given amplitude. Higher vibration amplitudes mean that more energy will be transformed into heat and are therefore desirable in thermosonics testing (so long as the excitation does not cause further propagation of the crack). On the other hand, higher vibration frequencies are also beneficial since the heat liberated by the crack per unit time will

be proportional to frequency for a fixed strain amplitude. Thus, reliable detection of cracks in thermosonics will involve the determination of the minimum amplitude, frequency, or combination of these two parameters, required to detect cracks of practical interest in industry.

In Chapter 5, a total of 116 tests on seven 10-mm-thick beams with cracks varying from 13% to 40% of the total cross section were recorded and then post-processed. The presence of a crack at mid-span was detected rather easily in all tests. The lowest strain amplitude excited by the setup of Figure 5.5 was sufficient to generate an easily measurable temperature rise on the smallest crack. Let us consider the test of Figure 5.12 (f), where a maximum strain of around 15 $\mu\epsilon$ was measured. This case (test 7 for specimen T-4) has been previously described as "barely measurable temperature rise" which is correct in comparison to temperature rises typically obtained in other higher strain tests, carried out on the same specimen, or on other specimens with larger cracks. In this test, a temperature rise was measured for the whole duration of the excitation pulse (the maximum temperature rise observed, T_{max}, was around 0.014 $^{\circ}C$), and was followed by the usual decay once the excitation was switched off. An estimate of the noise level (NL) for this measurement is the maximum temperature measured by the IR camera in the absence of ultrasonic stimulation. According to this definition, a noise level of approximately 0.004 $^{\circ}C$ can be estimated from Figure 5.12 (f). The noise level of a typical thermosonic thermal measurement is a function of the camera sensitivity as well as the spatial averaging which is used to obtain the average temperature rise on the crack (this will be discussed later in section 6.4). The signal-to-noise ratio (SNR) is calculated for this test-case as:

$$SNR = \frac{T_{max}}{NL} = \frac{14}{4} = 3.5 \simeq 11dB \tag{6.1}$$

which is adequate for the signal to be clearly observed. A study of the minimum strain required to reliably detect this 13%-of-cross-section crack, would have required the excitation of strain amplitudes lower than 15 $\mu\epsilon$. Unfortunately, this could not be achieved consistently using the excitation setup of Figure 5.5 for the 10-mm-thick beams. This is essentially due to the fact that the exciter is a fixed displacement and fixed frequency device, designed to operate within a given range of loading force

and therefore within given boundaries of power absorption. If the conditions of such an operation range are not satisfied, a cut-off circuit is programmed to interrupt the electrical input to the exciter (refer to Chapter 5, section 5.2.1).

A viable method of carrying out a study on the vibration threshold needed to detect small cracks using the same excitation setup, is to test a set of thicker beams with cracks of size approximately 10% or lower of the cross section. In this way, less flexible beams coupled to the same excitation system ensure the possibility to investigate the threshold between detectable and non-detectable crack sizes. Furthermore, for a given crack size, tests falling on either side of the vibration threshold could be recorded and analyzed to determine this vibration limit as accurately as possible. The cracked beams described in Table 2.3 in Chapter 2 were specifically prepared for this purpose. The steps involved in the definition of a testing procedure able to ensure reliable detection of cracks using thermosonics can be summarized as follows:

1. determine a function of strain amplitude and frequency to be used as a reference parameter to be monitored throughout the study; ideally, this function will be able to provide an estimate of the temperature rise to be expected on the crack from the post-processing of the strain record in each test;

2. test the new set of cracked specimens to measure the threshold value of this new parameter (i.e. the value necessary to detect each crack clearly);

3. calibrate the monitoring parameter against the actual temperature rise measured in each test;

4. use the results of points 2 and 3 to prescribe a testing procedure to be used in real thermosonic inspection to detect cracks reliably.

6.2 Frequency domain post-processing of thermosonic tests

The crack extra-damping for this new set of specimens was measured in mode 3 at strains comparable to those normally excited in the thermosonic tests. The results are illustrated in Figure 3.9 (Chapter 3). If we consider these results and those of Figure 3.8, it can be observed that virtually constant crack damping as a function of amplitude was obtained for the two smallest cracks in the specimens tested in Chapter 5, specimens T-4 and T-7, as well as for all the new specimens (TT-1 to TT-7). It has already been shown (see section 2.3.1) that the degree of opening of the crack can influence the actual contact area between the crack interfaces. In light of this effect, the concept of "effective" crack size was introduced to interpret certain VAM results (see Chapter 4, section 4.6). The effective crack size is determined by the gross crack size, the amplitude of vibration and the microscopic morphology of the defect (e.g. asperities, plastic region around crack tip, condition of pre-stress across the crack, etc.). This particularly applies to large cracks, such as those in specimens T-1 and T-5, which have a reduced contact area as the amplitude of vibration increases; hence the dissipation of energy per unit cycle decreases. Other specimens which show an increase of loss factor with amplitude, for example T-2, T-3 and T-6, exhibit this distinctive feature if the degree of engagement of the crack asperities increases at higher amplitudes with no change of the effective crack area. However, smaller cracks (with size below 20% of the total cross section), vibrating within this range of amplitudes, seem to be rather immune to such an evident nonlinear damping behaviour. For small cracks, it seems reasonable to assume that the crack damping can be approximately modelled using a single constant loss factor value, η, at any given amplitude and frequency. This is equivalent to considering the crack as an extra source of linear damping in the system.

The immediate implication of this assumption is that the computation of the power dissipated at the crack during a thermosonic test can also be carried out in the frequency domain, with reasonable accuracy, rather than only in the time domain

Table 6.1: *Results from the finite-element modal analysis of the beams TT-1 to TT-7 of Table 2.3.*

Flexural mode N	Natural frequency f_N (Hz)	Back-face strain $\epsilon_{fe,N}$ ($\times 10^6 \mu\epsilon$)
1	996	3.80
3	5127	16.8
5	11759	37.6
7	20039	61.7
9	29324	87.3
11	39192	113
13	49373	139
15	59693	164
17	70020	188
19	80212	210
21	89954	224

(as described in Chapter 5) since for a linear system (or reasonably assumed so) the principle of superposition is valid. This allows the decomposition of the specimen's vibration into its individual frequency components and, hence, the calculation of the strain energy carried by the beam at each frequency from the knowledge of the mode shapes (see equation 6.3 and Table 6.1). The crack loss factor is used to calculate the energy dissipated by the crack when vibrating in that mode using equation 3.13 (Chapter 3). This algorithm needs to be implemented in short-time Fourier transform mode due to the non-stationary nature of a typical thermosonic test (see for example Figure 5.6 in Chapter 5). The contributions from all modes can be summed according to the principle of superposition to obtain:

$$P(t) = 2\pi\eta_{crack} \sum_N f_N V_N, \tag{6.2}$$

$$V_N = (\frac{\frac{1}{2}\omega_N^2}{\epsilon_{fe,N}^2})\epsilon_{exp,N}^2 = C_N \epsilon_{exp,N}^2, \tag{6.3}$$

where the strain energy per unit strain squared, C_N, is calculated numerically from

the eigenvalue finite-element analysis of the beams, in the same way as described in section 3.3.2. If the eigenvectors are mass-normalized, the strain energy is given by half the eigenvalue ($\frac{1}{2}\omega_N^2$), $\epsilon_{fe,N}$ is the back-face strain of the mode N in this mass-normalized configuration computed from the finite-element analysis (FEA), and $\epsilon_{exp,N}$ is the actual measured strain of the frequency component f_N. The values of f_N and $\epsilon_{fe,N}$ obtained from FEA of the new beams are given in Table 6.1. Only odd flexural modes of the beams (up to around the cross-sectional cut-off frequency) are included in Table 6.1 since the cracks were grown in the middle of the beams and are therefore predominantly moved (opened/closed) by these modes. The strain energy per unit strain squared for mode 21 was used for higher order modes if these were excited in the beams.

In Figure 6.1, the power dissipated at the crack calculated in the frequency domain is compared to the power profile obtained in the time domain for a selection of tests carried out on specimens which did not show amplitude-dependent damping. The two methods produce essentially the same results, even though vibration records with strong variability of the vibration in time were selected. In the cases of Figures 6.1 (a) and (b), after an initial rapid variation, the power dissipated settles to an approximately constant value until the excitation is switched off. In the cases of Figures 6.1 (c), (d) and (e) the power profile varies strongly in time. Figure 6.1 (c) shows an extreme case in which the power peaks sharply and returns to a base level. As explained in section 5.2.4, these characteristics are a product of the uncontrolled coupling between the exciter and the structure. In Figures 6.1 (b) and (d) the frequency domain prediction produces a slightly higher power dissipated, whereas in Figure 6.1 (c) the time domain prediction produces a slightly higher estimate of power dissipation around the peaks. This is not surprising, considering that the mechanism of power dissipation at the crack is not perfectly linear.

For the purpose of this study, the frequency and time domain post-processing algorithms will be considered equivalent on specimens where the crack damping is reasonably independent of amplitude. In Chapter 5 it was shown that the thermosonic temperature rise can be predicted, to a reasonable degree of accuracy, using

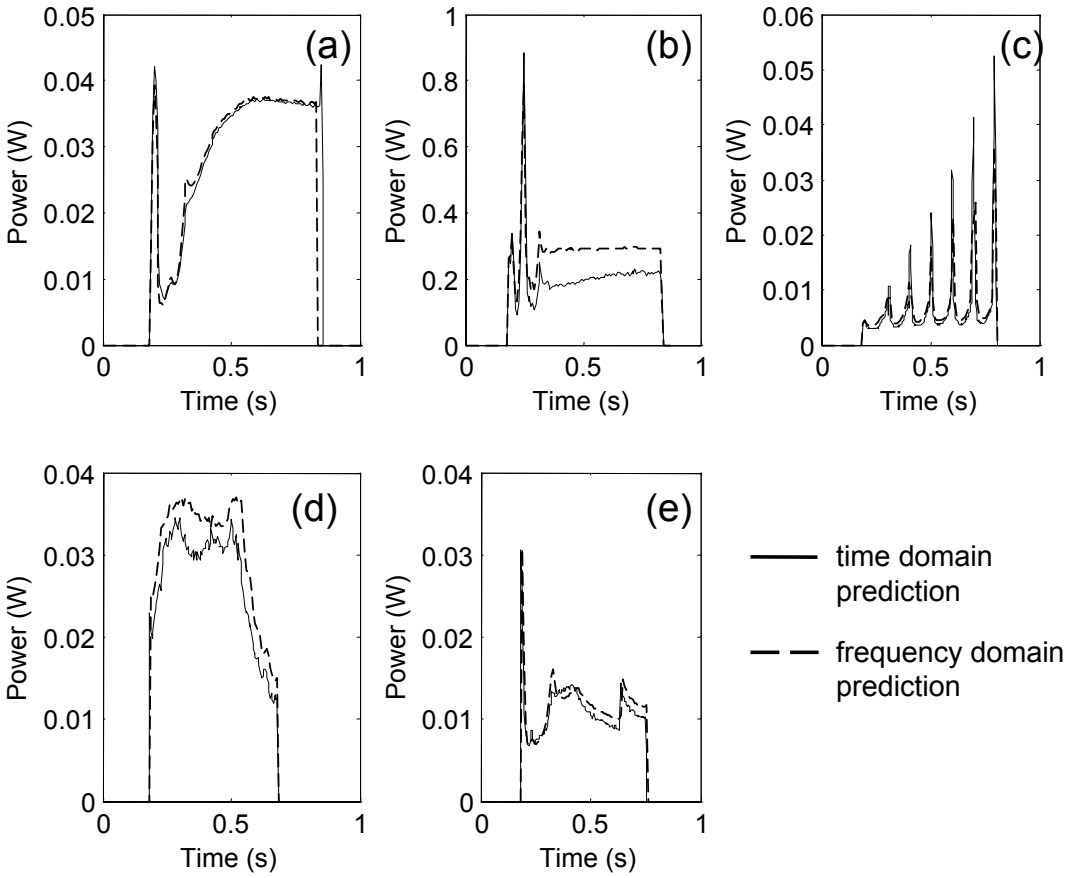

Figure 6.1: *Comparison of the power dissipated at the crack calculated using the time domain (solid line) and the frequency domain (dashed line) methods for specimens with non-amplitude-dependent crack loss factors: (a), test 3 on specimen T-4; (b), test 13 on specimen T-7; (c), test 10 on specimen TT-1; (d), test 6 on specimen TT-3; (e), test 5 on specimen TT-5.*

time domain post-processing of strain records. We can therefore conclude that, for cracks showing an approximately linear extra-damping, the frequency domain post-processing can equivalently be used to predict the thermosonic signal. The aim of the next section is that of introducing a single parameter able to determine whether a thermosonic test is good enough to allow the detection of a crack of given size; this new parameter will require the decomposition of the thermosonic strain in its frequency components. Hence, it has been necessary to compare the time domain approach and the frequency domain approach in this section.

6.3 Calibration

In practical NDT testing, a preliminary calibration is very often required before performing real inspections. Calibration procedures are meant to reliably insert an NDT methodology into a real inspection context. This involves identifying the characteristics of the equipment which is available for testing, finding information on the target defect which has to be detected, gathering knowledge of the response of the system to a non-defective reference sample, etc.. In this practical perspective, one can imagine that a number of thermosonic tests will be carried out on defective and non-defective samples, using the exciter and the IR camera available, before starting real inspections. Information on the damping introduced by the defects to be detected would be valuable, as it could be used to provide an estimate of the actual temperature rise to be expected for a given strain. However, in practice this kind of background information is hardly ever available since, as shown in Chapter 3, it can require complicated measurements and can be time consuming. From a practical point of view, it would be extremely valuable to develop a purely experimental calibration routine, able to ensure reliable detection of the target cracks, without a-priori knowledge of the crack damping and of the strain energy per unit strain squared in any mode.

6.3.1 Energy index (EI)

We have previously seen that, for small cracks, the damping can be approximated to a constant which can be used at any amplitude and frequency. It was also shown that large amplitudes and high frequencies are beneficial towards achieving the threshold power dissipation needed to detect the crack. The energy dissipated is proportional to the strain squared and the heating rate is proportional to frequency. It seems appropriate, then, to introduce a new simpler measure of the power generated at the crack, that will be called “Energy Index” (EI):

$$EI = \sum_i W_i \epsilon_i^2 \tag{6.4}$$

where $W_i = f_i/f_0$ is the "weight" of the frequency component ϵ_i, and is computed as the ratio of the frequency, f_i, of the strain component, ϵ_i, to the conventionally chosen center frequency of the exciter, f_0 (=40 kHz in our case). The EI function now introduced is very similar to the actual power dissipated at the (small) crack computed in the frequency and/or time domain (equation 6.2). However, in the case of EI, the absolute magnitude is arbitrarily scaled (by arbitrarily choosing a center frequency f_0), it does not depend on the crack damping (compare equation 6.4 with equation 6.2) and it does not incorporate the strain energy coefficient C_N which appears in equation 6.3.

6.3.2 Heating index (HI)

The energy index cannot be correlated, as is, to the temperature rise that can be expected on the cracks. The temperature rise depends on the thermal response of the beam/crack system to the excitation function represented by the power liberated at the crack (this has been discussed in section 5.3.1 in Chapter 5). If the vibration exceeds a threshold value, then a temperature rise is measured by the IR camera. If the heat is produced on the surface of the specimens, at the mouth of the crack, it is readily measurable in the form of a temperature rise. If the heat source is deeper towards the crack tip, then the heat will have to diffuse towards the monitoring surface before being detected. At any instant, the actual temperature rise measured by the camera is the result of contributions from the heat currently being generated close to the surface and from the heat, generated earlier over the crack depth, which has diffused towards the surface. In real applications, it would be extremely difficult to estimate the heating distribution over the crack, as was done in Chapter 5; hence, it will not be possible to know precisely the delay corresponding to the heat that has been generated beneath the surface. An accurate modelling of the exact locations where the heat is released over the cracked area would depend on a detailed knowledge of the crack morphology, which has already been shown (Chapter 2) to be very complex. For practical purposes, it would be useful to introduce a simple parameter able to describe the basic physics of thermosonic heating without knowing exactly

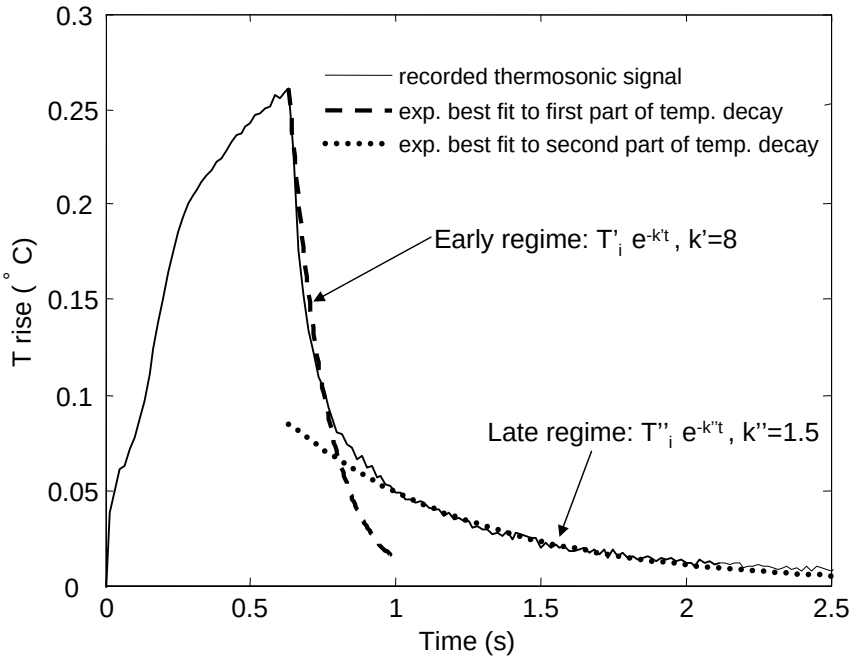

Figure 6.2: *Temperature rise recorded for test 17 on specimen T-4 and curve fitting of the temperature decay after switching off the ultrasonic excitation. This can be approximately decomposed into two exponential decay regimes: the early decay (dashed line, $T_i' e^{-k't}$) is faster than the later decay (dotted line, T_i"$e^{-k"t}$).*

where the heat is generated. If most of the heat is produced at the surface, the transient thermal response will tend to be faster and predominantly driven by the instantaneous value of the energy index. If most of the heat is produced internally, the thermal gradients will tend to be slower and their magnitude will be dominated by the sum of the contributions from heating which has occurred earlier. In this work, the following "Heating Index" (HI) can be introduced to model the behaviour described above:

$$HI(\tau) = \int_0^{\tau} e^{k(t-\tau)} EI(t) dt \tag{6.5}$$

where τ is time, t is the time integration variable, k is a time constant and EI is the energy index. In other words, this index is a weighted integral of EI where the weight function is an exponential decay which is equal to unity for $t = \tau$. The time constant k expresses the rapidity of decay of this weight function.

A justification for the use of an exponential weight function like the one in equation

6.5 can be obtained by analyzing the recorded transients of temperature decay after switching off the ultrasonic excitation as they provide, for each crack, the information on the relative proportions of heat that are produced closer to the surface or nearer the crack tip. For example, a very rapid transient could correspond to a very shallow crack with most of the heat being released very close to the surface. Figure 6.2 shows the thermosonic signal recorded during one experiment on one of the specimens tested in Chapter 5. The shape of the temperature decay after the ultrasonic excitation has been turned off cannot be modelled using one single analytical function [93]; the temperature decay immediately after the termination of the excitation is typically faster than the decay at a later time. The point of maximum curvature ("elbow" point) of the recorded temperature decay separates two regions within the transient of decay that can be defined as, respectively, the early and the late regimes. Temperature decays with similar features were obtained in all tests, and were also reproduced accurately by the thermal models described in section 5.4 of Chapter 5. Ideally one would use the shape of these temperature decays as weight functions in equation 6.5. However, this can be impractical as there is no single analytical expression for these shapes. However, each of the two regimes of decay in Figure 6.2 can be approximated by a simple exponential-law decay of type $T_i e^{-kt}$ by choosing opportune values for the constants T_i and k. The first regime is the one that will predominantly determine the actual value of the temperature rise on the specimen surface during a thermosonic test, as it is the earlier and the faster of the two. For this reason, it seemed sensible to use a single exponential weight function in equation 6.5.

The simplest method to find appropriate values of k for each crack, during the calibration stage, is then by looking at the initial part of the decays of the temperature signals recorded after switching off the exciter in all positive-detection tests for each specimen. Figure 6.3 shows the fitting of an exponential-law curve to the early regime of temperature decay recorded in three tests on three different specimens. For specimen T-7 (previous batch of cracked specimens) a typical value of $k = 5$ was obtained in Figure 6.3 (a); for specimens TT-1 and TT-2 (new batch of specimens), the typical values of k were respectively 30 and 15, as seen in Figures 6.3 (b) and

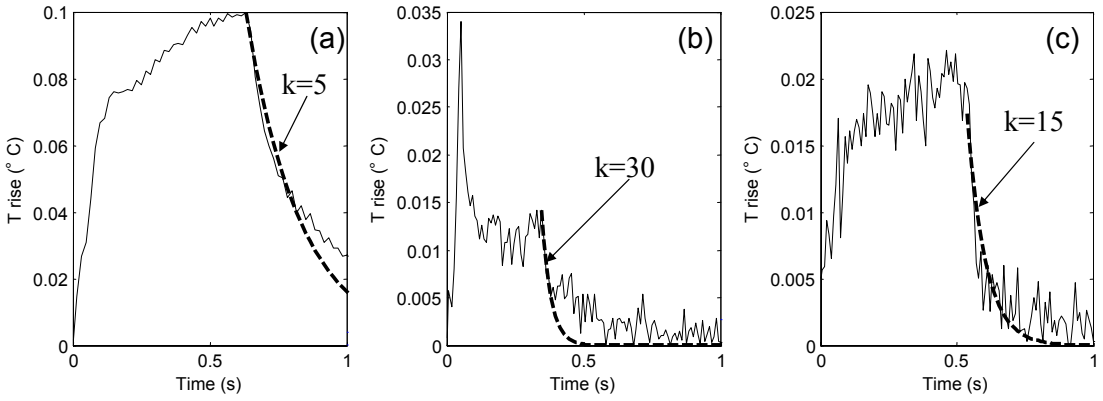

Figure 6.3: *Curve fitting of the early part of the temperature decay for the estimation of the time constant k. The solid lines represent the thermosonic signal and the dashed lines the exponential-law best fit. (a) Test 17 on specimen T-7: $k = 5$. (b) Test 16 on specimen TT-1: $k = 30$. (c) Test 3 on specimen TT-2: $k = 15$.*

Table 6.2: *Integration constants used to calculate the heating index. The variability among different tests for each specimen is given by the standard deviation (sd) over the mean value (k). For specimen TT-4 a value of 10 was assumed as a temperature rise was never detected.*

Beam	T-1	T-2	T-3	T-4	T-5	T-6	T-7
k	5	5	8	8	5	5	5
sd/k (%)	20	13	7	11	17	9	12
Beam	TT-1	TT-2	TT-3	TT-4	TT-5	TT-6	TT-7
k	30	15	5	10	10	50	10
sd/k (%)	23	33	19	-	18	34	22

(c). The time constants k which will be used in the weight function of equation 6.5 throughout this Chapter, and a measure of their scatter among repeated tests for each crack are given in Table 6.2. These values were relatively consistent among different tests on the same specimen/crack. The scatter tended to be larger for the new batch of specimens, due to the smaller measured temperature rise. However, the mean value of k allowed the heating index to be fitted consistently to the shape of the measured temperature rise (see later Figure 6.8). For the specimens used in

Chapter 5 (T-1 to T-7), generally lower values of k were found compared to those of the specimens to be tested in this Chapter (TT-1 to TT-7). This is not surprising considering that these latter specimens all contain smaller defects and hence the heat will be generated closer to the crack mouth. Specimens TT-1 and TT-6 show the highest values of k. This could be explained by heat being generated for these specimens in a very shallow region at the crack mouth (note that if the heat was produced by a line source on the surface of the specimens a value of k around 1000 would be obtained). An assigned value of $k = 10$ was given to specimen TT-4 since, for this specimen, it was never possible to measure a temperature rise (refer to section 6.4). An alternative method to find appropriate values of k could be by using a "try-and-error" procedure assuming different values of k until the shape of the measured temperature rise is well reproduced by the shape of the heating index.

With the introduction of the exponential weighting function in equation 6.5, the response of the system to the generation of heat at the crack (described by EI) can be modelled in a very simple manner but retaining the fundamental physical characteristics. Furthermore, the heating index HI can be derived immediately from the temperature and strain measurements, without resorting to additional experiments/information. This is very valuable in view of the definition of easy calibration procedures for real-life thermosonic applications. Naturally, it will be important that the batch of calibration cracked specimens is representative of the real target cracks that will have to be detected in real life; the time constant k that will have to be used in real testing will be the highest amongst the time constants found in the calibration tests so to obtain conservative estimates of the heating index in each test.

6.3.3 Use of HI in the calibration procedure

In Figure 6.4, three examples are provided to illustrate the use of EI and HI. The strain at the crack, the spectrograms of the strain, EI, HI and the actual temperature rise are shown for three tests on three different specimens. The left-hand column (a) shows a test-case during which a stationary regime of vibration has been

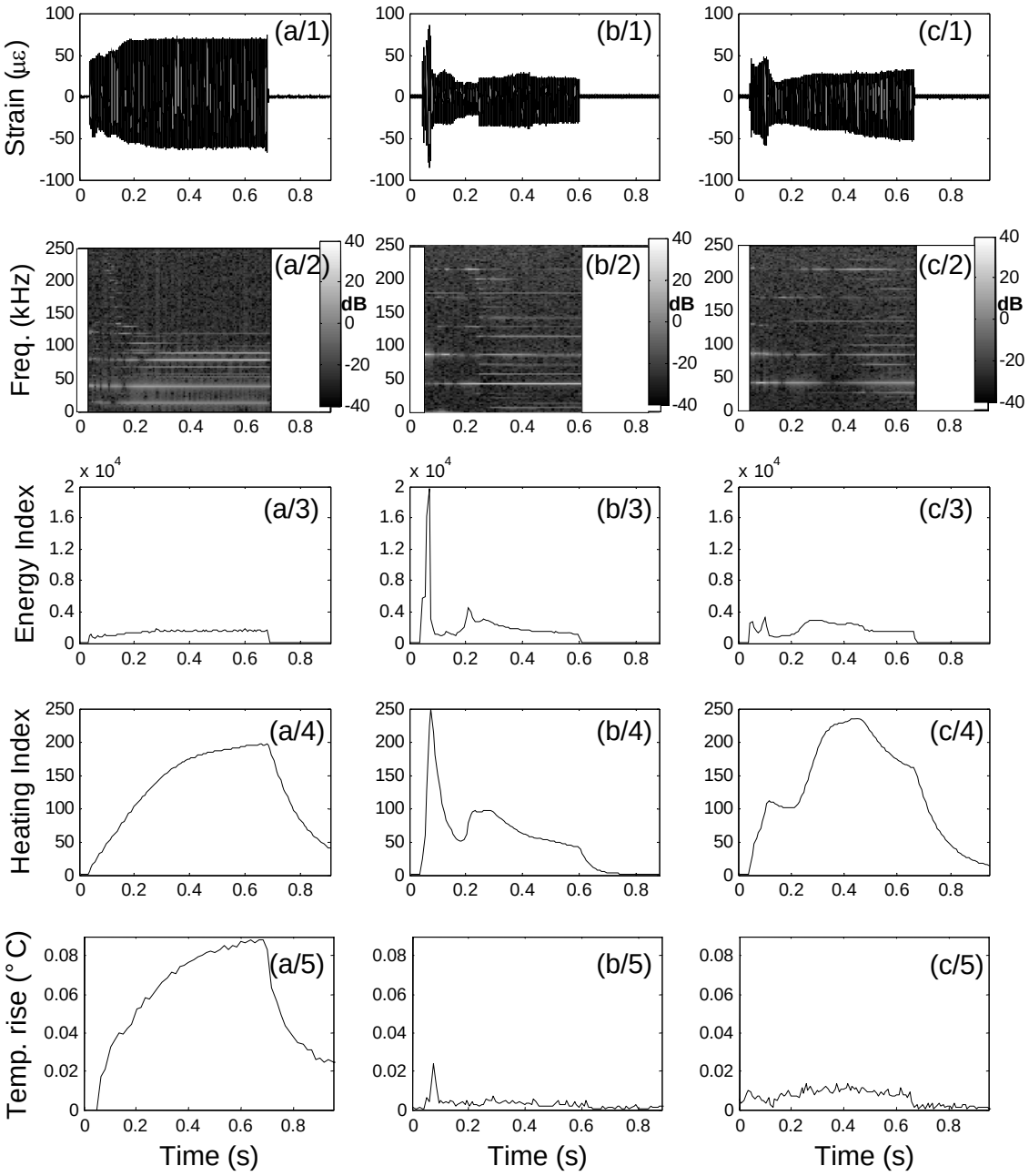

Figure 6.4: *Calculation of the energy index and heating index for different tests on different specimens. First column from left: (a/1) strain record for test 10 on specimen T-4; (a/2) its STFT; (a/3) energy index; (a/4) heating index ($k = 8$); (a/5) actual measured temperature rise. Second column from left: (b/1) strain record for test 7 on specimen TT-1; (b/2) its STFT; (b/3) energy index; (b/4) heating index ($k = 30$); (b/5) actual measured temperature rise. Third column from left: (c/1) strain record for test 6 on specimen TT-5; (c/2) its STFT; (c/3) energy index; (c/4) heating index ($k = 10$); (c/5) actual measured temperature rise.*

practically reached after approximately half of the pulse duration. This is seen from the strain amplitude [Figure 6.4 (a/1)] and from the short-time Fourier transform plot of the strain [Figure 6.4 (a/2)]. The spectrogram also shows the dominant frequency components at around 40 kHz and 80 kHz, with other contributions from several sub-harmonics (mainly 1/3 of 40 kHz and its multiples) and super-harmonics (120 kHz) of the driving frequency. The corresponding energy index is very close to a step function [Figure 6.4 (a/3)]. The heating index is intended to describe the "build-up" of the heat at the top of the crack in the form of temperature rise [Figure 6.4 (a/4)]. After an initial stage during which the temperature rises, a condition of equilibrium is nearly reached during which the heat supplied to the surface at the crack location is almost equivalent to the heat being diffused away. When the excitation is switched off, the temperature starts to fall rapidly. The actual temperature measurement is shown in Figure 6.4 (a/5), and confirms that HI can be used to reproduce the shape of the actual temperature rise. The middle column of Figure 6.4, (b), gives an example of a test-case with abrupt changes in the test-piece vibration. Both the amplitude [Figure 6.4 (b/1)] and the frequency content [Figure 6.4 (b/2)] change in time. When the maximum strain is reached (approximately 85 $\mu\epsilon$ just before 0.1 seconds), the 80 kHz component becomes dominant before stabilizing at lower amplitudes comparable to that of the 40 kHz component. At a time instant between 0.2 and 0.3 seconds, the regime of vibration changes completely: before this time the 40 and 80 kHz components dominate the vibration whereas after this time the spectrum becomes rich of many sub-harmonics of the driving frequency. The energy index shows a high peak close to the onset of vibration, Figure 6.4 (b/3). The heating index [Figure 6.4 (b/4)] also presents one large peak, as a result of the integration of equation 6.5. The recorded temperature rise, see Figure 6.4 (b/5), shows a visible peak corresponding to the peak of the HI function. This case indicates that a peaky behaviour of the vibration is actually very beneficial for the purpose of defect detection as the vibration threshold necessary to measure a temperature rise could be surpassed only in the presence of such peaks. The right-hand column, (c), illustrates an example of a test showing an intermediate degree of variability of the vibration of the test-sample in time [Figure 6.4 (c/1)], but involv-

ing higher frequency components [Figure 6.4 (c/2)]. All the super-harmonics of the driving frequency are excited between 80 and 200 kHz. After around 0.5 seconds, the spectrum is enriched by the onset of frequency components at multiples of the sub-harmonic at 1/3 of the driving frequency. The energy index [Figure 6.4 (c/3)] varies moderately around an average level very similar to that of Figure 6.4 (a/3). The corresponding heating index [Figure 6.4 (c/4)] is also similar in magnitude to that in Figure 6.4 (a/4). However, the actual temperature rise of Figure 6.4 (c/5) reaches a much lower maximum level and indicates that the heat generated by this crack is barely sufficient to sustain a measurable temperature rise. This can be explained by recalling that the temperature rise will be proportional to HI for a given crack, but the temperature rise for a fixed HI will depend on the crack characteristics. The correlation between HI and the actual temperature rise measured on the cracks will be discussed in detail later in section 6.4.2. The lower temperature rises measured in Figure 6.4 (b/5) for specimen TT-1 and in Figure 6.4 (c/5) for specimen TT-5 compared to that measured for specimen T-4 in Figure 6.4 (a/5), in three tests characterized by a similar maximum HI, are due to the sizes of the cracks which are smaller for specimens TT-1 and TT-5.

Figure 6.5 shows a flow-chart of the calibration process. Initially, the region(s) of the component where a crack could grow and the target size of the defects to be found have to be defined (oval block) and a representative set of cracked specimens has to be made available or produced. The excitation and supports should be optimized to produce a strain large enough to measure a temperature rise on the cracked samples. The analysis of the thermosonic temperature records will provide an estimate of the typical time constant k to be used in the calculation of HI as described earlier. Again, if for one or more cracked specimens in the calibration batch, k is substantially greater than the average, the highest value of k should be used in real testing as it will yield a conservative HI for a given strain record. EI and HI are arbitrarily-normalized (40 kHz was conventionally chosen as center frequency) estimates of respectively the power dissipated at the crack and the temperature rise to be expected on the crack. If calibrated against the actual temperature rise recorded for a crack of known size, HI can be used as the reference parameter to determine whether the excitation

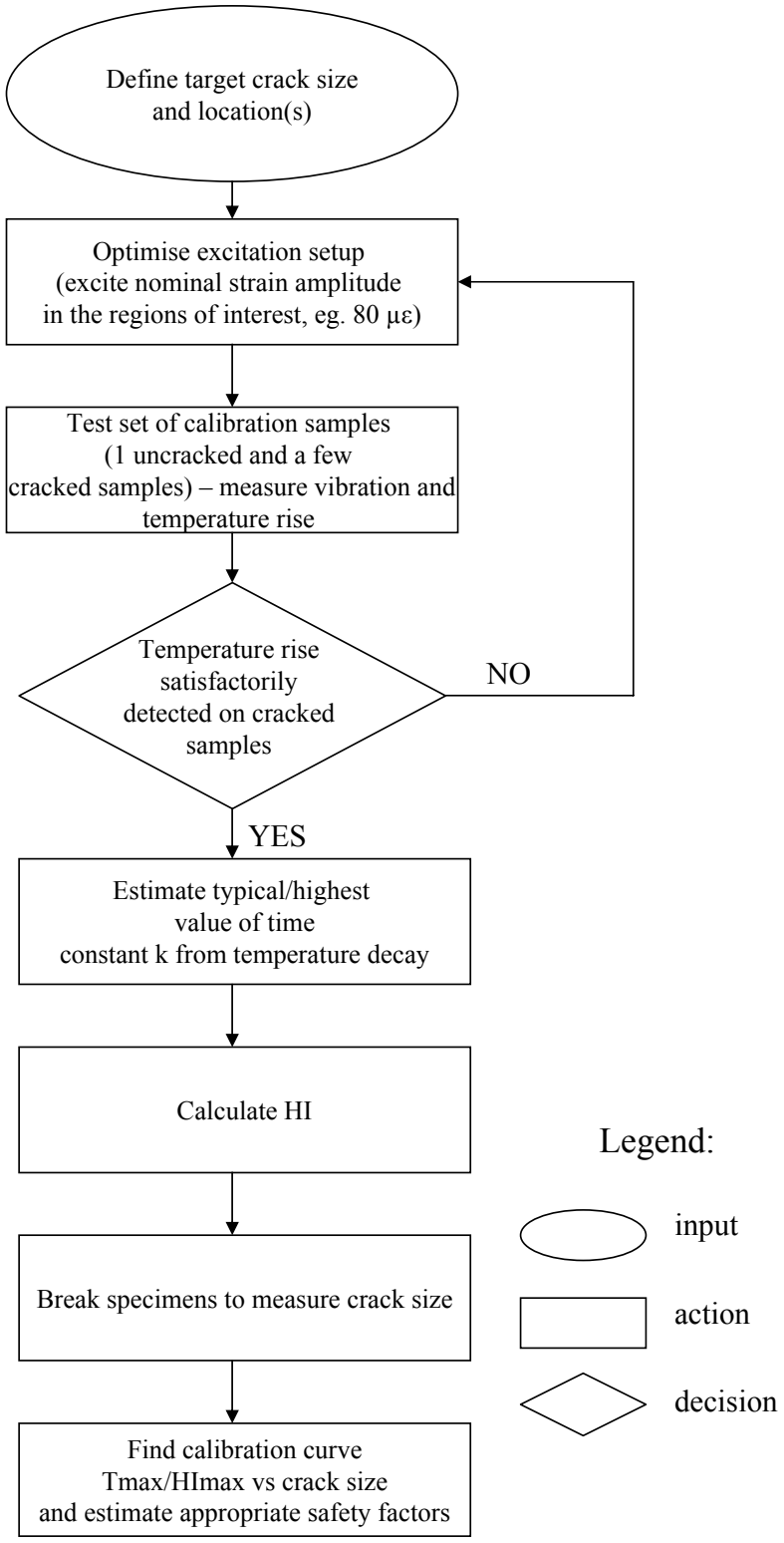

Figure 6.5: *Flow chart showing the calibration procedure.*

delivered in a particular test would be sufficient to detect any defects of the target size or above that are present. This calibration will be done by calculating the ratio of the maximum temperature rise (T_{max}) to the maximum HI (HI_{max}) for all positive-detection tests and by plotting this as a function of the actual crack size measured after breaking the specimens (rectangular box at the bottom of flow-chart). The best-fit curve obtained from these experimental data will be used as the main calibration curve, since it provides an estimate of the temperature rise per unit HI to be expected during the inspection of cracks of predetermined size. Furthermore, the scatter in the experimental data could be used to estimate an appropriate safety factor to be used during real testing. The following section shows the details of this calibration procedure for the specimens and testing setup used throughout this work.

6.4 Analysis of results

In this study, the location of the crack is known before testing. This makes the detected/undetected judgement easier for the person who is conducting the test. The IR images shown in Figure 6.6 illustrate three typical test cases obtained testing the specimens TT-1 to TT-7: (a) detection failed, (b) detection barely achieved and, (c), detection easily achieved [note the different temperature scale in (c)]. The images have been post-processed using background subtraction. This was done by subtracting the first frame within each acquisition sequence from all successive frames. The amplitude of the resulting images, therefore, gives a temperature variation with respect to the initial instant. The judgement on the presence of a crack is taken on the basis of the contrast between bright pixels on the crack and dark pixels away from the crack during ultrasonic excitation. In Figure 6.6 (b), only the lower segment of the crack becomes visible. This could be explained by analyzing the details of the crack morphology. However, for the purpose of this study, this is a sign that the vibrations excited are barely sufficient to produce a visible thermosonics signal. In the tests described in Chapter 5, a temperature rise was always measured across the whole crack width. The size of the array of pixels covering the crack mouth is a

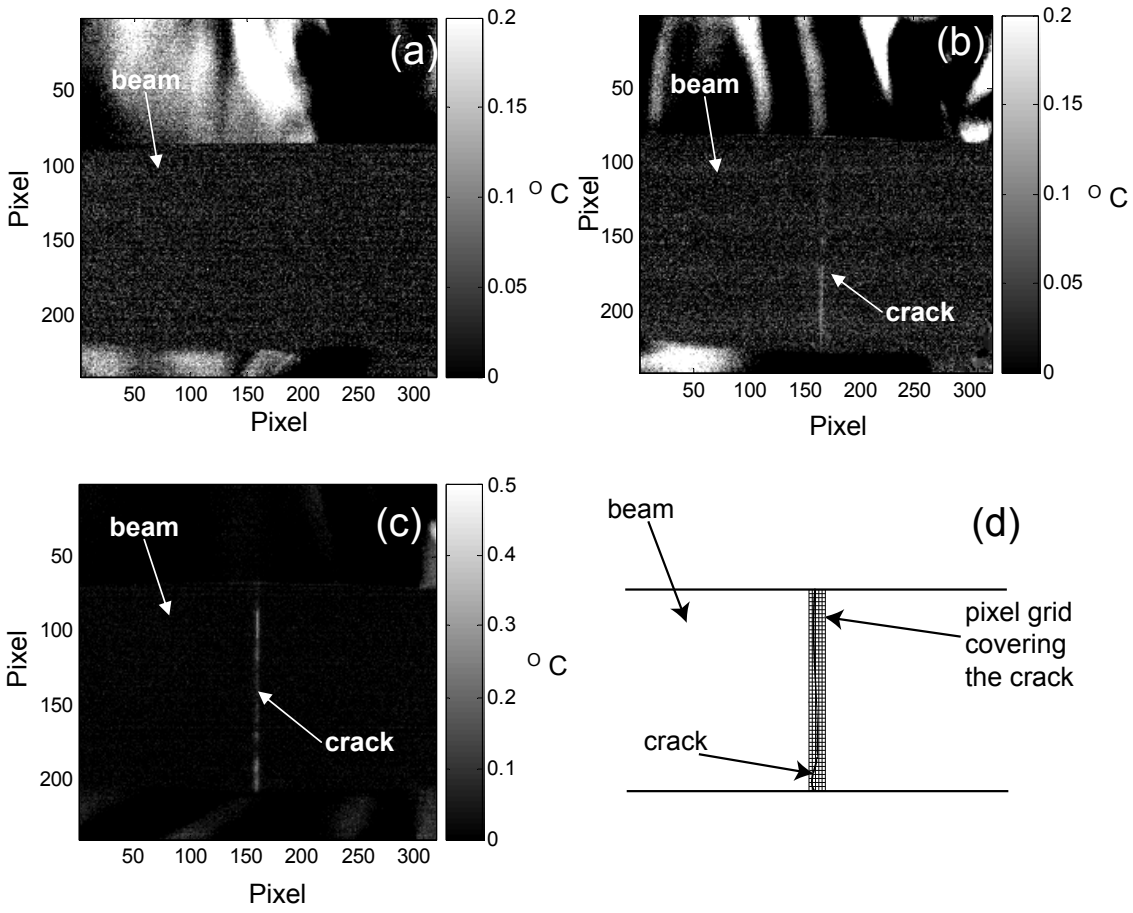

Figure 6.6: *Examples of IR measurements during thermosonics testing on the beams TT-1 to TT-7. (a) Crack not detected during a test on beam TT-1. (b) Crack detected during a test on beam TT-5: heat is generated in the lower segment of the crack. (c) Crack detected in one of the tests on beam TT-6: in this test, the highest temperature rise among all tests on this batch of specimens was recorded (around 0.5 °C). (d) Schematic showing the grid of IR camera pixels covering the crack region.*

function of the distance of the camera from the beam. Typically, an array of 150×5 (rows x columns) pixels covered the area occupied by the crack mouth, as seen in the schematic representation of Figure 6.6 (d). The thermosonic signal in time was extracted by considering, at any instant, the brightest pixel within each row, and then averaging across the crack width (column direction). In addition, this spatial averaging reduces the noise level in the so-called thermosonic signal compared to the baseline IR image noise level. As earlier discussed, the noise level in the thermosonic test described here was around 0.004 $°C$

6.4.1 Pass-fail analysis

The first stage of the experiments involved testing the detectability of the cracks in the new specimens TT-1, TT-2, etc. A few tests were run for each specimen looking at whether the crack was or was not detected. For specimen TT-4 it was never possible to detect the crack with the particular setup and excitation system used. For specimens TT-1, TT-3, TT-5 and TT-6 the cracks could be detected after a few trials. For specimens TT-2 and TT-7 the crack could be detected after many trials. Thus, it was decided to break specimens TT-2, TT-4 and TT-7 at this stage to reveal the size of the cracks, without testing them further. The defect in specimen TT-4 (never detected) was measured to be 2.9 % of the total cross section. Specimens TT-1, TT-3, TT-5 and TT-6 were retained in order to take further measurements to validate the use of HI in the calibration procedure and then to obtain criteria for the reliable detection of cracks in real inspections. The solid points in Figure 6.7 show the maximum HI reached among all failed-detection tests on each specimen, plotted versus crack size; the hollow points represent the minimum HI measured among all positive-detection tests on each specimen plotted versus crack size. The best-fit line was evaluated considering only the three positive-detection points that seem to lie on a reciprocal-law curve, since they represent the three lowest positive-detection HI relative to crack size. The model fitted to these points was the power-law $y = ax^b$, where a and b are two coefficients. These were found to be $a = 10.9 \times 10^3$ and $b = -2$ using a nonlinear regression method. The area to the right of this curve represents the area of probable detection whereas the area to the left the region with significant chance of failure to detect a crack. Conversely, if the maximum obtained HI is known from the strain record, the minimum detectable crack size can be obtained from this graph. From Figure 6.7 it can also be seen that the values of the highest negative-detection HI and the corresponding lowest positive-detection HI for each of the three specimens considered to find a best-fit line (specimens TT-2, TT-3 and TT-7) lie relatively close to this curve, confirming that the best-fit line is close to the boundary of detectability for cracks of different sizes.

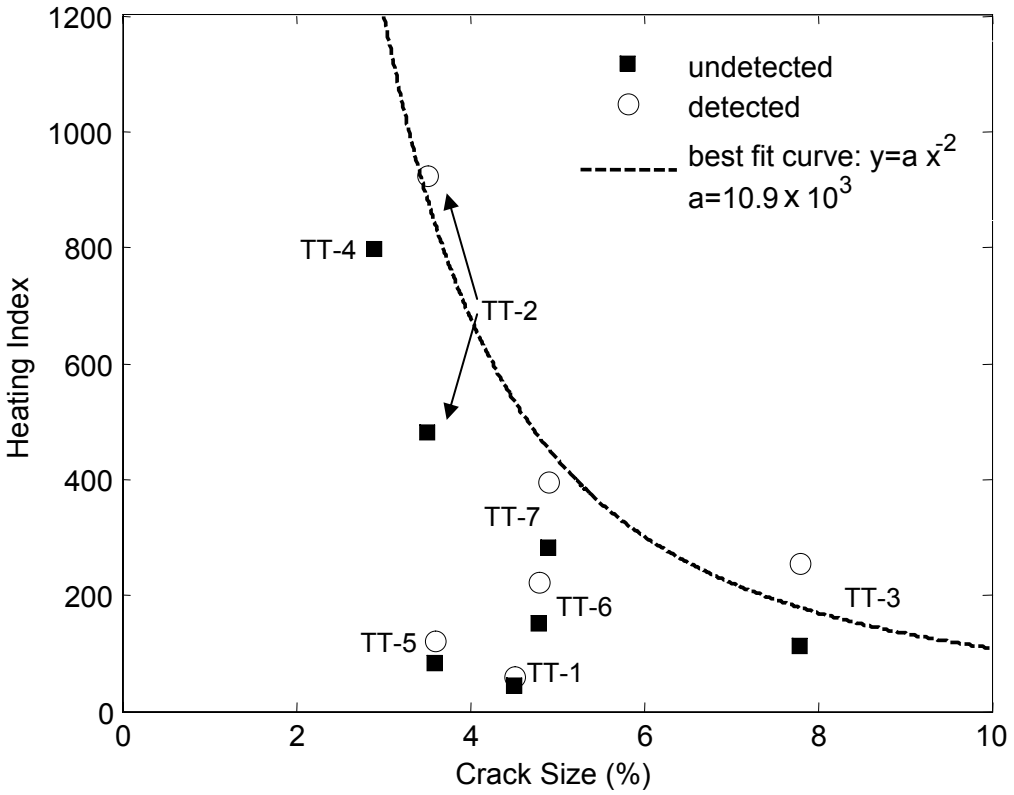

Figure 6.7: *Maximum failed-detection HI and minimum positive-detection HI amongst all tests in specimens TT-1 to TT-7 plotted vs crack size (given as percentage of the total cross section of the beams). The dashed line expresses the reciprocal power-law best fit for the specimens TT-2, TT-3, TT-4 and TT-7 (specimens with the relative highest failed-detection heating index).*

6.4.2 Correlation between HI and temperature rise

Before proceeding to a closer study of the vibration threshold required to detect a crack, the use of HI to describe the temperature rise on the specimens can be validated against the recorded temperature rise for each test. Figure 6.8 presents the results for all positive-detection tests carried out on specimen TT-5. HI and the thermosonic signal are normalized to unity. The correlation of the shape of the HI function with the measured temperature rise is very good for all tests except for the one in Figure 6.8 (b). The tests in Figures 6.8 (a) to (j) show a noisy recorded temperature rise profile due to the baseline noise present in the measurements, meaning that these tests are those for which a weaker temperature rise was produced.

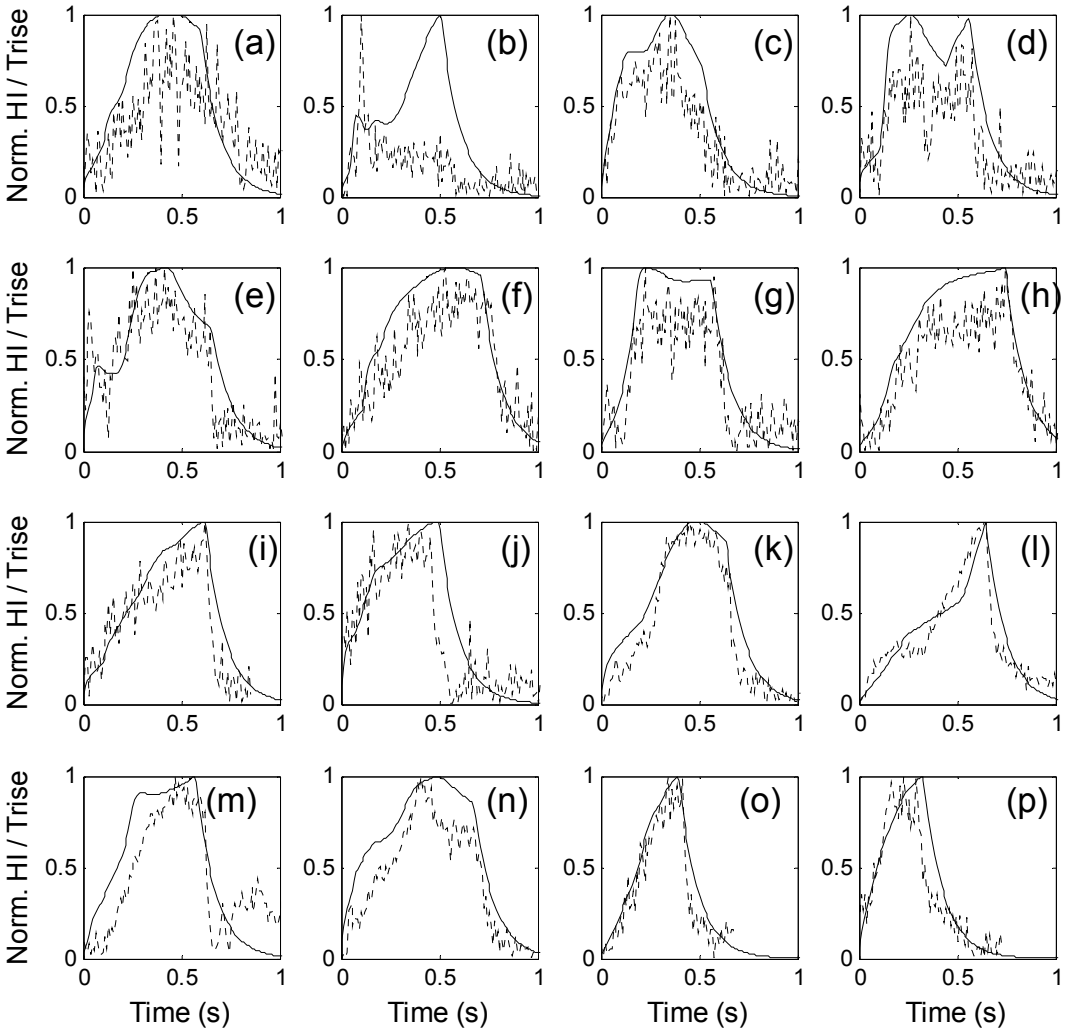

Figure 6.8: *Normalized heating index (solid line) and temperature rise (dotted line) for all positive-detection tests on specimen TT-5: (a) test 1; (b) test 2; (c) test 3; (d) test 4; (e) test 5; (f) test 6; (g) test 7; (h) test 8; (i) test 9; (j) test 10; (k) test 11; (l) test 12; (m) test 13; (n) test 14; (o) test 15; (p) test 16.*

The cases of Figures 6.8 (k) to (p) show a cleaner profile of the temperature record.

In Figure 6.9 the maximum value of temperature rise is plotted versus the maximum value of HI for all positive-detection tests on specimens TT-1, TT-3, TT-5 and TT-6 (hollow points). The highest negative-detection heating index is also included for each specimen (solid point as in Figure 6.7). Good linear correlation was obtained for all four specimens considering the positive-detection test-cases. This validates

the use of HI as the reference parameter in practical thermosonic applications, as this is a good measure of the actual temperature rise to be expected. The best-fit line has been calculated for each specimen from the positive-detection experimental points in Figures 6.9 (a), (b), (c) and (d) [the scale in (d) is expanded by 50% compared to (a), (b) and (c)] using the least squares method including the origin in the population of experimental points (no temperature rise must correspond to absence of ultrasonic stimulation). The horizontal lines represent the temperature threshold value, i.e. the value which has to be surpassed by the thermosonic signal to reliably detect the cracks; this value was provisionally set to twice the noise level associated with the measurement and is here equal to 0.008 $°C$. This choice was, however, rather arbitrary at this stage and was only intended to indicate a "rule of thumb". In real applications this threshold temperature rise will have to be defined accurately. It will depend on the base camera sensitivity, on the post-processing of the thermal measurements and on the pass-fail criteria specified for that specific application. For example, if temperature rise is occurring for the whole duration of the ultrasonic pulse, this could provide enough evidence on the crack presence even if the maximum value of the temperature is very close to the threshold value. On the other hand, if the temperature rise is a single sharp spike within the duration of the pulse [similar to the case of Figure 6.4 (b/5)], it could be said that the maximum value needs to be three or four times higher than the threshold value before concluding on the presence of a crack; otherwise, the test should be run again. The highest failed-detection test for each specimen (a "zero" temperature rise was assigned to these tests) is also included in Figure 6.9; the highest HI for the failed-detection tests for all specimens was already used to plot Figure 6.7. The intercept of the best-fit lines in Figure 6.9 with the threshold temperature rise can be used to better define the threshold values for HI. For example, for specimen TT-1 it can be said that HI needs to be higher than approximately 50 to detect the crack.

The parameters EI and HI are meant to be used in practice with no extra knowledge on the crack characteristics such as damping, size, shape, etc.. It is only necessary that the calibration cracked samples are similar to the cracks that need to be detected in real life. For completeness, it would be useful to compute EI and HI for the strain

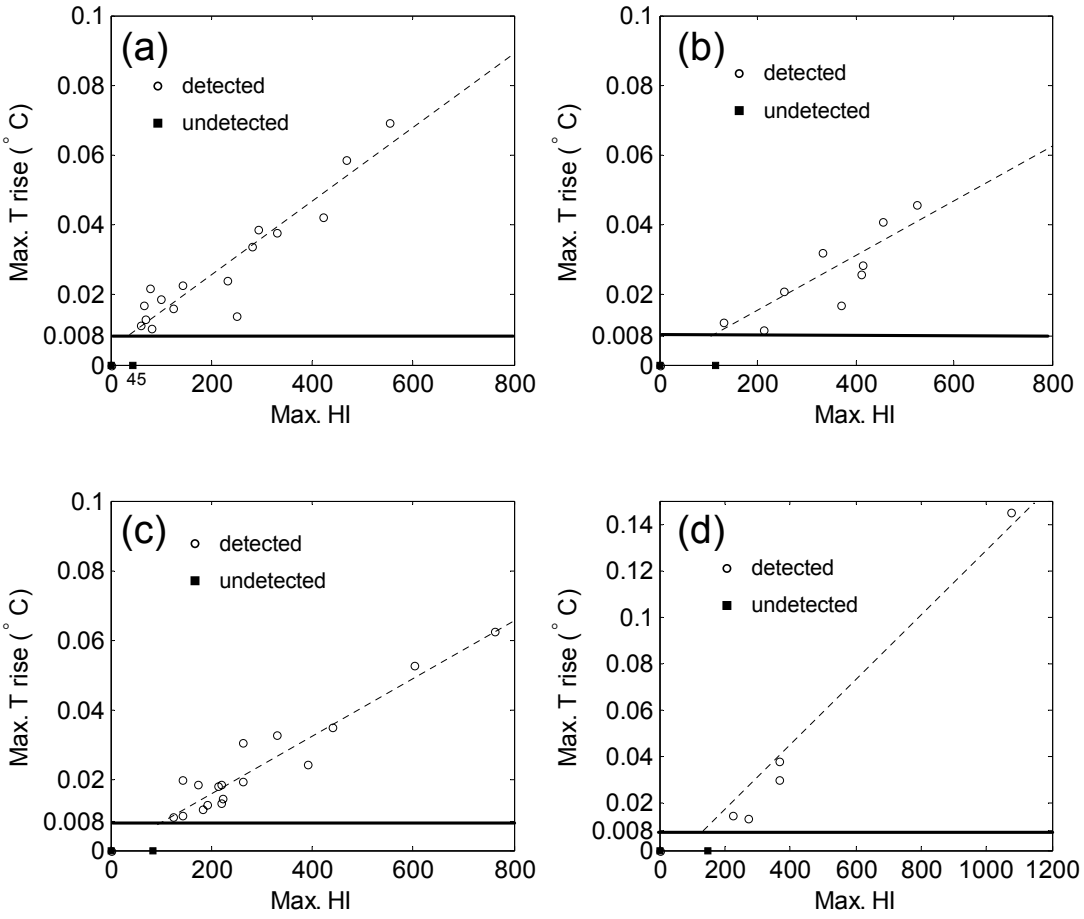

Figure 6.9: *Maximum temperature rise vs maximum HI for specimens with small cracks: (a) specimen TT-1; (b) specimen TT-3; (c) specimen TT-5; (d) specimen TT-6. The dashed lines are the best fits. The horizontal lines at 0.008 °C represent the threshold temperature rise.*

records obtained for the specimens with larger cracks used in Chapter 5. If the maximum HI correlates well with the maximum temperature rise for these tests as well, this would further confirm that EI and HI are indeed able to model the thermosonic basic mechanism/physics and are therefore suitable to be used widely in practical applications. In Figure 6.10 HI is plotted on a normalized scale with the actual temperature rise for all tests on specimen T-4. The results indicate strong shape correlation even though, towards the end of the transient of decay, the two lines consistently seem to diverge. This is due to the fact that HI cannot represent in detail the effect of the heat coming from deeper parts of the cracks; this is mainly due to the fact that a single exponential-law weight function, found fitting a curve to

the early regime of temperature decay, was used in equation 6.5 despite the presence of a second slower regime that represents the effect of heating produced at deeper parts of the cracks (see Figure 6.2). This behaviour is likely to be greater for larger cracks. However, during the excitation pulse, HI seems to represent satisfactorily the shape of the temperature rise.

The next step is to compare the maximum values of HI with the actual temperature rise. This is shown in Figure 6.11. The results for all specimens of the previous batch, T-1, T-2, etc., are presented here together with those obtained for TT-1, TT-3, TT-5 and TT-6 previously shown in Figure 6.9. Good linear correlation between the maximum HI and the maximum temperature rise was generally obtained for all specimens. The best fit is represented by the dashed lines in Figure 6.11. It can be observed that the scatter in the experimental points is lower in the cases of Figures 6.11 (h), (i), (j) and (k) which correspond to the 4 smallest cracks. This is not surprising, since the heating index provides a less accurate estimate of the temperature rise for larger cracks. Since the larger cracks are easier to detect, this is not important practically; the issue in practice is whether the excitation was sufficient to detect the smallest cracks that must be found.

6.4.3 Calibration curve

After having validated the use of HI for real thermosonics testing (it can be calculated from the strain record and is proportional to the temperature rise), the calibration curve introduced in section 6.3.3 can now be derived. The estimation of this curve coincides essentially with a revised analysis of the sensitivity of the "thermosonic efficiency" to crack size. In section 5.6, the concept of thermosonic efficiency was defined as the average temperature rise (T_{avg}) per unit rms strain squared (ϵ^2_{rms}) and was described as the ability of a crack to generate an average temperature rise in response to an average level of strain excited in a test. At that time, this seemed an appropriate definition of thermosonic efficiency, since the temperature rise was usually measured during the whole pulse duration, and the magnitude of this temperature increase was such that the cracks could always be

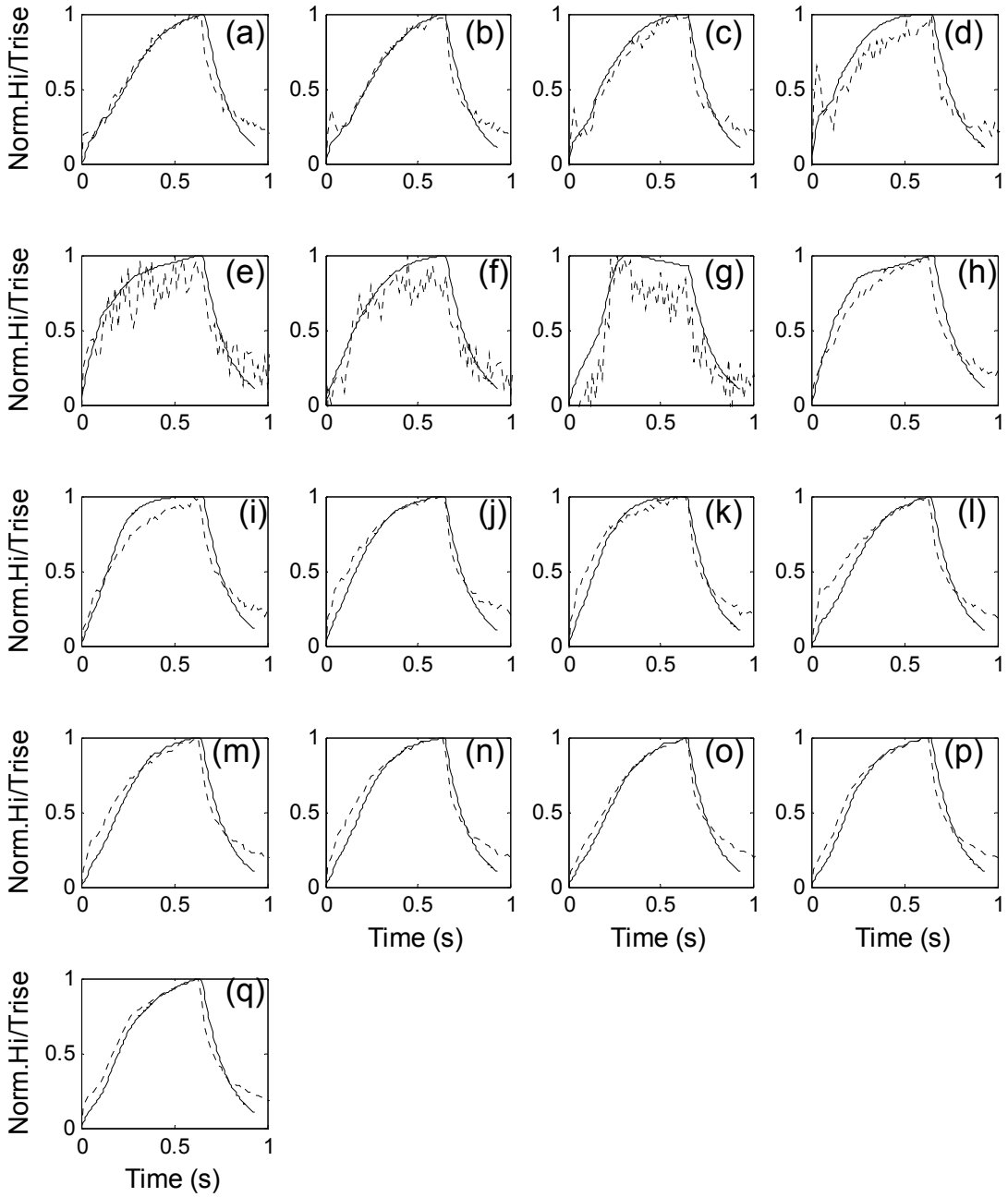

Figure 6.10: *Normalized heating index (solid line) and temperature rise (dotted line) for all tests on specimen T-4: (a) test 1; (b) test 2; (c) test 3; (d) test 4; (e) test 5; (f)test 6; (g) test 7; (h) test 8; (i) test 9; (j) test 10; (k) test 11; (l) test 12; (m) test 13; (n) test 14; (o) test 15; (p) test 16; (q) test 17.*

easily detected. Therefore, the average temperature rise, during the time interval in which the crack was visible, was taken as the reference quantity. However, from the point of view of the detection of small cracks, it is important that the thresh-

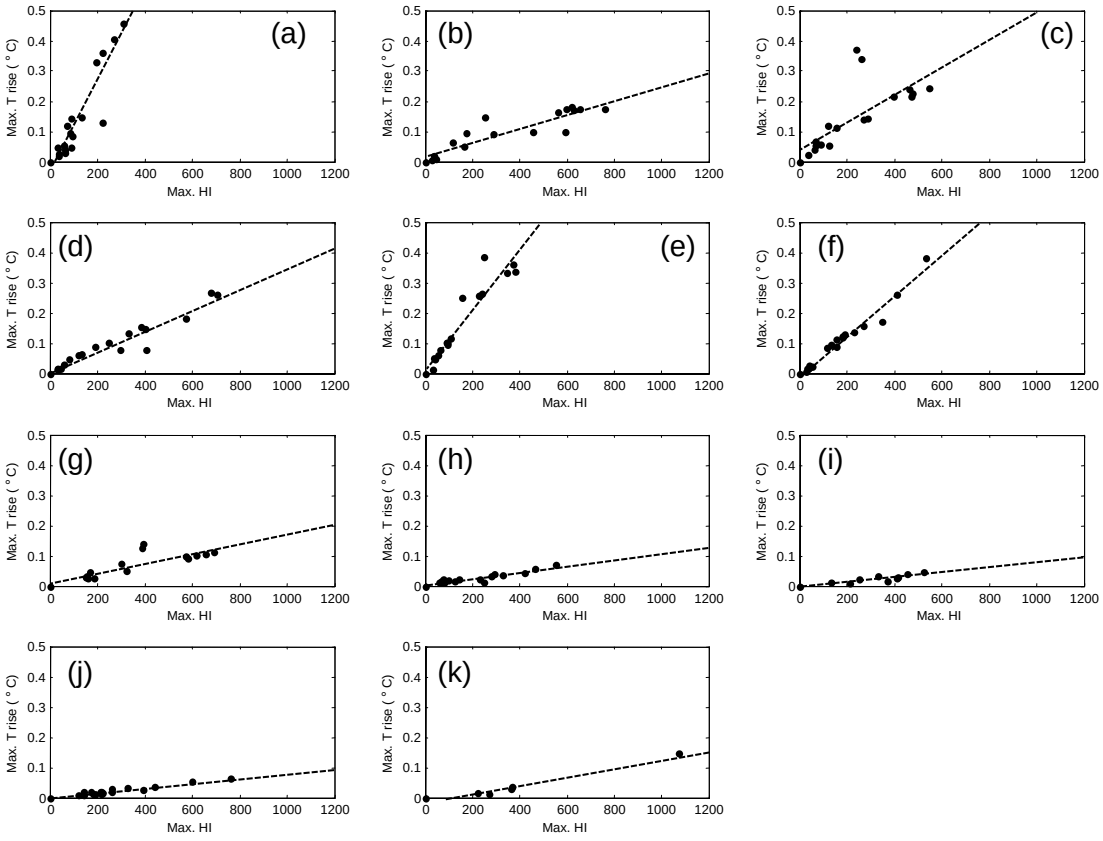

Figure 6.11: *Maximum temperature rise vs maximum HI for all available specimens and tests: (a) specimen T-1; (b) specimen T-2; (c) specimen T-3; (d) specimen T-4; (e) specimen T-5; (f) specimen T-6; (g) specimen T-7; (h) specimen TT-1; (i) specimen TT-3; (j) specimen TT-5; (k) specimen TT-6. The dashed lines represent the linear best fit. Each dot represents one test carried out on one particular specimen. Each test has an amplitude and frequency content that is particular only to that test and is typically non-reproducible.*

old temperature rise is exceeded during the vibration even for a short time interval. This case could happen when the strain record exhibits distinct peaks, like in Figure 6.4 (b/5). Cases like this occurred often during the tests on the specimens TT-1 to TT-7. Hence, at the same time as estimating the calibration curve, it seemed appropriate to revise the definition of thermosonic efficiency previously used. The ratio of maximum temperature rise over maximum of HI during a test can be now used to better characterize the thermosonic efficiency of a crack. The slopes of the best fit lines of Figure 6.11 already provide a measure of such thermosonic efficiency. In Figure 6.12, the experimental thermosonic calibration curve is shown. It represents the

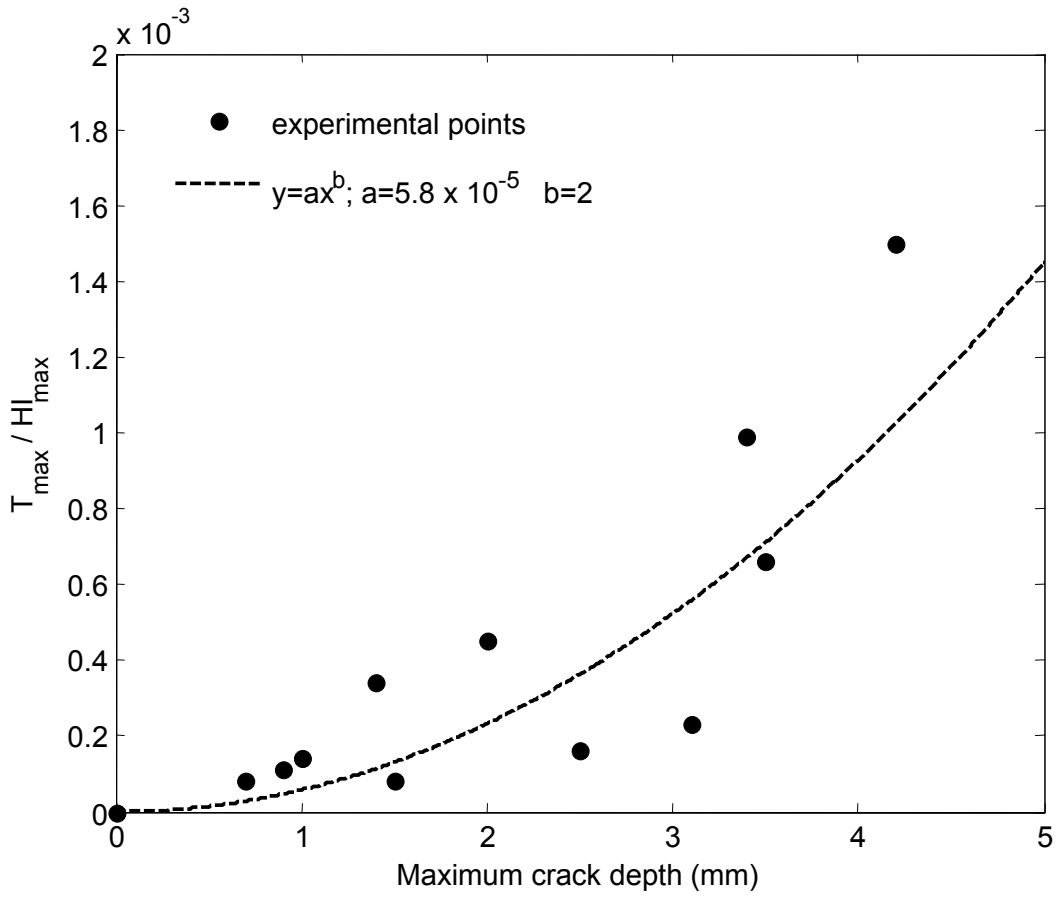

Figure 6.12: *New "thermosonic efficiency" vs crack size for all beams of Figure 6.11. The dashed line represents the best fit of the experimental data and also represents the calibration curve.*

variation of thermosonic efficiency with crack size (here the maximum crack depth was considered). The dashed line is the power-law best fit of type $y = ax^b$, where a and b are the coefficients that have been optimized using a nonlinear regression method. The choice of this model to be fitted to the experimental data was based on two considerations: first, it expresses the relative increase of difficulty to detect cracks of size tending to zero (well known to the testing operator and confirmed in Figure 6.7) and, second, this curve passes through the origin (the absence of temperature rise must correspond to uncracked specimen). However, more specimens should be tested before deciding which curve fitting model is the most appropriate. Here, the curve fitting of the twelve experimental points available is intended to provide an example. Finally, an appropriate safety factor can be determined as a

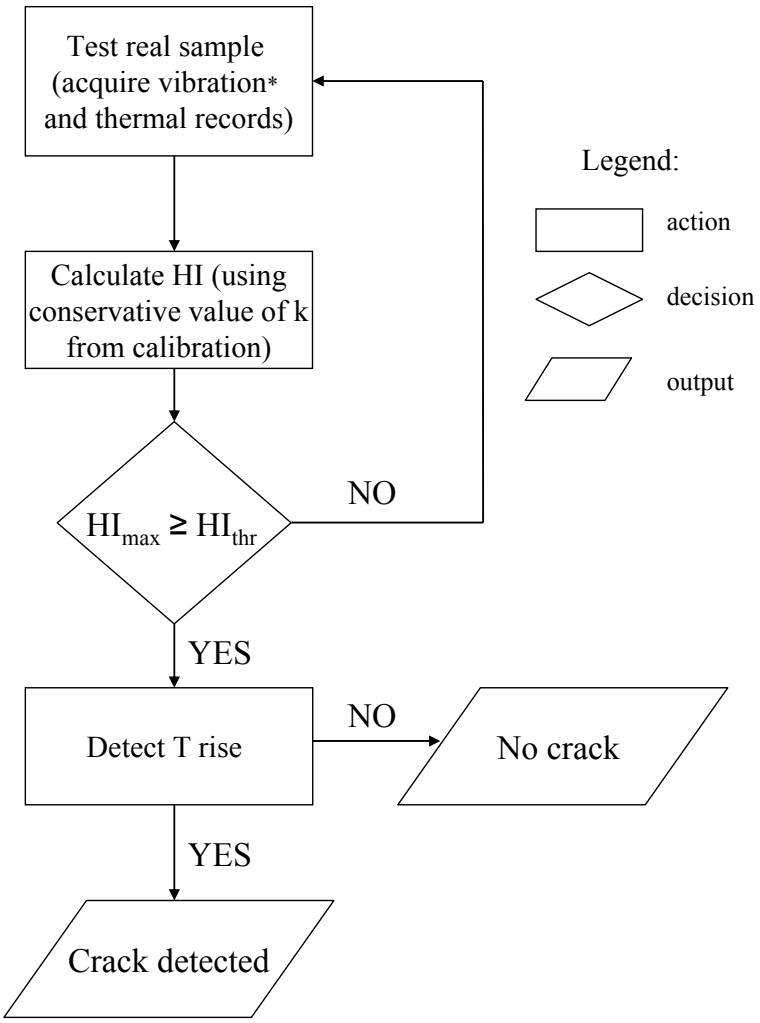

Figure 6.13: *Flow chart representing the stages involved in real thermosonics testing.*

function of the scatter of the experimental points around the calibration curve.

6.5 Criterion of detectability in thermosonic inspection

Based on the results obtained from the calibration process, a detectability criterion can be enunciated to be used in real-life thermosonics testing. This criterion, shown in the recommended thermosonic inspection procedure of Figure 6.13, is based on

the definition of the threshold heating index, HI_{thr}, which is a function of the target crack size, S_c, defined prior to the testing. After each test, the maximum HI, HI_{max}, has to be calculated using the measured strain record and the time constant k, as described in the calibration phase, and then compared to HI_{thr}. If the threshold heating index has been exceeded, then the thermal record will be post-processed looking for possible temperature rises. Based on the detection or non-detection of a temperature rise, the specimen will be judged as respectively cracked or uncracked. The actual value of HI_{thr} will depend on the results of the calibration, i.e. on the type of specimen/defect, on the sensitivity of the IR camera and on the thermal image spatial averaging used. In this study, the defects are through-width surface cracks produced at mid-span in mild steel rectangular cross section beams (the geometry was specified in Chapter 2), and the testing configuration is that of Figure 5.5. The exciter and IR camera used were described in section 5.2. However, the flow diagram of Figure 6.13 can conceptually be used in any thermosonics testing application. The criterion to reliably detect a crack of size S_c can be expressed starting from the fundamental condition for successful crack detection:

$$\Delta T_{max} \geq \Delta T_{thr} \tag{6.6}$$

where ΔT_{max} is the temperature rise stimulated on the crack by a strain record characterized by a maximum heating index HI_{max} and ΔT_{thr} is the threshold temperature rise (as discussed earlier it is a function of the equipment sensitivity and spatial averaging in the IR image post-processing). Equation 6.6 can be rewritten in terms of HI using the results of the calibration:

$$HI_{max} \geq \frac{\Delta T_{thr}}{Cal(S_c)} \times SF \tag{6.7}$$

where $Cal(S_c)$ is the experimental calibration factor (function of the target crack size) and SF the safety factor, both determined from Figure 6.12. Hence, the threshold heating index will be defined as

$$HI_{thr} = \frac{\Delta T_{thr}}{Cal(S_c)} \times SF \tag{6.8}$$

to obtain

$$HI_{max} \geq HI_{thr} \tag{6.9}$$

which is the condition that has to be satisfied in each test to be able to be confident that cracks of the required size and location will be detected.

6.6 Review of Chapter

In this Chapter, the problem of practical testing using thermosonics has been tackled. This study moves from the background findings of Chapter 5, which clarified the basic mechanisms of thermosonic heating. The minimum combination of strain amplitude and frequency content necessary to achieve reliable detection of cracks was conveniently expressed by the heating index, HI. HI can be calculated from the analysis of the strain record, after a time constant which accounts for the depth at which the heat has been released (k) has been estimated. The minimum HI needed to exceed the minimum measurable temperature rise is a function of crack size, and it has been shown that it is relatively more difficult to detect cracks as their size decreases. With the setup used in this work, a crack measuring 2.9% of the specimen total cross section could never be detected. However, larger cracks of size between 3.5% and 7.8% of the cross section could be successfully detected and used to find an experimental curve to calibrate HI against the actual temperature rise as a function of crack size. The results from this calibration process were then used to recommend a testing algorithm that can be used in real thermosonic inspections. In principle, much smaller cracks can be found in different geometries (e.g. thinner beams) and/or using more powerful exciters [86]. However, the calibration procedure suggested in this Chapter remains a valid tool to empirically correlate temperature rise, vibration level and crack size, provided the same representative vibration parameter (e.g. strain, velocity or displacement) is measured during the calibration and real tests.

Chapter 7

Conclusions and further work

7.1 Review of Thesis

This thesis has investigated the performance of the vibro-acoustic modulation (VAM) and thermosonic methods of NDT applied to rapid screening of metallic structures for the detection of small cracks. As discussed in Chapter 1, both methods have the potential to detect fatigue cracks otherwise difficult to detect using traditional NDT techniques (especially when the cracks are small and tightly closed).

VAM and thermosonics are two relatively novel NDT methods which both rely on the excitation of vibrations able to generate differential movement of the crack interfaces. In this work, this was done by exciting one of the lowest frequency modes of the test structure in the case of VAM, or a large number of modes (simultaneously) in the lower ultrasonic frequency range between 20 and 200 kHz for thermosonics. The effects of displacing the cracks in these ways were then measured either using an interrogating ultrasonic signal (in the range between 100 and 230 kHz) for VAM, or by monitoring the temperature of the surface of the structure with an infrared camera looking for local heating at the defect location or close to it in the case of thermosonics.

Quantitative studies have been made possible by the availability of sets of speci-

mens of simple geometry with cracks of different size. In Chapter 2, the procedure to obtain cracks of controlled size by fatiguing metallic and perspex pre-notched beams has been illustrated; the cracks were grown to different depths looking at the propagating crack tip with a microscope while dynamically loading the specimens. Cracks were produced measuring from around 3% to 40% of the total cross section. This has allowed the correlation of the experimental results with the actual crack size known after breaking the specimens at the crack location. However, the crack size was found to be not the only parameter influencing the magnitude of the monitored quantities in both methods (sidebands-to-fundamental ratio for VAM, and temperature rise for thermosonics). Other morphological features like the initial pre-stress status of the crack, its partial opening and the crack roughness may have an effect on the sensitivity of VAM and thermosonics. The size, the initial partial opening and the roughness of the cracks produced for this work have been measured and characterized.

Both methodologies have been found to be related to the damping measurement method of NDT: in order to prove this, damping measurements were taken on all the available cracked specimens in addition to the VAM and thermosonic measurements. The experimental setups used to measure the crack damping have been described in Chapter 3. Initially, the damping readings were taken in order to compare the sensitivities of VAM and thermosonics with that of the damping method of NDT. However, the knowledge of the damping of the cracks, and its dependence on the frequency and amplitude of vibration, was also useful to predict the thermosonic temperature rise from the measurement of the vibration excited in the structure.

Work carried out within this project by Duffour et al. [94] showed that the sensitivity of the VAM method to small cracks in metallic structures is very similar to that of the damping method and, crucially, in this Thesis it was shown that both methods are extremely sensitive to the supporting conditions of the test-piece (Chapter 4). If the supports are not engineered properly, they may introduce significant amounts of damping and nonlinearities in the system, so that small cracks would become undetectable if their presence produces extra damping or extra nonlinearities of

the same order or less than that generated by the supports. Although VAM and damping measurement are in principle two different NDT methodologies, it was shown in Chapter 4 that VAM generally performs better for initially lightly damped systems, which are also ideal for the damping measurement method. A reliable implementation of VAM testing was achieved by suspending the specimens on elastic strings, de-coupling the specimen and the supports by means of rubber studs and exciting the low frequency vibration using an impact hammer. A vibro-modulation damage index has been defined and plotted versus the severity of each crack.

By contrast, thermosonics allows the cracks to be detected despite the specimens typically being either clamped to the supports or sandwiched between the exciter and the supports, both of which introduce a significant amount of damping and non-linearity. In these conditions, the energy converted into heat at the crack is picked up by the IR camera in the form of a temperature gradient, irrespective of the energy that is being dissipated elsewhere in the system (e.g. supports, contact between specimen and exciter, etc.) provided the crack is far enough from all other sources of heat. In essence, thermosonics can be regarded as a *local* damping measurement. This has been proved in Chapter 5, where the crack "thermosonic efficiency" was found to be proportional to the crack "damping efficiency". While thermosonics is virtually insensitive to the extra damping introduced by the supports in the system, it benefits from the nonlinearities caused by the contact between the specimen and the supports and between the specimen and the exciter. A rich frequency content of the excited vibration has been often been shown to be key to obtaining a measurable temperature rise.

Since the thermosonic excitation system produces non-reproducible, complex vibrations in the test-piece (due to the uncontrolled coupling and supporting conditions) it was decided to investigate the introduction of a unified measure of the excitation undergone by the crack, which could be used to establish whether any individual test reached a satisfactory level of vibration to be able to detect a crack of predetermined size. This has been done by defining the energy index and the heating index in Chapter 6, which are both calculated from the recorded vibration signal, and are

functions of both amplitude and frequency. In particular, the heating index can be correlated to the actual temperature rise that can be expected on the monitoring surface, and can therefore be calibrated against it on a batch of calibration cracks of target size. In practice, this calibration establishes experimentally a quantitative link between crack size, temperature rise and level of excitation. On this basis, a real-life testing procedure has been proposed which guarantees the reliable detection of cracks of target size.

7.2 Comparative analysis of VAM and thermosonics

Sensitivity

Using the implementation of VAM testing investigated in this Thesis and the vibro-modulation damage index defined in section 4.4.1, it was shown that cracks of size less than 7% of the total cross section are unlikely to be detected. By contrast, thermosonics could detect cracks through around 3% of the total cross section of the beams using the setup shown in Figure 5.5. Although both methods are sensitive to variations in the crack morphology, this study was carried out using beams cracked in the same fatiguing rig using similar loading settings, so the cracks had similar morphological characteristics. It can be argued that cracks smaller than 7% of the cross section could be detected by VAM, if the damage index was obtained by averaging over a narrower ultrasonic range of frequencies around one of the points of maximum sensitivity (see for example Figure 4.9) and higher levels of low frequency strain were excited; this observation is valid, however it has to be taken into account that, in this case, a preliminary ultrasonic sweep over a broad frequency range should always be performed to identify the ultrasonic frequencies of maximum sensitivity. For this reason it seemed more practical to average over a broad frequency range to calculate the vibro-modulation damage index. The excitation of higher low frequency strains would be problematic as the method has

been shown to be very sensitive to the supporting conditions and to the presence of attachments (e.g. shaker); for this reason the excitation of higher strains in VAM was not pursued further. Obtaining a higher VAM sensitivity would require significant further efforts in the optimization of the testing rig. Conversely, in the case of thermosonics, it would be sufficient to use a more powerful exciter to excite higher levels of vibration and be able to detect smaller cracks, as reported by Favro et al. [85].

Reliability

For VAM, reliable crack detection can be potentially achieved in three steps: first, the testing rig has to be optimized to ensure negligible strain dependence of the sidebands for an uncracked specimen, then ultrasonic probing frequencies of maximum sensitivity have to be selected and finally a large strain (magnitude dependent on size to be detected) has to be excited at the crack location (i.e. the crack must not be at a low frequency vibration node). However, the issue of reliable crack detection using VAM has not been investigated in depth in this Thesis since the method appeared less attractive than thermosonics due to the need to optimize the supports and to sweep the ultrasonic frequency. For thermosonics, the subject of reliable crack detection has been investigated in detail in Chapter 6 and the real-life testing procedure that has been suggested ensures the reliable detection of target cracks if the maximum heating index reached in a test exceeds a minimum prescribed threshold value.

Defect location

In the implementation used in this Thesis, VAM does not offer information on the defect location; it can only provide a pass/fail test on the respective absence/presence of a crack. Conversely, one of the key advantages of thermosonics is the immediate knowledge of the location of the defect. However, to achieve this, the threshold heating index should be excited throughout the whole structure (this will be discussed

later in section 7.4.2).

Inspection time

If a point of maximum sensitivity for the ultrasonic interrogating signal is known, the VAM test could be carried out relatively quickly (on the assumption that the test rig has been previously optimized). A disadvantage in terms of rapidity of inspection for VAM is represented by the need to ensure a point of maximum sensitivity by sweeping the ultrasound, especially if small cracks have to be detected. By contrast, thermosonics is an intrinsically fast method, although a relatively large time could be spent on the optimization of the supports and excitation (which is an equivalent issue in VAM testing).

Usability

Usability is here intended to describe the extent to which either method could be used as an "off-the-shelf" and "user-friendly" tool for rapid screening of structures for small fatigue cracks. In this respect, the common factor shared by VAM and thermosonics is the need to carry out a preliminary optimization of the testing rigs before the data can be used to make an assessment of whether the target cracks can be detected reliably or not. In the case of VAM, the supports must not introduce significant nonlinearities in the system, whereas for thermosonics the exciter and the supports have to be optimized to excite the minimum heating index required in the whole specimen. Once this has been achieved (in both cases this may require considerable effort), the test-piece can be tested straightaway using thermosonics, although in certain circumstances cleaning of the component and/or painting it black may be required to provide a uniform maximum emissivity. The test-component that has to be prepared to be tested using VAM will have to be cleaned in order to enable the attachment of any studding required to support the specimens.

Cost of equipment

The major cost for equipment is represented by the IR camera employed by thermosonics (at least one order of magnitude more expensive than any other instrument that may be required for VAM or thermosonics testing), whereas the cost of ultrasonic horns is similar to the cost of any other standard exciter used in modal analysis (e.g. electromagnetic shakers). Less expensive, uncooled microbolometer IR cameras are nowadays available in the market, and are usually characterized by a sensitivity a factor of 4 to 5 lower than the traditional cooled IR cameras [95]. VAM uses standard means to excite the required vibration fields and is therefore potentially much cheaper to implement than thermosonics.

7.3 Summary of scientific achievements

The work on VAM and thermosonics undertaken in this Thesis has led to an extensive quantitative assessment of the potential of both methods for the rapid detection of small cracks.

The sensitivity of the VAM method that was chosen for implementation has been shown (Chapter 4) to be a function of the ultrasonic frequency selected for inspection; points of maximum and minimum sensitivity to the defects have been found to alternate regularly across a wide ultrasonic frequency range. The immediate practical implication of these results is that an ultrasonic frequency sweep is likely to be required in most NDT VAM applications, particularly if small cracks need to be detected.

In order to increase the VAM sensitivity to small cracks, a large low frequency strain could be applied at the crack location as an alternative or in addition to tuning to a point of ultrasonic maximum sensitivity. However, this strategy is likely to be very difficult to implement since the VAM method used in this Thesis has been shown to be sensitive to the supporting conditions and to possible exciter attachments. It was found that this poses a further limitation to the practical potential of inspection of

VAM. The findings discussed so far have been presented in a conference paper [P6] and in a journal paper [P3].

In another journal paper [P1], it was demonstrated that there is no significant advantage using this implementation of VAM over the traditional damping measurement method of NDT for detecting cracks in metallic or perspex beams: both techniques appeared to offer limited sensitivity for the detection of small cracks and hence could be rated as equivalent for the purpose. An improvement of the sensitivity of both damping measurement and VAM would mean significant efforts in the optimization of the supports which results in a loss of attractiveness for industrial applications.

The systematic measurement of crack damping has led to an insight on the dissipation mechanisms at the crack that are also responsible for the generation of the heat detected by thermosonics (Chapter 3). If large vibration amplitudes are reached, a portion of the crack area can lose contact at the asperities and therefore the damping may decrease for increasing amplitude vibration, in contrast with the traditional statement that the structural damping (to which the presence of the crack added) increases for increasing vibration amplitudes. This effect has been measured and has been taken into account for the relevant specimens in the prediction of the thermosonic signal. These results can be found in a journal paper [P4] and in a conference paper [P7].

In Chapter 5, the thermosonic temperature rise was calculated on the basis of the additional structural damping due to the cracks (which was measured previously and independently of the thermosonic tests). The results showed that thermosonics can be regarded as a localized damping measurement, although the scatter in the correlation between the thermosonic efficiency and the damping efficiency demonstrated that the three-dimensional morphology of the cracks may affect the accuracy of the predictions. These findings were included in a conference paper [P8] and in a journal paper [P4].

Since the thermosonic method appeared promising for quick NDT, an in-depth study was carried out in Chapter 6 to establish criteria for the reliable detection of small

cracks. The calibration procedure established a methodology to find empirically the minimum vibration level that generates a measurable temperature rise on the cracks that need to be detected using an IR camera of known sensitivity. This quantitative link between the fundamental variables of thermosonics is the foundation of a simple procedure to ensure that sufficient strain level has been achieved in a given test to ensure detection of any cracks of the required size. These findings have been in part published in a conference paper [P9] and the submission of a journal paper [P5] has been planned.

Finally, the experience gained throughout this work has also helped to advance the application of thermosonics to the detection of delaminations in composites. This part of the project has not been discussed in this Thesis, since it was carried out under the responsibility of the collaborators at the University of Bath (see Chapter 1). However, most thermosonic experiments on composites were carried out in parallel with the thermosonic tests on metals (which were the main area of investigation) and benefited from them. The advances in thermosonic testing on composites have been published in a journal paper [P2].

7.4 Further work

7.4.1 Further work on VAM

Further work could be carried out (on the same specimens) to compare the performance of the implementation of VAM testing studied in this Thesis with other implementations which are also usually categorized within the VAM family: for example, tests could be carried out using two or more ultrasonic signals and looking at their inter-modulation [96], by using short ultrasound pulses travelling in the test-structure in pulse-echo or pitch-catch configuration [61], or by looking at phase modulation in addition to amplitude modulation [51].

VAM tests were carried out in this Thesis on rather thick mild steel beams with

through-width cracks extending to a maximum depth of a few millimeters; further work could be conducted to investigate thin aluminium plates with through-thickness cracks (this geometry is similar to the panels used in the aerospace industry) and a new assessment of sensitivity could be carried out for these specimens and compared with the VAM sensitivity performance found in this Thesis. More sophisticated post-processing routines (e.g. bispectrum analysis [96]) could also be used on the data that have been already collected for this study to establish whether this brings any improvement of the sensitivity of the method to small cracks.

7.4.2 Further work on thermosonics

Further work could be planned to compare (on the same specimens) the performance of the pulsed implementation of ultrasound stimulated thermography studied in this Thesis with the continuous excitation method known as "lock-in" ultrasound stimulated thermography [80].

Throughout the thermosonics research, cracks known to be located in the middle of the beams have been detected and a procedure to reliably detect small cracks known to be in one or more *specific* locations of the test-structure has been prescribed in Chapter 6. However, for real applications it will be valuable to extend this procedure to cases where the possible crack location is unknown. In order to do this, criteria will have to be developed to ensure that the threshold heating index is surpassed over the whole structure during the test and not only at one location. This could be achieved by exciting, for example, a number of high frequency modes of the structure simultaneously (broad band excitation) or in succession by sweeping the excitation over a frequency range. Another significant area of investigation would be the detection of non-surface-breaking cracks and the analysis of the maximum detectable depth as a function of the excitation level. Finally, it has been shown in this Thesis that the current thermosonics excitation method is non controlled; a key area of investigation for thermosonics to become a routine inspection method in industry would be the availability of an excitation apparatus able to ensure that the correct modes and amplitudes needed to excite the required heating

index throughout the whole structure are consistently excited. To achieve this, both the mechanical and electrical behaviour of the acoustic horns described in Chapter 5 should be further analyzed in order to develop new, better controlled and dedicated thermosonics exciters.

References

[1] C. Hellier, *Handbook of Nondestructive Evaluation* (McGraw Hill, New York - London, 2001).

[2] X. Maldague, *Nondestructive Evaluation of Materials by Infrared Thermography* (Springer-Verlag, London, 1993).

[3] X. Maldague, in *Trends in Optical Nondestructive Testing and Inspection*, edited by P. K. Rastogi and I. Inaudi (Elsevier Science, New York, 2000), Chap. Application of infrared thermography in nondestructive evaluation (invited chapter), pp. 591–609.

[4] D. Almond, G. Busse, E. Grinzato, J. C. Krapez, X. Maldague, V. Vavilov, and W. Peng, "Infrared thermographic detection and characterization of impact damages in carbon fiber plastics: round robin test result," in *Proceedings of QIRT98 (Quantitative Infrared Thermography 1998), Lodz, Poland, 7-10 September 1998*, edited by D. Balageas, G. Busse, and G. Carlomagno (PKOpto - Polish Society of Optoelectronic Engineering, Warszawa - Poland, 1998), Eurotherm Seminar 60.

[5] A. S. Korotkov, M. M. Slavinskii, and A. M. Sutin, "Variations of acoustic nonlinear parameters with the concentration of defects in solids," Acoustical Physics **40**(1), 71–74 (1994).

[6] R. L. Thomas, L. D. Favro, X. Han, Z. Ouyang, H. Sui, and G. Sun, Infrared imaging of ultrasonically excited subsurface defects in materials, US PATENT APPLICATION number 6236049, 1999.

[7] R. B. Mignogna, R. E. Green, J. C. Duke, E. G. Henneke, and K. L. Reifsnider, "Thermographic investigation of high-power ultrasonic heating in materials," Ultrasonics **19**(4), 159 (1981).

[8] P. Cawley and D. P. Almond, Thermosonics - A New Quick Technique for Crack Detection, 2002, case for support.

[9] D. Donskoy, A. Zagrai, and J. Lottiaux, "N-scan: new vibro-modulation system for detection monitoring and characterization," in *Review of Progress in Quantitative Nondestructive Evaluation 23*, Vol. 700 of *AIP Conference Proceedings*, edited by D. O. Thompson and D. E. Chimenti (American Institute of Physics, Melville, NY, 2003), pp. 1414–1421.

[10] M. Rothenfusser and C. Homma, "Acoustic thermography: vibrational modes of cracks and the mechanism of heat generation," in *Review of Progress in Quantitative Nondestructive Evaluation 24*, Vol. 760 of *AIP Conference Proceedings*, edited by D. O. Thompson and D. E. Chimenti (American Institute of Physics, Melville, NY, 2004), pp. 624–631.

[11] N. E. Dowling, *Mechanical Behavior of Materials : Engineering Methods for Deformation, Fracture, and Fatigue* (Prentice Hall, New Jersey, 1999).

[12] R. L. Carlson and G. A. Kardomateas, *An Introduction to Fatigue in Metals and Composites* (Chapman-Hall, London, 1996).

[13] D. Broek, *The Practical Use of Fracture Mechanics* (Kluwer Academic Publishers, Boston/London, 1988).

[14] S. Stoychev and D. Kujawski, "Methods for crack opening load and crack tip shielding determination: a review," Fatigue and Fracture of Engineering Materials and Structures **26**, 1053–1067 (2003).

[15] Y. Verreman, "Monitoring short fatigue cracks with miniature strain gages," Experimental Mechanics **34**(3), 207–216 (1994).

[16] P. Cawley and R. Ray, "A comparison of the natural frequency changes produced by cracks and slots," Journal of Vibration, Acoustics, Stress and Reliability in Design **110**, 366–370 (1988).

[17] M. Imregun and K. Y. Sanliturk, "Natural frequency and damping changes produced by fatigue cracks," in *Proceedings of the 15th Seminar on Modal Analysis* (Leuven, Belgium, 19-21 September, 1990), pp. 791–805.

[18] R. D. Adams, P. Cawley, C. J. Pye, and B. J. Stone, "Vibration technique for non-destructively assessing integrity of structures," Journal of Mechanical Engineering Science **20**(2), 93–100 (1978).

[19] R. D. Adams and P. Cawley, "Vibration techniques in nondestructive testing," in *Research Techniques in Nondestructive Testing*, edited by R. S. Sharpe (Academic Press Inc. Ltd., London, 1985), Vol. 8, Chap. 7, pp. 304–360.

[20] C. F. Beards, *Structural Vibration: Analysis and Damping* (Arnold, London, 1996).

[21] A. P. Bovsunovsky and A. G. Kratko, "The shape of mechanical hysteresis loops for metals under harmonic loading," Journal of Testing and Evaluation **26**(1), 31–37 (1998).

[22] A. D. Dimarogonas and S. D. Panteliou, "Damping associated with porosity and crack in solids," Theoretical and Applied Fracture Mechanics **34**, 217–223 (2000).

[23] S. D. Panteliou, T. G. Chondros, V. C. Argyrakis, and A. D. Dimarogonas, "Damping factor as an indicator of crack severity," Journal of Sound and Vibration **241**(2), (2001).

[24] A. P. Bovsunovsky, C. Surace, and R. Ruotolo, "The effect of damping on the non-linear dynamic behaviour of a cracked beam at resonance and super-resonance vibrations," *Damage Assessment of Structures, Proceedings*, Vol. 245-2 of *Key Engineering Materials* (CSA Illumina, Bathesda, Maryland, 2003), pp. 97–105.

[25] A. P. Bovsunovsky and C. Surace, "Considerations regarding superharmonic vibrations of a cracked beam and the variation in damping caused by the presence of the crack," Journal of Sound and Vibration **288**(4-5), 865–886 (2005).

[26] B. J. Lazan, *Damping of Materials and Members in Structural Mechanics* (Pergamon Press, Oxford, UK, 1968).

[27] D. J. Inman, *Engineering Vibration* (Prentice-Hall International, London, 1994).

[28] D. J. Ewins, *Modal Testing: Theory and Practice* (Research Studies Press, Baldock, UK, 1984).

[29] A. P. Bovsunovsky, "The mechanisms of energy dissipation in the non-propagating fatigue cracks in metallic materials," Engineering Fracture Mechanics **71**(16-17), 2271–2281 (2004).

[30] P. Cawley and N. Sarsentis, "A quick method for the measurement of structural damping," Mechanical Systems and Signal Processing **2**, 39–47 (1988).

[31] J. Goken, D. Letzig, and K. Kainer, "Measurement of crack induced damping of cast magnesium alloy AZ91," Journal of Alloys and Compounds **378**, 220–225 (2004).

[32] R. D. Blevins, "Modal density of rectangular volumes, areas, and lines," Journal of the Acoustical Society of America **119**(2), 788–791 (2006).

[33] S. G. Braun, D. J. Ewins, and S. S. Rao, *Encyclopedia of Vibration* (Academic Press, San Diego, 2002).

[34] L. Meirovitch, *Elements of Vibration Analysis* (MacGraw-Hill, New York, 1986).

[35] E. M. Uygur, "Nondestructive dynamic testing," in *Research Techniques in Nondestructive Testing*, edited by R. S. Sharpe (Academic Press, New York, 1980), Vol. 4, pp. 205–244.

[36] Y. Zheng, R. G. Maev, and I. Y. Solodov, "Nonlinear acoustic applications for material characterization: a reveiw," Canadian Journal of Physics **77**, 927–967 (1999).

[37] L. Bjorno, "Forty years of nonlinear ultrasound," Ultrasonic **40**, 11–17 (2002).

[38] P. B. Nagy, "Fatigue damage assessment by nonlinear ultrasonic material characterization," Ultrasonics **36**, 365–381 (1998).

[39] O. Buck, W. L. Morris, and J. M. Richardson, "Acoustic harmonic generation at unbounded interfaces and fatigue cracks," Applied Physics Letters **33**(5), 371–373 (1978).

[40] I. Y. Solodov, "Ultrasonics of nonlinear contacts: propagation, reflection and NDE-applications," Ultrasonics **36**, 383–390 (1998).

[41] B. A. Korshak, I. Y. Solodov, and E. M. Ballad, "Dc effects, sub-harmonics, stochasticity and 'memory' for contact acoustic non-linearity," Ultrasonics **36**, .

[42] K. E.-A. Van Den Abeele, J. Carmeliet, J. A. Tencate, and P. A. Johnson, "Nonlinear elastic wave spectroscopy (NEWS) techniques to discern material damage, part II: single-mode nonlinear resonance acoustic spectroscopy," Research in Nondestructive Evaluation **12**, 31–42 (2000).

[43] A. S. Korotkov and A. M. Sutin, "Modulation of ultrasound by vibration in metal constructions with cracks," Acoustics Letters **18**(4), 59–62 (1994).

[44] M. M. Korotkov, A. S. Slavinskii and A. M. Sutin, "Variation of acoustic nonlinear parameters with the concentraion of defects in steel," Acoustical Physics **40**(1), 84–87 (1994).

[45] N. Krohn, R. Stoessel, and G. Busse, "Acoustic nonlinearity for defect selective imaging," Ultrasonics **40**, 633–637 (2002).

[46] V. V. Kazakov, A. M. Sutin, and P. A. Johnson, "Sensitive imaging of an elastic nonlinear wave-scattering source in a solid," Applied Physics Letters **81**(4), 646–648 (2002).

[47] I. Y. Solodov, N. Krohn, and G. Busse, "CAN: and example of nonclassical acoustic nonlinearity," Ultrasonics **40**, 621–625 (2002).

[48] J. G. Sessler and V. Weiss, Crack detection apparatus and method, US PATENT number 3867836, 1975.

[49] K. E.-A. Van Den Abeele, A. M. Sutin, J. Carmeliet, and P. A. Johnson, "Micro-damage diagnostics using nonlinear elastic wave spectroscopy," NDT&E International **34**, 239–248 (2001).

[50] V. V. Kazakov and A. M. Sutin, "Pulsed sounding of cracks with the use of the modulation of ultrasound by vibrations," Acoustical Physics **47**(3), 308–312 (2001).

[51] V. Y. Zaitsev, A. M. Sutin, I. Y. Belyaeva, and V. E. Nazarov, "Nonlinear interaction of acoustical waves due to cracks and its possible usage for cracks detection," Journal of Vibration and Control **1**, 335–344 (1995).

[52] A. V. Oppenheim, A. S. Willsky, and S. H. Nawab, *Signals and Systems* (Prentice Hall International, Upper Saddle River, New Jersey, USA, 1997).

[53] D. M. Donskoy and A. M. Sutin, "Vibro-acoustic modulation nondestructive evaluation technique," Journal of intelligent material systems and structures **9**, 765–771 (1998).

[54] D. M. Donskoy and A. M. Sutin, "Vibro-acoustic modulation nondestructive evaluation technique," in *Nondestructive evaluation of aging aircraft, airports and aerospace hardware II*, Vol. 3397 of *SPIE proceedings*, edited by G. A. Geithman and G. E. Georgeson (SPIE, San Antonio Texas, 1998), pp. 226–237.

[55] A. E. Ekimov, I. N. Didenkulov, and V. V. Kazakov, "Modulation of torsional waves in a rod with a crack," Journal of the Acoustical Society of America **106**(3), 1289–1292 (1999).

[56] V. Zaitsev and P. Sas, "Nonlinear response of a weakly damaged metal sample: a dissipative modulation mechanism of vibro-acoustic interaction," Journal of Vibration and Control **6**, 803–822 (2000).

[57] K. E.-A. Van Den Abeele, P. A. Johnson, and A. M. Sutin, "Nonlinear elastic wave spectroscopy (NEWS) techniques to discern material damage, part I: nonlinear wave moudlation spectroscopy (NWMS)," Research in Nondestructive Evaluation **12**, 17–30 (2000).

[58] D. M. Donskoy, A. M. Sutin, and A. E. Ekimov, "Nonlinear acoustic interaction on contact interfaces and its use for nondestructive testing," NDT&E International **34**, 231–238 (2001).

[59] I. Y. Balyaeva and V. Y. Zaitsev, "Nonlinear scattering of acoustic waves by discontinuity-like defects in application to crack detection," Journal of Vibration and Control **2**, 465–478 (1996).

[60] J. Y. Kim, V. A. Yakovlev, and S. I. Rokhlin, "Parametric modulation mechanism of surface acoustic wave on a partially closed crack," Applied Physics Letters **82**(19), 3203–3205 (2003).

[61] J. Y. Kim, V. A. Yakovlev, and S. I. Rokhlin, "Surface acoustic wave modulation on a partially closed fatigue crack," Journal of the Acoustical Society of America **115**(5), 1961–1972 (2004).

[62] W. J. Staszewski, Using acoustic waves to determine the structural integrity of a body, GB PATENT number 2383412, 2003.

[63] V. V. Kazakov, "A modulation crack-detection technique: I. instrumental method of implementation," Russian Journal of Nondestructive Testing **42**(11), 709–716 (2006).

[64] P. Duffour, M. Morbidini, and P. Cawley, "A study of the vibro-acoustic modulation technique for the detection of cracks in metals," Journal of the Acoustical Society of America **119**(3), 1463–1975 (2006).

[65] D. Newkirk and R. Karlquist, "Mixers, modulators and demodulators," in *The ARRL Handbook for Radio Communications, 2006* (ARRL, Newington, CT, 2006), Vol. 81st edition, pp. 15.1–15.36.

[66] K. L. Narayan and C. Jebaraj, "Sensitivity analysis of local/global modal parameters for identification of a crack in a beam," Journal of Sound and Vibration **228**, 994–997 (1999).

[67] G. M. Owolabi, A. S. J. Swamidas, and R. Seshadri, "Crack detection in beams using changes in frequencies and amplitudes of frequency response functions," Journal of Sound and Vibrations **65**, 1–22 (2003).

[68] B. W. Drinkwater, R. Dwyer-Joyce, and P. Cawley, "A study of the interaction between ultrasound and a partially contacting solid-solid interface," Proceedings of the Royal Society of London A **452**, 2613–2628 (1996).

[69] J. M. Richardson, "Harmonic generation at an unbounded interface. I: planar interface between semi-infinite elastic media," International Journal of Engineering Science **17**, 73–85 (1979).

[70] R. E. Ziemer and W. H. Tranter, *Principles of Communication* (Wiley, New York, 2003).

[71] S. H. Crandall, N. C. Dahl, and L. T. J., *An Introduction to the Mechanics of Solids* (McGraw-Hill, Tokyo, Japan, 1978).

[72] R. L. Thomas, "Thermal NDE techniques - from photoacoustics to thermosonics," in *Review of Progress in Quantitative Nondestructive Evaluation 21*, Vol. 615 of *AIP Conference Proceedings*, edited by D. O. Thompson and D. E. Chimenti (American Institute of Physics, Melville, NY, 2002), pp. 3–13.

[73] D. Wu, A. Salerno, J. Rantala, and G. Busse, "Characterization of layered materials using lock-in thermography," Progress in Natural Science **6**, 76–79 (1996), suppl. S.

[74] D. T. Wu and G. Busse, "Lock-in thermography for nondestructive evaluation of materials," Revue Generale De Thermique **37**(8), 693–703 (1998).

[75] C. J. Pye and R. D. Adams, "Heat emission from damaged composite materials and its use in nondestructive testing," Journal of Physics D-Applied Physics **14**(5), 927–941 (1981).

[76] C. J. Pye and R. D. Adams, "Detection of damage in fiber reinforced plastics using thermal fields generated during resonant vibration," NDT&E International **14**(3), 111–118 (1981).

[77] J. Rantala, D. Wu, and G. Busse, "Amplitude-modulated lock-in vibrothermography for NDE of polymers and composites," Research in Nondestructive Evaluation **7**(4), 215–228 (1996).

[78] J. Rantala, D. Wu, and G. Busse, "NDT of polymer materials using lock-in thermography with water-coupled ultrasonic excitation," NDT&E International **31**(1), 43–49 (1998).

[79] L. D. Favro, X. Y. Han, Z. Ouyang, G. Sun, H. Sui, and R. L. Thomas, "Infrared imaging of defects heated by a sonic pulse," Review of Scientific Instruments **71**(6), 2418–2421 (2000).

[80] T. Zweschper, A. Dillenz, and G. Busse, "Ultrasound lock-in thermography - a defect-selective NDT method for the inspection of aerospace components," Insight **43**(3), 173–179 (2001).

[81] L. D. Favro, X. Y. Han, O. Y. Zhong, G. Sun, and R. L. Thomas, "Sonic IR imaging of cracks and delaminations," Analytical Sciences **17**, S451–S453 (2001), sp. Iss. SI.

[82] T. Zweschper, A. Dillenz, G. Riegert, D. Scherling, and G. Busse, "Ultrasound excited thermography using frequency modulated elastic waves," Insight **45**(3), 178–182 (2003).

[83] A. Dillenz, T. Zweschper, and G. Busse, "Elastic wave burst thermography for NDE of subsurface features," Insight **42**(12), 815–817 (2000).

[84] L. D. Favro, X. Y. Han, Z. Ouyang, L. Li, S. Wang, and R. L. Thomas, "Thermosonic imaging of cracks and delaminations," Progress in Natural Science **11**, S133–S136 (2001), suppl. S.

[85] L. D. Favro, R. L. Thomas, X. Han, Z. Ouyang, G. Newaz, and D. Gentile, "Sonic infrared imaging of fatigue cracks," International Journal of Fatigue **23**, S471–S476 (2001), suppl. S.

[86] X. Y. Han, L. D. Favro, and R. L. Thomas, "Recent developments in sonic IR imaging," in *Review of Progress in Quantitative Nondestructive Evaluation 22*, Vol. 657 of *AIP Conference Proceedings*, edited by D. O. Thompson and D. E. Chimenti (American Institute of Physics, Melville, NY, 2003), pp. 500–505.

[87] X. Y. Han, W. Li, Z. Zeng, L. D. Favro, and R. L. Thomas, "Acoustic chaos and sonic infrared imaging," Applied Physics Letters **81**(17), 3188–3190 (2002).

[88] X. Y. Han, Z. Zeng, W. Li, M. S. Islam, J. P. Lu, V. Loggins, E. Yitamben, L. D. Favro, G. Newaz, and R. L. Thomas, "Acoustic chaos for enhanced detectability of cracks by sonic infrared imaging," Journal of Applied Physics **95**(7), 3792–3797 (2004).

[89] X. Y. Han, V. Loggins, Z. Zeng, L. D. Favro, and R. L. Thomas, "Mechanical model for the generation of acoustic chaos in sonic infrared imaging," Applied Physics Letters **85**(8), 1332–1334 (2004).

[90] X. Y. Han, M. S. Islam, G. Newaz, L. D. Favro, and R. L. Thomas, "Finite-element modeling of acoustic chaos to sonic infrared imaging," Journal of Applied Physics **98**(1), article 014907, 4 pages (2005).

[91] X. Y. Han, M. Sarwar Islam, L. D. Favro, and R. L. Thomas, "Finite element modeling of the heating of cracks during sonic infrared imaging," Journal of Applied Physics **99**(7), article 074905, 7 pages (2006).

[92] Z. Ouyang, "Theoretical modeling of thermosonic imaging of cracks," in *Review of Progress in Quantitative Nondestructive Evaluation 21*, Vol. 615 of *AIP Conference Proceedings*, edited by D. O. Thompson and D. E. Chimenti (American Institute of Physics, Melville, NY, 2002), pp. 577–581.

[93] H. S. Carslaw and J. C. Jaeger, *Conduction of Heat in Solids* (Clarendon Press, Oxford, UK, 1986).

[94] P. Duffour, M. Morbidini, and P. Cawley, "Comparison between a type of vibro-acoustic modulation and damping measurement as NDT techniques," NDT&E International **39**, 123–131 (2006).

[95] P. Cawley and D. P. Almond, Compact thermosonic NDE system, 2006, case for support.

[96] A. J. Hillis, S. A. Neild, B. W. Drinkwater, and P. D. Wilcox, "Global crack detection using bispectral analysis," Proceedings of the Royal Society of London A **462**, 1515–1530 (2006).

List of Publications

Journal Articles

[P1] P. Duffour, M. Morbidini and P. Cawley: *Comparison between a type of vibro-acoustic modulation and damping measurement as NDT techniques*, in NDT&E International, Vol. 39, September 2005, pp. 123-131.

[P2] T. Barden, M. Morbidini, D. Almond and P. Cawley: *Advances in thermosonics for detecting impact damage in CFRP composites*, in Insight, Vol. 48, Num. 2, February 2006, pp. 90-93.

[P3] P. Duffour, M. Morbidini and P. Cawley: *A study of the vibro-acoustic modulation technique for the detection of cracks in metals*, in Journal of the Acoustical Society of America, Vol. 119, Num. 3, March 2006, pp. 1463-1475.

[P4] M. Morbidini, P. Cawley, T. Barden, D. Almond and P. Duffour: *Prediction of the thermosonic signal from fatigue cracks in metals using vibration damping measurements*, in Journal of Applied Physics, Vol. 100, Num. 10, November 2006, Article 4905, pp. 1-13.

[P5] M. Morbidini and P. Cawley: *Reliable crack detection using thermosonics*, to be published.

Conference Papers

[P6] M. Morbidini, P. Duffour, and P. Cawley: *Vibro-acoustic modulation - Part 2: an experimental study*, in Review of Progress in Quantitative Nondestructive Evaluation Vol. 24, AIP Conference Proceedings Vol. 760, April 2005, pp. 616-623.

[P7] M. Morbidini, P. Cawley, T. Barden, D. Almond and P. Duffour: *A new approach for the prediction of the thermosonic signal from vibration records*, in Review of Progress in Quantitative Nondestructive Evaluation Vol. 25, AIP Conference Proceedings Vol. 820, March 2006, pp. 558-565.

[P8] M. Morbidini, P. Cawley, P. Duffour, T. Barden and D. Almond: *The relationship between crack damping, vibration amplitude and temperature rise in thermosonics NDT*, in Review of Progress in Quantitative Nondestructive Evaluation Vol. 26, to be published in the AIP Conference Proceedings in 2007.

[P9] M. Morbidini, P. Cawley, T. Barden, D. Almond and P. Duffour: *The relationship between vibration level and minimum detectable defect size in sonic-IR inspection*, in Proceedings of the 9th European Conference in NDT (ECNDT), Berlin, September 2006.